

NAVAL POSTGRADUATE SCHOOL

Monterey, California



THESIS

**DRIFTER OBSERVATIONS
OF THE
MEDITERRANEAN SEA SURFACE CIRCULATION**

by

Todd A. Mauerhan

March 2000

Thesis Advisor:
Second Reader:

Pierre-Marie Poulain
Jeffrey D. Paduan

Approved for public release; distribution is unlimited.

DTIC QUALITY INSPECTED 4

20000608 103

REPORT DOCUMENTATION PAGE

Form Approved
OMB No. 0704-0188

Public reporting burden for this collection of information is estimated to average 1 hour per response, including the time for reviewing instruction, searching existing data sources, gathering and maintaining the data needed, and completing and reviewing the collection of information. Send comments regarding this burden estimate or any other aspect of this collection of information, including suggestions for reducing this burden, to Washington headquarters Services, Directorate for Information Operations and Reports, 1215 Jefferson Davis Highway, Suite 1204, Arlington, VA 22202-4302, and to the Office of Management and Budget, Paperwork Reduction Project (0704-0188) Washington DC 20503.

1. AGENCY USE ONLY (Leave blank)	2. REPORT DATE March 2000	3. REPORT TYPE AND DATES COVERED Master's Thesis
----------------------------------	------------------------------	---

4. TITLE AND SUBTITLE Drifter Observations of the Mediterranean Sea Surface	5. FUNDING NUMBERS
6. AUTHOR(S) Mauerhan, Todd A.	

7. PERFORMING ORGANIZATION NAME(S) AND ADDRESS(ES) Naval Postgraduate School Monterey, CA 93943-5000	8. PERFORMING ORGANIZATION REPORT NUMBER
--	---

9. SPONSORING / MONITORING AGENCY NAME(S) AND ADDRESS(ES)	10. SPONSORING / MONITORING AGENCY REPORT NUMBER
---	---

11. SUPPLEMENTARY NOTES
The views expressed in this thesis are those of the author and do not reflect the official policy or position of the Department of Defense or the U.S. Government.

12a. DISTRIBUTION / AVAILABILITY STATEMENT Approved for public release; distribution is unlimited.	12b. DISTRIBUTION CODE
---	------------------------

13. ABSTRACT (maximum 200 words)

Since June 2, 1986, several institutions have conducted a variety of drifter studies within the Mediterranean Sea for scientific and operational purposes. The data from these studies include 521 individual drifters and span over 13 years. This thesis examines these data in an effort to better describe the Mediterranean Sea surface circulation. Interpretation of the data is conducted by calculating Eulerian and Lagrangian statistics and evaluating some of the errors they contain.

An Eulerian framework is employed that best represents the surface flow throughout the Mediterranean Sea as a combination of a deterministic mean and fluctuations due to temporal and mesoscale variability. The results of the Eulerian statistics are presented as charts of Mean Kinetic Energy (MKE), Eddy Kinetic Energy (EKE), mean flow, and velocity variance. Seasonality is analyzed in regions where temporal and spatial coverage of drifter observations is adequate. Drifter wind slippage errors and array biases are evaluated to possibly determine a valid correction. The Lagrangian statistics: diffusivity, velocity covariance, and integral time and space scales are computed.

The Eulerian and Lagrangian surface circulation statistics computed from the drifters are in general similar, but much improved and more accurate, to those presented in earlier works.

14. SUBJECT TERMS Mediterranean Sea, Surface Circulation, Drifter, Lagrangian Methods, Eulerian Methods	15. NUMBER OF PAGES 114
	16. PRICE CODE

17. SECURITY CLASSIFICATION OF REPORT Unclassified	18. SECURITY CLASSIFICATION OF THIS PAGE Unclassified	19. SECURITY CLASSIFI- CATION OF ABSTRACT Unclassified	20. LIMITATION OF ABSTRACT UL
---	---	--	-------------------------------------

Approved for public release; distribution is unlimited

**DRIFTER OBSERVATIONS OF
THE MEDITERRANEAN SEA SURFACE CIRCULATION**

Todd A. Mauerhan
Lieutenant, United States Navy
B.S., Texas A&M University, 1987
B.S., Texas A&I University, 1987

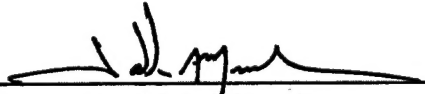
Submitted in partial fulfillment of the
requirements for the degree of

MASTER OF SCIENCE IN PHYSICAL OCEANOGRAPHY

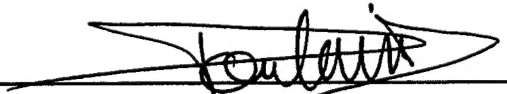
from the

**NAVAL POSTGRADUATE SCHOOL
March 2000**

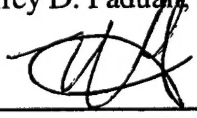
Author: _____


Todd A. Mauerhan

Approved by: _____


Pierre-Marie Poulain, Thesis Advisor


Jeffrey D. Paduan, Second Reader


Roland W. Garwood, Jr., Chairman
Department of Oceanography

ABSTRACT

Since June 2, 1986, several institutions have conducted a variety of drifter studies within the Mediterranean Sea for scientific and operational purposes. The data from these studies include 521 individual drifters and span over 13 years. This thesis examines these data in an effort to better describe the Mediterranean Sea surface circulation. Interpretation of the data is conducted by calculating Eulerian and Lagrangian statistics and evaluating some of the errors they contain.

An Eulerian framework is employed that best represents the surface flow throughout the Mediterranean Sea as a combination of a deterministic mean and fluctuations due to temporal and mesoscale variability. The results of the Eulerian statistics are presented as charts of Mean Kinetic Energy (MKE), Eddy Kinetic Energy (EKE), mean flow, and velocity variance. Seasonality is analyzed in regions where temporal and spatial coverage of drifter observations is adequate. Drifter wind slippage errors and array biases are evaluated to possibly determine a valid correction. The Lagrangian statistics: diffusivity, velocity covariance, and integral time and space scales are computed.

The Eulerian and Lagrangian surface circulation statistics computed from the drifters are in general similar, but much improved and more accurate, to those presented in earlier works.

TABLE OF CONTENTS

I.	INTRODUCTION.....	1
II.	BACKGROUND	3
A.	MEDITERRANEAN SEA GENERAL CHARACTERISTICS.....	3
B.	MEDITERRANEAN SURFACE CIRCULATION	4
C.	SEASONAL VARIABILITY.....	6
D.	DRIFTER STUDIES.....	7
III.	DATA.....	9
A.	BUOY DESCRIPTIONS.....	9
1.	CODE.....	9
2.	CMOD	10
3.	SVP and TRISTAR.....	10
4.	A111 and A104.....	11
5.	Other.....	11
B.	DEPLOYMENTS.....	12
C.	DATA ACQUISITION	12
1.	Satellite Tracking.....	12
2.	Data Pre-Processing	13
IV.	METHODS	15
A.	REGIONS.....	15
B.	EULERIAN STATISTICS	16
1.	Binning	16
a.	Statistics	17
b.	Mesoscale.....	17
c.	Sensitivity.....	18
d.	Geographical Bin Spacing.....	19
2.	Eulerian Calculations.....	20
C.	SEASONALITY.....	21
D.	WIND CORRECTION.....	22
1.	Comparison Method	22
2.	Correlation Method	24
3.	Application of Correction Derived Outside this Study	24
E.	ARRAY BIAS	26
F.	LAGRANGIAN STATISTICS	27
V.	RESULTS.....	31
A.	EULERIAN.....	31
1.	Region 1: The Alboran Sea/Algerian Current	32
2.	Region 2: The Ionian Sea	35
3.	Region 3: The Adriatic Sea/Tyrrhenian Sea.....	37
4.	Region 4: The Levantine Sea.....	38
B.	SEASONALITY.....	40
1.	Region 2: The Ionian Sea	40
2.	Region 3: The Adriatic Sea/Tyrrhenian Sea.....	42
C.	ARRAY BIAS	42

1.	<i>Region 1: The Alboran Sea/Algerian Current</i>	42
2.	<i>Region 2: The Ionian Sea</i>	42
3.	<i>Region 3: The Adriatic Sea/Tyrrhenian Sea</i>	43
4.	<i>Region 4: The Levantine Sea</i>	43
D.	LAGRANGIAN	43
1.	<i>Region 1: The Alboran Sea/Algerian Current</i>	44
2.	<i>Region 2: The Ionian Sea</i>	45
3.	<i>Region 3: The Adriatic Sea/Tyrrhenian Sea</i>	45
4.	<i>Region 4: The Levantine Sea</i>	46
VI.	DISCUSSION AND CONCLUSIONS	47
VII.	RECOMMENDATIONS FOR FUTURE WORK	51
	LIST OF REFERENCES	111
	INITIAL DISTRIBUTION LIST	115

LIST OF FIGURES

FIGURE 1. MEDITERRANEAN SEA WITH AREAS OF INTEREST LABELED.....	55
FIGURE 2. MEDITERRANEAN GEOSTROPHIC SURFACE CURRENTS DERIVED FROM HYDROGRAPHIC DATA IN WINTER (FROM OVCHINNIKOV, 1966).	56
FIGURE 3. CIRCULATION PATHS OF THE MODIFIED ATLANTIC WATER (MAW) AND THE WINTER INTERMEDIATE WATER (WIW) IN THE WESTERN MEDITERRANEAN BASIN (FROM MILLOT, 1999). ...	56
FIGURE 4. IONIAN SEA UPPER THERMOCLINE CIRCULATION. SOLID LINES DENOTE PERMANENT DYNAMIC FEATURES. DASHED LINES MARK WATER MASS PATHWAYS (FROM MALANOTTE-RIZZOLI ET AL., 1997).	57
FIGURE 5. UPPER THERMOCLINE GENERAL CIRCULATION OBTAINED FROM MELDING OF DATA AND DYNAMICS IN THE EASTERN MEDITERRANEAN BASIN (FROM ROBINSON AND GOLNARAGHI, 1993).....	57
FIGURE 6. DISTRIBUTION OF THE TOTAL NUMBER OF DRIFTERS FOR THE FIVE DRIFTER TYPES (CODE, CMOD, SVP/TRISTAR, A111/A104, AND OTHER-DENOTED TELE).	58
FIGURE 7. DISTRIBUTION OF THE TOTAL NUMBER OF THE TOTAL 6-HOURLY DRIFTER OBSERVATION POINTS FOR THE FIVE DRIFTER TYPES (CODE, CMOD, SVP/TRISTAR, A111/A104, AND OTHER-DENOTED TELE).	58
FIGURE 8. PHOTOGRAPH AND SCHEMATIC DIAGRAM OF THE MODIFIED CODE DRIFTER (FROM POULAIN ET AL., 2000A).....	59
FIGURE 9. SCHEMATICS OF THE CMOD DRIFTER COMPONENTS AND FLOATING CHARACTERISTICS (FROM POULAIN ET AL., 2000A).	60
FIGURE 10. DRIFTER COVERAGE BY MONTH AND YEAR. THE NUMBER OF DRIFTER DAYS (FOUR 6-HOURLY OBSERVATIONS) IS PLOTTED FOR EACH MONTH OF EACH YEAR	61
FIGURE 11. DRIFTER DEPLOYMENT POSITIONS. THE DOTS ARE COLOR-CODED WITH RESPECT TO THE DRIFTER TYPE.....	62
FIGURE 12. DRIFTER TERMINATION POSITIONS. THE DOTS ARE COLOR-CODED WITH RESPECT TO THE DRIFTER TYPE.....	63
FIGURE 13. REGIONS OF STUDY. THE REGIONS OVERLAP ONE ANOTHER, BUT ALL REGIONS ARE RECTANGULAR AS DEFINED BY LATITUDE AND LONGITUDE LINES. THE POSITIONS OF THE 6-HOURLY OBSERVATIONS ARE OVERLAID IN RED.	64
FIGURE 14. SENSITIVITY ANALYSIS FOR REGIONS 1-4. FOR EACH REGION, EULERIAN STATISTICS UTILIZING BINS OF VARYING SIZES WERE COMPUTED. THE AVERAGE ENERGIES (MKE AND EKE) OF ALL THE BINS REQUIRED TO COVER THE REGION IS DISPLAYED FOR EACH BIN SIZE (BIN SIZE REFERS TO THE RADIUS OF THE CIRCULAR BINS).	65
FIGURE 15. BIN CENTERS. THE LOCATIONS OF 40 KM RADIUS CIRCULAR BIN CENTERS ARE DENOTED FOR UNIFORM BIN SPACING BETWEEN BIN CENTERS.....	66
FIGURE 16. BIN SHAPE AND DISTRIBUTION. SCHEMATIC SHOWS ON A MERCATOR PROJECTION THE LOCATIONS AND ORIENTATION OF 40 KM RADIUS CIRCULAR BINS WITH 40 KM BETWEEN BIN CENTERS.....	66
FIGURE 17. SEASONAL ANALYSIS. FOR 40 KM RADIUS BINS WITH 40 KM SPACING BETWEEN BIN CENTERS, THE EKE AND MKE AVERAGED OVER ALL BINS IS DISPLAYED FOR THE SIX MONTH PERIOD BEGINNING WITH THE MONTH ANNOTATED. RESULTS ARE SHOWN FOR REGIONS 1 THROUGH 4.....	67
FIGURE 18. DISTRIBUTION OF THE MAGNITUDE OF WIND SLIPPAGE CORRECTION FOR INDIVIDUAL CODE DRIFTER VELOCITIES FROM 1995 IN REGION 3.....	68
FIGURE 19. DISTRIBUTION OF THE MAGNITUDE OF THE DIFFERENCE BETWEEN BIN AVERAGE VELOCITIES FOR CORRECTED AND UNCORRECTED DRIFTER DATA (CODE DRIFTERS IN 1995 FOR REGION 3).	68
FIGURE 20. CORRECTION OF CODE DRIFTER WIND SLIPPAGE. THE BLUE (RED) ARROWS INDICATE THE UNCORRECTED (CORRECTED) BIN AVERAGES OF CODE DRIFTER VELOCITIES FROM 1995 IN REGION 3 USING 40 KM RADIUS CIRCULAR BINS WHOSE CENTERS ARE SPACED AT 40 KM.	69
FIGURE 21. REGION 1 DRIFTER OBSERVATIONS. EACH 6-HOURLY DRIFTER OBSERVATION, WHICH FALLS WITHIN ANY OF THE 40 KM RADIUS CIRCULAR BINS USED TO COVER THE ENTIRE AREA OF THE REGION, IS PLOTTED.	70

FIGURE 22. REGION 1 DATA DENSITY. THE TOTAL NUMBER OF 6-HOURLY DRIFTER OBSERVATIONS PER 40 KM RADIUS CIRCULAR BIN IS DISPLAYED AT THE BIN'S CENTER. A SQUARE COLOR PATCH IS ALSO DISPLAYED AT THE BINS CENTER INDICATING THE SAME QUANTITY. A NUMBER WITHIN AN UNCOLORED PATCH INDICATES THAT THE BIN DID NOT MEET THE THRESHOLD CRITERION OF 40 6-HOURLY DRIFTER OBSERVATIONS.....	71
FIGURE 23. REGION 1 MKE. THE MEAN KINETIC ENERGY (MKE) PER 40 KM RADIUS CIRCULAR BIN IS DISPLAYED AT THE BIN'S CENTER. A SQUARE COLOR PATCH IS ALSO DISPLAYED AT THE BINS CENTER INDICATING THE SAME QUANTITY. A NUMBER WITHIN AN UNCOLORED PATCH INDICATES THAT THE BIN DID NOT MEET THE THRESHOLD CRITERION OF 40 6-HOURLY DRIFTER OBSERVATIONS.	72
FIGURE 24. REGION 1 EKE. THE EDDY KINETIC ENERGY (EKE) PER 40 KM RADIUS CIRCULAR BIN IS DISPLAYED AT THE BIN'S CENTER. A SQUARE COLOR PATCH IS ALSO DISPLAYED AT THE BINS CENTER INDICATING THE SAME QUANTITY. A NUMBER WITHIN AN UNCOLORED PATCH INDICATES THAT THE BIN DID NOT MEET THE THRESHOLD CRITERION OF 40 6-HOURLY DRIFTER OBSERVATIONS.	73
FIGURE 25. REGION 1 SURFACE FLOW. THE AVERAGE DRIFTER VELOCITY PER 40 KM RADIUS CIRCULAR BIN IS DISPLAYED AT THE CENTER OF MASS OF THE DRIFTER OBSERVATIONS WITHIN EACH BIN.	74
FIGURE 26. REGION 1 SURFACE FLOW VARIANCE. AN ELLIPSE DEFINED BY THE PRINCIPAL AXES OF VARIANCE FOR EACH BIN REPRESENTS VARIANCE OF SURFACE FLOW. THE ELLIPSE IS CENTERED AT THE CENTER OF MASS OF THE DRIFTER OBSERVATIONS WITHIN EACH BIN.....	75
FIGURE 27. REGION 2 DRIFTER OBSERVATIONS. EACH 6-HOURLY DRIFTER OBSERVATION, WHICH FALLS WITHIN ANY OF THE 40 KM RADIUS CIRCULAR BINS USED TO COVER THE ENTIRE AREA OF THE REGION, IS PLOTTED.	76
FIGURE 28. REGION 2 DATA DENSITY. THE TOTAL NUMBER OF 6-HOURLY DRIFTER OBSERVATIONS PER 40 KM RADIUS CIRCULAR BIN IS DISPLAYED AT THE BIN'S CENTER. A SQUARE COLOR PATCH IS ALSO DISPLAYED AT THE BINS CENTER INDICATING THE SAME QUANTITY. A NUMBER WITHIN AN UNCOLORED PATCH INDICATES THAT THE BIN DID NOT MEET THE THRESHOLD CRITERION OF 40 6-HOURLY DRIFTER OBSERVATIONS.....	77
FIGURE 29. REGION 2 MKE. THE MEAN KINETIC ENERGY (MKE) PER 40 KM RADIUS CIRCULAR BIN IS DISPLAYED AT THE BIN'S CENTER. A SQUARE COLOR PATCH IS ALSO DISPLAYED AT THE BINS CENTER INDICATING THE SAME QUANTITY. A NUMBER WITHIN AN UNCOLORED PATCH INDICATES THAT THE BIN DID NOT MEET THE THRESHOLD CRITERION OF 40 6-HOURLY DRIFTER OBSERVATIONS.	78
FIGURE 30. REGION 2 EKE. THE EDDY KINETIC ENERGY (EKE) PER 40 KM RADIUS CIRCULAR BIN IS DISPLAYED AT THE BIN'S CENTER. A SQUARE COLOR PATCH IS ALSO DISPLAYED AT THE BINS CENTER INDICATING THE SAME QUANTITY. A NUMBER WITHIN AN UNCOLORED PATCH INDICATES THAT THE BIN DID NOT MEET THE THRESHOLD CRITERION OF 40 6-HOURLY DRIFTER OBSERVATIONS.	79
FIGURE 31. REGION 2 SURFACE FLOW. THE AVERAGE DRIFTER VELOCITY PER 40 KM RADIUS CIRCULAR BIN IS DISPLAYED AT THE CENTER OF MASS OF THE DRIFTER OBSERVATIONS WITHIN EACH BIN.	80
FIGURE 32. REGION 2 FLOW VARIANCE. AN ELLIPSE DEFINED BY THE PRINCIPAL AXES OF VARIANCE FOR EACH BIN REPRESENTS VARIANCE OF SURFACE FLOW. THE ELLIPSE IS CENTERED AT THE CENTER OF MASS OF THE DRIFTER OBSERVATIONS WITHIN EACH BIN.....	81
FIGURE 33. REGION 3 DRIFTER OBSERVATIONS. EACH 6-HOURLY DRIFTER OBSERVATION, WHICH FALLS WITHIN ANY OF THE 40 KM RADIUS CIRCULAR BINS USED TO COVER THE ENTIRE AREA OF THE REGION, IS PLOTTED.	82
FIGURE 34. REGION 3 DATA DENSITY. THE TOTAL NUMBER OF 6-HOURLY DRIFTER OBSERVATIONS PER 40 KM RADIUS CIRCULAR BIN IS DISPLAYED AT THE BIN'S CENTER. A SQUARE COLOR PATCH IS ALSO DISPLAYED AT THE BINS CENTER INDICATING THE SAME QUANTITY. A NUMBER WITHIN AN UNCOLORED PATCH INDICATES THAT THE BIN DID NOT MEET THE THRESHOLD CRITERION OF 40 6-HOURLY DRIFTER OBSERVATIONS.....	83
FIGURE 35. REGION 3 MKE. THE MEAN KINETIC ENERGY (MKE) PER 40 KM RADIUS CIRCULAR BIN IS DISPLAYED AT THE BIN'S CENTER. A SQUARE COLOR PATCH IS ALSO DISPLAYED AT THE BINS CENTER INDICATING THE SAME QUANTITY. A NUMBER WITHIN AN UNCOLORED PATCH INDICATES THAT THE BIN DID NOT MEET THE THRESHOLD CRITERION OF 40 6-HOURLY DRIFTER OBSERVATIONS.	84

FIGURE 36. REGION 3 EKE. THE EDDY KINETIC ENERGY (EKE) PER 40 KM RADIUS CIRCULAR BIN IS DISPLAYED AT THE BIN'S CENTER. A SQUARE COLOR PATCH IS ALSO DISPLAYED AT THE BINS CENTER INDICATING THE SAME QUANTITY. A NUMBER WITHIN AN UNCOLORED PATCH INDICATES THAT THE BIN DID NOT MEET THE THRESHOLD CRITERION OF 40 6-HOURLY DRIFTER OBSERVATIONS.	85
FIGURE 37. REGION 3 SURFACE FLOW. THE AVERAGE DRIFTER VELOCITY PER 40 KM RADIUS CIRCULAR BIN IS DISPLAYED AT THE CENTER OF MASS OF THE DRIFTER OBSERVATIONS WITHIN EACH BIN.	86
FIGURE 38. REGION 3 FLOW VARIANCE. AN ELLIPSE DEFINED BY THE PRINCIPAL AXES OF VARIANCE FOR EACH BIN REPRESENTS VARIANCE OF SURFACE FLOW. THE ELLIPSE IS CENTERED AT THE CENTER OF MASS OF THE DRIFTER OBSERVATIONS WITHIN EACH BIN.....	87
FIGURE 39. REGION 4 DRIFTER OBSERVATIONS. EACH 6-HOURLY DRIFTER OBSERVATION, WHICH FALLS WITHIN ANY OF THE 40 KM RADIUS CIRCULAR BINS USED TO COVER THE ENTIRE AREA OF THE REGION, IS PLOTTED.	88
FIGURE 40. REGION 4 DATA DENSITY. THE TOTAL NUMBER OF 6-HOURLY DRIFTER OBSERVATIONS PER 40 KM RADIUS CIRCULAR BIN IS DISPLAYED AT THE BIN'S CENTER. A SQUARE COLOR PATCH IS ALSO DISPLAYED AT THE BINS CENTER INDICATING THE SAME QUANTITY. A NUMBER WITHIN AN UNCOLORED PATCH INDICATES THAT THE BIN DID NOT MEET THE THRESHOLD CRITERION OF 40 6-HOURLY DRIFTER OBSERVATIONS.....	89
FIGURE 41. REGION 4 MKE. THE MEAN KINETIC ENERGY (MKE) PER 40 KM RADIUS CIRCULAR BIN IS DISPLAYED AT THE BIN'S CENTER. A SQUARE COLOR PATCH IS ALSO DISPLAYED AT THE BINS CENTER INDICATING THE SAME QUANTITY. A NUMBER WITHIN AN UNCOLORED PATCH INDICATES THAT THE BIN DID NOT MEET THE THRESHOLD CRITERION OF 40 6-HOURLY DRIFTER OBSERVATIONS.	90
FIGURE 42. REGION 4 EKE. THE EDDY KINETIC ENERGY (EKE) PER 40 KM RADIUS CIRCULAR BIN IS DISPLAYED AT THE BIN'S CENTER. A SQUARE COLOR PATCH IS ALSO DISPLAYED AT THE BINS CENTER INDICATING THE SAME QUANTITY. A NUMBER WITHIN AN UNCOLORED PATCH INDICATES THAT THE BIN DID NOT MEET THE THRESHOLD CRITERION OF 40 6-HOURLY DRIFTER OBSERVATIONS.	91
FIGURE 43. REGION 4 SURFACE FLOW. THE AVERAGE DRIFTER VELOCITY PER 40 KM RADIUS CIRCULAR BIN IS DISPLAYED AT THE CENTER OF MASS OF DRIFTER OBSERVATIONS WITHIN EACH BIN.	92
FIGURE 44. REGION 4 FLOW VARIANCE. AN ELLIPSE DEFINED BY THE PRINCIPAL AXES OF VARIANCE FOR EACH BIN REPRESENTS VARIANCE OF SURFACE FLOW. THE ELLIPSE IS CENTERED AT THE CENTER OF MASS OF THE DRIFTER OBSERVATIONS WITHIN EACH BIN.....	93
FIGURE 45. REGION 2 WINTER 6-HOURLY OBSERVATIONS. EACH WINTER 6-HOURLY DRIFTER OBSERVATION, WHICH FALLS WITHIN ANY OF THE 40 KM RADIUS CIRCULAR BINS USED TO COVER THE ENTIRE AREA OF THE REGION, IS PLOTTED. WINTER IS CONSIDERED AS THE 6-MONTH PERIOD BEGINNING IN NOVEMBER AND ENDING IN APRIL.....	94
FIGURE 46. REGION 2 SUMMER 6-HOURLY OBSERVATIONS. EACH SUMMER 6-HOURLY DRIFTER OBSERVATION, WHICH FALLS WITHIN ANY OF THE 40 KM RADIUS CIRCULAR BINS USED TO COVER THE ENTIRE AREA OF THE REGION, IS PLOTTED. SUMMER IS DEFINED AS THE 6-MONTH PERIOD BEGINNING IN MAY AND ENDING IN OCTOBER.....	95
FIGURE 47. REGION 2 WINTER DATA DENSITY. THE TOTAL NUMBER OF WINTER 6-HOURLY DRIFTER OBSERVATIONS PER 40 KM RADIUS CIRCULAR BIN IS DISPLAYED AT THE BIN'S CENTER. A SQUARE COLOR PATCH IS ALSO DISPLAYED AT THE BINS CENTER INDICATING THE SAME QUANTITY. A NUMBER WITHIN AN UNCOLORED PATCH INDICATES THAT THE BIN DID NOT MEET THE THRESHOLD CRITERION OF 40 6-HOURLY DRIFTER OBSERVATIONS. WINTER IS DEFINED AS THE 6-MONTH PERIOD BEGINNING IN NOVEMBER AND ENDING IN APRIL.	96
FIGURE 48. REGION 2 SUMMER DATA DENSITY. THE TOTAL NUMBER OF SUMMER 6-HOURLY DRIFTER OBSERVATIONS PER 40 KM RADIUS CIRCULAR BIN IS DISPLAYED AT THE BIN'S CENTER. A SQUARE COLOR PATCH IS ALSO DISPLAYED AT THE BINS CENTER INDICATING THE SAME QUANTITY. A NUMBER WITHIN AN UNCOLORED PATCH INDICATES THAT THE BIN DID NOT MEET THE THRESHOLD CRITERION OF 40 6-HOURLY DRIFTER OBSERVATIONS. SUMMER IS DEFINED AS THE 6-MONTH PERIOD BEGINNING IN MAY AND ENDING IN OCTOBER.....	97

FIGURE 49. REGION 2 WINTER SURFACE FLOW. THE AVERAGE DRIFTER VELOCITY PER 40 KM RADIUS CIRCULAR BIN IS DISPLAYED AT THE CENTER OF MASS OF DRIFTER OBSERVATIONS WITHIN EACH BIN. WINTER IS DEFINED AS THE 6-MONTH PERIOD BEGINNING IN NOVEMBER AND ENDING IN APRIL.	98
FIGURE 50. REGION 2 SUMMER SURFACE FLOW. THE AVERAGE DRIFTER VELOCITY PER 40 KM RADIUS CIRCULAR BIN IS DISPLAYED AT THE CENTER OF MASS OF DRIFTER OBSERVATIONS WITHIN EACH BIN. SUMMER IS DEFINED AS THE 6-MONTH PERIOD BEGINNING IN MAY AND ENDING IN OCTOBER.	99
FIGURE 51. REGION 2 WINTER FLOW VARIANCE. AN ELLIPSE DEFINED BY THE PRINCIPAL AXES OF VARIANCE FOR EACH BIN REPRESENTS VARIANCE OF SURFACE FLOW. THE ELLIPSE IS CENTERED AT THE CENTER OF MASS OF DRIFTER OBSERVATIONS WITHIN EACH BIN. WINTER IS DEFINED AS THE 6-MONTH PERIOD BEGINNING IN NOVEMBER AND ENDING IN APRIL.	100
FIGURE 52. REGION 2 SUMMER FLOW VARIANCE. AN ELLIPSE DEFINED BY THE PRINCIPAL AXES OF VARIANCE FOR EACH BIN REPRESENTS VARIANCE OF SURFACE FLOW. THE ELLIPSE IS CENTERED AT THE CENTER OF MASS OF DRIFTER OBSERVATIONS WITHIN EACH BIN. SUMMER IS DEFINED AS THE 6-MONTH PERIOD BEGINNING IN MAY AND ENDING IN OCTOBER.	101
FIGURE 53. REGION 2 ARRAY BIAS. THE ARRAY BIAS PER 40 KM RADIUS CIRCULAR BIN IS DISPLAYED AT THE CENTER OF MASS OF DRIFTER OBSERVATIONS WITHIN EACH BIN.	102
FIGURE 54. REGION 2 SURFACE FLOW (ARRAY BIAS CORRECTED). THE MEAN SURFACE FLOW CORRECTED (RED) AND UNCORRECTED (BLUE) FOR THE ARRAY BIAS PER 40 KM RADIUS CIRCULAR BIN IS DISPLAYED AT THE CENTER OF MASS OF DRIFTER OBSERVATIONS WITHIN EACH BIN.	103
FIGURE 55. REGION 1 LAGRANGIAN STATISTICS WITHOUT (LEFT) AND WITH (RIGHT) THE EULERIAN MEAN FLOW REMOVED FOR TIME LAGS BETWEEN+ 20 AND -20 DAYS.	104
FIGURE 56. REGION 2 LAGRANGIAN STATISTICS WITHOUT (LEFT) AND WITH (RIGHT) THE EULERIAN MEAN FLOW REMOVED FOR TIME LAGS BETWEEN+ 20 AND -20 DAYS.	105
FIGURE 57. REGION 3 LAGRANGIAN STATISTICS WITHOUT (LEFT) AND WITH (RIGHT) THE EULERIAN MEAN FLOW REMOVED FOR TIME LAGS BETWEEN+ 20 AND -20 DAYS.	106
FIGURE 58. REGION 4 LAGRANGIAN STATISTICS WITHOUT (LEFT) AND WITH (RIGHT) THE EULERIAN MEAN FLOW REMOVED FOR TIME LAGS BETWEEN+ 20 AND -20 DAYS.	107
FIGURE 59. MEDITERRANEAN SEA SURFACE CIRCULATION DERIVED FROM DRIFTER DATA (1986-1999). ARROWS INDICATE THE LOCATIONS AND DIRECTIONS OF THE MAJOR CURRENTS OBSERVED, BUT DO NOT INDICATE THE RELATIVE STRENGTH OF THE CURRENTS.	109

LIST OF TABLES

TABLE 1. DRIFTER TYPES WITH ORIGIN.....	53
TABLE 2. CORRECTED LAGRANGIAN STATISTICS (WITH THE EULERIAN MEAN FLOW REMOVED): VELOCITY VARIANCE, DIFFUSIVITY, AND LAGRANGIAN TIME AND LENGTH SCALES FOR REGIONS 1-4.	53

ACKNOWLEDGEMENT

First and foremost, I would like to thank Dr. Pierre-Marie Poulain for his support throughout this thesis effort. I consider his patience, insight, and intellect as invaluable to this body of work.

The following institutions are acknowledged for deploying drifters in the Mediterranean Sea and making their data available: Naval Postgraduate School, California; SACLANT Undersea Research Centre, Italy; Naval Oceanography Office, Mississippi; Consejo Superior de Investigaciones Cientificas, Spain; Centre National de la Recherche Scientifique, France; Ente per le Nuove Tecnologie, l'Energia e l'Ambiente, Italy; Istituto Universitario Navale, Italy; Telespazio, Italy; Istituto Nazionale di Oceanografia e di Geofisica Sperimentale, Italy; and Stazione Zoologica di Napoli, Italy.

I would also like to thank my wife and partner in life, Karen, for her enduring support.

I. INTRODUCTION

As the United States Navy is evolving from the open ocean Cold War super power to the littoral water peacekeeper, it is faced with new problems and obstacles. In the past ten years, the Navy has extended itself into the coastal areas of mostly third world nations which depend on mine warfare, including internationally prohibited drifting mines, for an inexpensive yet effective defense. In the Mediterranean Sea, which has been the location of a majority of the latest conflicts, oceanographic studies have been conducted by a variety of institutions to describe the spatial structure and temporal variability of the surface circulation. These studies date to the 1960's (Ovchinnikov, 1966) to the present (Poulain, 2000), and in many cases conflict with one another to the degree of showing flow in opposite directions. The lack and dissimilarity of surface current information has severely hampered operations on several occasions in the presence of a drifting mine threat.

This study analyzes data from 521 different drifters deployed throughout the Mediterranean Sea from 1986 to 1999 in order to resolve conflicting information and provide information where none is present. Eulerian and Lagrangian surface circulation statistics are examined for most of the Mediterranean Sea.

An Eulerian grid system is employed to best represent flow throughout the Mediterranean Sea as a combination of a deterministic mean and fluctuations due to temporal and mesoscale variability. The results of the Eulerian statistics are presented as

charts of Mean Kinetic Energy (MKE), Eddy Kinetic Energy (EKE), mean flow, and velocity variance.

Seasonal variation is also addressed where temporal and spatial distribution of the data is adequate. Errors inherent to drifter data due to array bias and wind slippage are investigated for possible correction.

Lagrangian statistics of diffusivity, velocity covariance, integral time and length scales are evaluated to characterize the dispersion properties of the fluctuating currents.

This thesis is organized as follows: Section II provides background information and introduces significant studies in the Mediterranean Sea. Section III describes the drifter systems utilized, deployment characteristics of the drifters, acquisition of drifter data, and the pre-processing of the raw data. Eulerian and Lagrangian methods are presented in Section IV along with the techniques used to evaluate seasonality and errors due to wind slippage and array bias. The results are presented in Section V with the discussion and conclusions in Section VI. The last section, Section VII, contains recommendations for future work.

II. BACKGROUND

A. MEDITERRANEAN SEA GENERAL CHARACTERISTICS

The Mediterranean Sea can be described as an inverse estuary, mid-latitude evaporation basin. This semi-enclosed basin communicates with the Atlantic Ocean through the Strait of Gibraltar (sill depth approximately 300 *m* with a width of 14 *km*). The magnitude of water lost through evaporative processes throughout the Mediterranean Sea dominates the rain and river run-off into the basin. Atlantic water flows into the Mediterranean Sea at the surface through the Strait of Gibraltar while saltier Mediterranean water flows into the Atlantic Ocean subsurface through the strait.

The Mediterranean Sea is further divided by the presence of other sills. The Strait of Sicily (average depth of 500 *m* with a width of 78 *km*) is another important sill that separates the Mediterranean Sea into two major basins. The Western Mediterranean Basin is composed of the Tyrrhenian Sea, Ligurian Sea, Balearic Sea, and the Alboran Sea. The Eastern Mediterranean Basin is composed of the Ionian Sea, Adriatic Sea, Levantine Sea, and the Aegean Sea (Figure 1). Another sill of major importance separates the Adriatic Sea from the rest of the Eastern Mediterranean Basin (the Otranto Strait has an average depth of approximately 325 *m* with a width of 75 *km*).

The Mediterranean Sea floor has an average depth of about 1.5 *km* with 30% of the surface area between 2-3 *km* and 25% less than 200 *m*. With the exception of the Algerian Basin (which is remarkably flat), the Mediterranean Sea floor is characterized by

rugged terrain alternating between trenches and islands. The Mediterranean Sea with areas of interest is noted in Figure 1.

B. MEDITERRANEAN SURFACE CIRCULATION

Based on temperature and salinity values, the well-known Ovchinnikov (1966) geostrophic current chart outline the major surface current-pathways in the Mediterranean Sea (Figure 2).

Atlantic water entering the Mediterranean Sea at the surface of the Strait of Gibraltar is isolated from the Mediterranean water by two adjacent gyres east of the Strait of Gibraltar (along with the Almeria-Oran front). The Western Alboran Gyre is east of the Strait of Gibraltar. Although it is a quasi-permanent anticyclonic feature, the Western Alboran Gyre displays large variability of its shape, location and strength. The second gyre, the Eastern Alboran Gyre, is not always observable, and has been noted as being either cyclonic or anticyclonic (Milot, 1999). The Algerian basin acts as a reservoir for mixing the incoming Atlantic water and the already present Mediterranean water. The result of this mixing is the Modified Atlantic Water (MAW) and forms the Algerian Current, a strong current traveling eastward along the northern coast of Africa. Circulation in the Algerian basin is supported by large cyclonic gyres that spin off of the Algerian Current and travel northeast over the Algerian basin (Milot, 1999). Figure 3 displays this surface circulation in the Algerian Basin. Westward flow is evident off the coast of Italy to Spain along the northern boundary of the Mediterranean Sea (with a notable sinking zone in the Ligurian Sea). Mediterranean flow to the Atlantic Ocean of

salty Levantine Intermediate Water (LIW, formed by sinking MAW between Rhodes and Cyprus in the Eastern Mediterranean Basin) occurs in a deep layer through the Strait of Gibraltar (LIW flows from the Eastern Mediterranean Basin to the Western Mediterranean Basin in a deep layer through the Strait of Sicily).

At the surface of the Strait of Sicily, the flow is eastward as MAW travels from the Western Mediterranean Basin to the Eastern Mediterranean Basin. The eastward surface flow through the Strait of Sicily forms the Atlantic-Ionian Stream (AIS) that disassociates itself from the coast just after the strait (Robinson et al., 1999). This stream is less well defined and not as focused as the Algerian Current. The AIS turns north just east of Sicily and branches into two components (one turning south and the other continuing north) near the tip of Italy (Robinson and Golnaraghi, 1993; Malanotte-Rizzoli et al., 1997). This northward flow along the east coast of Italy continues to follow the coast of the basin forming an anticyclonic gyre circulation (North Ionian Gyre) in the north Ionian Sea and a southward current (the Mid-Ionian Jet, MIJ) in the center of the Ionian basin. Figure 4 shows the typical flow path of the AIS, its extension in the northern Ionian Sea, and the MIJ. A reversal of flow (northward to southward) has been observed east of Sicily and Italy in the Northern Ionian using satellite altimetry (Larnicol et al., 1995), which results in cyclonic circulation of the North Ionian Gyre in winter. This cyclonic gyre has also been noted in numerical simulations with real atmospheric forcing by Pinardi et al. (1997) and in geostrophic component analysis by Ovchinnikov (1966).

Regardless of the exact path of the AIS, flow in the Eastern Mediterranean Basin is characterized by several stable sub-basin gyres that extend often to the sea floor

(Robinson and Golnaraghi, 1993). These gyres tend to be cyclonic when formed north of the AIS or Mid-Mediterranean Jet (MMJ, and extension of the AIS as it enters the Levantine Sea) and anticyclonic when formed south of the stream (Figure 5). Evaporation increases further east in this basin and results in a sinking zone in the northern portion of the Levantine Sea.

Circulation into the Adriatic Sea from the Eastern Mediterranean Basin is present on the eastern side of the Otranto Strait, and is out of the Adriatic on the western side. Within the Adriatic Sea, basin-wide circulation is cyclonic. Sub-basin circulation in the Adriatic Sea is significantly affected by topography resulting in four cyclonic sub-basin gyres extending laterally along the basin (Artegiani et al., 1997; Poulain, 1999; Poulain, 2000).

C. SEASONAL VARIABILITY

Due to the significant change in winds on a seasonal scale, surface and intermediate circulations have seasonal variations (although the extent and magnitude of this effect are arguable). Winter is characterized by strong predominately westerly winds over most of the Mediterranean basin with most of the precipitation occurring during this season. By summer, these winds shift predominately to the north and decrease in magnitude. The mean of the wind stress curl over the Ionian Sea fluctuates widely but has a mean of approximately zero (Pinardi and Navarra, 1993). This seasonal variation results in a cyclonic North Ionian Gyre in the winter vice an anticyclonic gyre in the summer. Seasonal influence in the north Ionian Sea, however, does not always result in

the reversal of flow of the North Ionian Gyre. Pinardi et al. (1997) describes the circulation of the North Ionian Gyre reversing flow only one year out of a four-year study. The influence of interannual variability could play a key role in preventing seasonal influences from reversing the flow of the North Ionian Gyre.

D. DRIFTER STUDIES

The first drifter studies in the Mediterranean Sea were conducted through observations of cards and bottles (Mazelle, 1914; Feruglio, 1920). These initial Lagrangian studies could only interpret the displacement of drifters (from the deployment position and point of recovery) during a known time period (from the time of deployment to the time of recovery). These studies were unable to properly deal with uncertainties in time, wind and wave effects, and trajectory path.

Satellite technology allowed the tracking of drifting instrument with increasing position accuracy. This type of tracking resolved time and position uncertainties to acceptable levels of error. Slippage from wind and wave effects continued to decrease as efficient buoy designs with better water-following abilities were developed.

Drifter studies utilizing satellite-tracking technology were conducted in limited portions of the Mediterranean Sea using limited drifter sets as early as the 1980's (Millot, 1999). Borzelli et al. (1992) studied the northern Adriatic Sea in 1990. Salas et al. (2000) and Font et al. (1998) analyzed the surface characteristics of the Algerian Current. As available drifter data increased, Matteoda and Glenn (1996) studied recurrent mesoscale eddies in the eastern Mediterranean using 100 drifters. Most recently, a drifter

data set of 201 satellite-tracked drifters spanning nine years was used to study the Adriatic Sea (Poulain and Zanasca, 1998; Poulain, 1999; Poulain, 2000). As data from more drifters become available, studies can incorporate larger areas while maintaining or even increasing the resolution of statistical results.

III. DATA

A. BUOY DESCRIPTIONS

The data available for this study include 521 individual drifters. In order to preserve the identity of different drifter styles, each drifter was treated as one of 5 types. The distribution between these types is summarized in Table 1 and Figure 6. Because the lifetime of each drifter is unique, Figure 7 displays the available 6-hour data points among the drifter types.

1. CODE

Type 1 drifters are all of the modified CODE type construction. CODE refers to the type of drifter used in the Coastal Dynamics Experiment in the early 1980's (Davis, 1985). Manufactured by Technocean, Cape Coral, Florida, USA, this type of drifter houses the electronics within a 1-*m* long undrogued tube. A transmitting antenna extends from the top of the tube. Radially protruding out of the tube, four identical vanes, which extend the entire length of the tube, reduce the drifter's slip. Four spherical floats attached to the upper portion of each vane provide buoyancy. Figure 8 shows a schematic diagram of the drifter.

Measurements have been conducted on this type of drifter to analytically represent their ability to follow mean flow in the presence of wind and wave action. Velocities derived from CODE drifters were found to be accurate to about 3 *cm/s* (mostly wind-induced slippage error) even under strong wind conditions by studies using current meters

(Davis, 1985) and dye (D. Olson, Personal Communication) to measure the movement of water in the area around the drifters.

Although not a majority, CODE type drifters comprise the largest type of drifters in this study. Of the 521 drifters, 247 are of the CODE type (47.4%).

2. CMOD

Type 2 drifters include Compact Meteorological and Oceanographic Drifters (CMOD). Developed by Metocean, Dartmouth, Nova Scotia, Canada, these drifters are drogued sonobuoys. A 60 cm long aluminum cylindrical tube houses the electronics with a sonobuoy case drogued at 100 *m* or 4 *m*. A flotation collar fitted on the tube provides buoyancy (Figure 9). With the drogue, the drifter boasts of a 5 to 1 wet to dry area ratio (Matteoda and Glenn, 1996).

CMOD type drifters used in this study comprise 42.6% of the total drifters with 41 drogued at 4 *m* and 181 drogued at 100 *m*.

3. SVP and TRISTAR

Type 3 drifters include Surface Velocity Program (SVP) and TRISTAR designs. This drifter employs two floats and a holey-sock (SVP) or TRISTAR drogue laterally tethered. The upper 35 cm fiberglass float houses the transmitter, antenna, battery, and sensors. A second subsurface 20 cm fiberglass float provides additional buoyancy and is located 307 cm below the upper float (Sybrandy et al., 1991; Niiler et al., 1995). In order to reduce slippage, these drifters employ the holey-sock type drogues at 10 and 300 *m* (SVP) or the TRISTAR type drogue at 10 *m*.

A total of 22 type 3 drifters are used in this study comprising 4.2% of the drifters. TRISTAR type drogued at 10 *m* total 7, while SVP comprise the remaining 15 (14 drogued at 15 *m* and 1 drogued at 300 *m*).

4. A111 and A104

Type 4 drifters are composed of drifters manufactured by Brightwaters Instrument Co., New York, USA designated models A111 and A104.

Model A111 houses the transmitter, antenna, and batteries within a vertical cylinder. Buoyancy is provided by a collar on the top end of the cylinder, and a subsurface float (provides buoyancy for the drogue). The drogue is a holey-sock type tethered at a 10 *m* depth. Model A104 is similar in design to the CODE drifter with the following additions. This model represents the only drifter design used in this study with a GPS receiver (although this data was not used). Model A104 also utilized a holey-sock drogue tethered at 10 *m*. Both A111/A104 models produced similar subsurface to surface drag ratios (Font et al., 1998; Salas et al., 2000).

These two models account for only 3.3% (17 drifters) of the total available drifters.

5. Other

Type 5 drifters total only 13 (making up 2.5% of the 521 drifters) and are described in Borzelli et al. (1992).

B. DEPLOYMENTS

Various institutions contributed to the drifters used in this study. Table 1 summarizes the institutions responsible for the various drifter deployments. Since many of the drifters were deployed in primary support of a variety of operational and scientific studies, the spatial and temporal coverage of the drifter data is not consistent. Figure 10 shows the temporal coverage for each year and month from June 2, 1986 to October 11, 1999. Only 6 drifters were deployed in 1986. All of these drifters terminated in 1986 or 1987. No data are present for 1988, and small drifter deployments began again in 1989. The early 1990's represent relatively low drifter numbers with the bulk of the drifters present in 1995 to 1997. There are also significant geographical areas where statistically relevant data are not present. Figure 11 shows the drifter deployment sites, and Figure 12 displays the drifter termination points. Significant lack of coverage exists in the Aegean Sea, Ligurian Sea, northeast Alboran Basin, and the northern portion of the Levantine Sea. Figure 13 shows the spatial coverage for the pre-processed data (pre-processing is outlined in the following section) of all 521 drifters.

C. DATA ACQUISITION

1. Satellite Tracking

No drifters used in this study incorporated onboard positioning capabilities (with the exception of A104 buoys equipped with a GPS receiver which were not used). Instead, the drifters were tracked by the Argos Data Location and Collection System (DCLS) carried onboard the NOAA polar-orbiting satellites. Positioning of the drifters is

determined by the Doppler shift of the signal transmitted by the drifter (401.65 *MHz*). The drifter transmits this signal every 1 to 2 minutes. The accuracy of the positioning is dependent on the number of signals received during the satellite's pass as well as the satellite's position (affecting the distance between the drifter and satellite). The Argos system employed exhibits about 11 fixes per day (utilizing two satellites) for the mid-latitudes of the Mediterranean Sea. Argos provides the accuracy of these fixes in terms of location classes. After considering the accuracy (location class), the fixes were edited for outliers. The remaining data exhibited about 8 fixes a day per transmitting drifter. With outliers edited, the mean position accuracy is estimated to be 200-300 *m* (Poulain, 2000). Some drifters were programmed to transmit one out of three days to utilize a special scientific reduced tariff. Comparing all drifters' lifetimes with the total time the drifters transmit in this discontinuous fashion, 21.5% of the transmission time was discontinuous.

2. Data Pre-Processing

The data from the Argos system was manually and statistically edited for outliers as described in Poulain et al. (2000a; 2000b). In order to provide uniform position information in time, the edited time series of drifter position was interpolated. The interpolation technique employed is known as "kriging" (Hansen and Poulain, 1996). The interpolated function was sub-sampled at 1-hour intervals. The 1-hour time series of drifter positions was then low pass filtered using a Hamming filter with cutoff period of 36 hours. 36 hours was chosen to eliminate the effects of inertial and tidal currents. The subsequent edited, "kriged," and filtered data were again sub-sampled. 6 hours was

chosen for this sub-sampling since smaller time intervals provided no significant gain for the loss of processing time. In order to obtain velocity components in zonal and meridional directions, the position data was used by centered finite differences to obtain velocities. Based on the accuracy of the Argos tracking system, manipulation of the data by manual and statistical despiking, smoothing of the data by interpolating and sub-sampling, filtering by the Hamming method, and final sub-sampling at 6 hour intervals, velocity derivations from centered finite differences have an estimated accuracy of 2-3 *cm/s* (Poulain, 1999).

Details on the drifter hardware, data processing, and resulting processed data are available on CD-ROM (Poulain et al., 2000b) and on the world wide web (Poulain et al., 2000a).

IV. METHODS

A. REGIONS

In order to more closely evaluate the large area of the Mediterranean Sea, overlapping regions with similar characteristics were chosen for evaluation. These regions are depicted in Figure 13.

Region 1 extends from 6° W to 14° E longitudes and from 35° N to 40° N latitudes. This region contains all of the statistically significant data in the Algerian Basin and Alboran Sea. It also contains the Algerian Current from its inception to and just beyond the Strait of Sicily. Most of the Ligurian Sea and Algerian Basin north of the Balearic Islands are not included in this region or any other due to the absence of relevant drifter observations.

Region 2 extends from 10° E to 24° E longitudes and from 30° N to 40° N latitudes. This region contains the entire Ionian Sea and extends through the Strait of Sicily. On its Eastern side, the region extends just past the western edge of the island of Crete.

Region 3 extends from 10° E to 21° E longitudes and from 38° N to 46° N latitudes. This region contains the entire Adriatic Sea as well as the Tyrrhenian Sea. The northern extremity of the Ionian Sea is also included to sufficiently show the effects of the Strait of Otranto.

Region 4 extends from 20° E to 37° E longitudes and from 31° N to 36° N latitudes. This region contains all but the northern extensions of the Levantine Sea. It

also contains a large portion of the Ionian Sea to adequately represent the effects of the island of Crete. Although a portion of the Aegean Sea is contained in this region, no relevant data exists there.

Region 5 extends from 6° W to 37° E longitudes and from 30° N to 46° N latitudes. This region encompasses the entire Mediterranean Sea. Although no new results are presented by the study of this area, it does offer a medium to present summary results on a large scale. This region is presented solely as a presentation and summary technique.

B. EULERIAN STATISTICS

Eulerian statistics are generally computed by averaging the drifter velocity data in a given geographic domain (called a bin) over a specific time period. In this thesis, data are only separated temporally when analyzing seasonal dependency. The binning process used in this study is described below.

1. Binning

In order to represent the Lagrangian drifter data in a commonly understood Eulerian reference, a spatial scale for averaging must be selected. Many factors are used to determine this critical parameter. The goal is to choose a bin size that sufficiently represents the flow as a relatively consistent mean current with residual fluctuations due to temporal and spatial variability within the bin.

a. Statistics

In order to achieve robust results, the bin size must be large enough to contain sufficient data within each bin order to reduce the variance of the resulting statistics. If however, the bins are too large, the results they give have little use due to poor resolution even though they may be statistically sound. To help resolve this contradiction, overlapping circular bin equally spaced at a radius' distance from each other were used. The overlapping of the bins allows for more robust statistics while maintaining increased resolution (at the sacrifice of smoothing the data results since the data used in adjacent bins are not independent or even unique). Due to the inadequacies in the spatial and temporal uniformity, there are bins with unacceptable error due to lack of drifter observations. To remove results with unacceptable error, a threshold (minimum number of drifter observations) is chosen below which the information within that bin is disregarded. A threshold of 40 6-hourly observations was chosen for this study. This reflects the assumption that a bin, which has less than 40 6-hourly drifter observations, corresponds to results with unacceptable error.

b. Mesoscale

In order to eliminate mesoscale features through averaging, the bin size must be sufficiently larger than mesoscale features. Using satellite imagery (Millot, 1991; Gacic et al., 1996; Mauri and Poulain, 2000), in-situ measurements (Gacic et al., 1999), and the magnitude of the first internal Rossby radius of deformation (Grilli and Pinardi, 1998), the size of mesoscale activity ranges from about 10 *km* to nearly 20 *km*

throughout the Mediterranean Sea. In order to sufficiently average out this mesoscale activity, it is imperative to select a bin scale larger than 20 *km*.

c. Sensitivity

The averaging scale selected ultimately affects velocity statistics. This effect is easily seen and evaluated by observing the average Mean Kinetic Energy, MKE, and Eddy Kinetic Energy, EKE (the term "eddy" here does not necessarily relate to mesoscale features but more correctly to any temporal and spatial variability encompassed by the bin) for bins of increasing size (and thus decreasing number for complete coverage of the region). The overlapping circular bin grid system was applied to Regions 1 through 5. The radius of the circular bin was varied to evaluate the effects of MKE and EKE on the bin size. The results for each region (using a threshold of 40 6-hourly observations) are shown in Figure 14. The "bumps" in the MKE and EKE averages are due to inconsistencies in area coverage as a result of the changing number and size of the bins used. For all the regions, significant sensitivity of MKE and EKE is seen for bin sizes less than about 100 *km*. Since resolutions larger than 100 *km* for Eulerian statistics are not of much use (geostrophic evaluations would be adequate for this scale), it must be noted that the choice of bin size significantly affects the energy levels derived from those bins. A bin size of 40 *km* was chosen for this study (with uniform spacing of bin centers at 20 *km*) as a compromise of the above-mentioned factors, and the following results of this paper are specific to this averaging scale.

d. Geographical Bin Spacing

Due to the large geographical coverage of the Mediterranean Sea, any statistical approach to divide it up into bins must consider curvature of the earth. Normally binning is simply defined by center points or edges on a uniform Latitude and Longitude grid. This approach, however, would result in vastly different geographical surface area for bins at uniform but different latitudes. In order to maintain a constant surface area contained within each bin, the radial spacing of the bins is calculated considering the curvature of the earth. This method assures that each bin is equally spaced from adjacent bins and that each bin contains the same surface area. Keeping the bin surface area uniform allows comparison of bin statistics under the same conditions. This method does, however, result in non-uniform latitude and longitude coordinates for the bin centers.

The first step in the process for choosing bin centers for this study is to determine the center in earth coordinates (longitude, latitude) for each region. The distance from this center to the edge of the bin in the meridional and zonal direction is calculated taking into consideration the curvature of the earth. These distances are used to determine the number of identical and equally spaced bins required to cover the entire region, and the appropriately sized grid is formed in normal Cartesian coordinates. The last step is to project the uniform grid from Cartesian coordinates to earth coordinates. This is done by calculating the distance and azimuth from the center bin to all other bins in the region defined in Cartesian coordinates. Since the center bin has been defined in

earth coordinates, the distance and azimuth values are used to determine earth coordinates for all other bins.

The last issue in handling the curvature of the earth is how to best display information derived from the geoid in two dimensions. Because of its simplicity, familiarity, and general acceptance, Mercator projections are used to display the results of this study. Figure 15 shows the visual distortion of equally spaced bin centers projected into earth coordinates and displayed with a Mercator projection. Figure 16 displays the bin size, shape and orientation when displayed on a Mercator projection.

2. Eulerian Calculations

With the data separated into appropriate bins, Eulerian statistics can be calculated. Handling drifter velocities as magnitudes of zonal (u_1) and meridional (u_2) components, the following Eulerian statistics are defined:

$$\text{Mean flow: } \langle u_i \rangle, \quad (1)$$

where i takes on the values of 1 (zonal) and 2 (meridional), and $\langle \rangle$ denotes the average in a given bin,

$$\text{Mean Kinetic Energy: } \text{MKE} = \frac{1}{2} (\langle u_1 \rangle^2 + \langle u_2 \rangle^2), \quad (2)$$

$$\text{Eddy Kinetic Energy: } \text{EKE} = \frac{1}{2} \left(\langle u_1'^2 \rangle + \langle u_2'^2 \rangle \right), \quad (3)$$

where $u_i' = u_i - \langle u_i \rangle$ denote residual velocity components. The variance ellipses defined by the principal axes of variance are computed from the eigenvalues and eigenvectors of the velocity covariance matrix, $\langle u_i' u_j' \rangle$ (Emery and Thompson, 1998) where i and j take on the values of 1 (zonal) and 2 (meridional).

C. SEASONALITY

Evaluation of seasonality was first conducted on a four-month scale relating to winter, spring, summer, and fall. Due to poor statistical results (too few observations on a 40 km scale) and apparently little change of the surface flow between seasons, quantitative analysis was not performed on this scale. On a biannual scale, however, statistics became robust and fluctuations of mean flow between time periods became evident.

The first step to evaluate the flow on a biannual basis is to determine how to divide up the year into two equal seasons (denoted winter and summer). Since it is expected that the highest flow intensities and variances are present in the winter, a comparison of EKE and MKE for each possible continuous six month period was analyzed for each region (Figure 17). In Region 1, the maximum MKE occurs when averaged over a six month period starting in November while the EKE peaks for the period beginning in December. For Region 2, similar peaks occur in May and November

for MKE and EKE, respectively. MKE and EKE both peak in August for Region 3 and MKE and EKE peak in October and November, respectively, for Region 4. Since it is not reasonable to have different seasons for regions in the same geographical location, a single season definition must be chosen for all regions. Considering the relative magnitude of the peaks, slopes adjacent to the peaks, and to the average over the entire Mediterranean Sea (Figure 17), winter is defined as occurring from November to April, and summer is defined as occurring from May to October for this study.

D. WIND CORRECTION

Since five types (with several different drogue depths) of drifters were used in this study, it is expected that one group or groups may differ in their water following capabilities. Three methods were employed to evaluate and possibly correct for the wind slippage effects of the drifters.

1. Comparison Method

With almost 150 thousand 6-hourly drifter observations in the Mediterranean Sea, occasionally there existed instances where two drifters of different sub-types (drifters of the same type and drogue depth) existed in the same vicinity at relatively the same time. The first method used to evaluate the water following capabilities sought to take advantage of these occasions.

The object of this analysis is to find enough pairs of drifters of the desired type (each pair must contain different drifter sub-types, but each pair must contain the same two drifter sub-types). The spatial scale for these pairs must be one in which we do not

suspect flow or wind variation of any significant degree. Likewise, the temporal scale for the pair must be one in which no significant variation is expected for the winds and surface flow. The most limiting factor on the time and distance parameters was that they be large enough to include a statistically significant amount of pairs.

With distance scales less than 5 *km* and time scales less than 18 hours, significant pairs are present for certain sub-types of drifters. Selecting one sub-type of the two from a group of pairs as the more water following, the difference in velocity between the pair can be compared to the velocity of the wind. The time and location of the drifter chosen as less water following was used for obtaining wind data.

Navy Operational Regional Atmospheric Prediction System (NORAPS) nowcasts in 1995 were obtained for the entire Mediterranean Sea. These wind data were interpolated in space to the drifter's location at the time of the now cast (midnight). With wind at each drifter observation, the drifter's velocity was split into the along- and across-wind direction components.

A comparison was performed by linear regression (least-squares method) applied to the along- and across-wind components of the drifter pair difference with the wind velocity magnitude. Regardless of drifter sub-type, temporal scale, spatial scale, or number of observation (neglecting the obvious perfect regression of only two points), no significant correlations were found (maximum correlation coefficients, not squared, were of the order of .5).

2. Correlation Method

Another approach to evaluate the wind slippage of the drifters allows each drifter type with drogue depth (sub-type) to be compared to the wind. Then the comparisons themselves can be compared against one other (drifter of different sub-type). Using the NORAPS nowcasts in 1995 for the entire Mediterranean Sea, wind data were again interpolated in space to the drifter's location at the time of the now cast (midnight). Dividing drifter type into sub-types, the along- and across-wind drifter speeds were quantitatively compared by linear regression (least-squared fit) to the wind speed magnitude at the drifter observation. Almost no correlation was evident for any drifter sub-type (correlation coefficients, not squared, were mostly less than .01), although data was plentiful (tens of thousands of data points). Without any significant correlation between the drifter and wind velocities, comparison among drifter sub-type is meaningless.

3. Application of Correction Derived Outside this Study

Using large numbers of drifters in most of the world's oceans, Pazan (Personal Communication) derived a correlation between the along-wind velocity of undrogued surface drifters and the wind speed (no significant across-wind slip was found for any latitude):

$$u_c = u_{uc} - .0088 * u_{wind} \quad (4)$$

where u_c is the corrected along-wind drifter speed, u_{uc} is the uncorrected along-wind drifter speed, and u_{wind} is wind speed. Using the same NORAPS nowcasts for 1995 as used in the comparison and correlation methods, (4) was applied to CODE drifters (only the 6-hourly CODE drifter observations in 1995). Since a vast majority of the 1995 CODE drifters existed in Adriatic Sea, Region 3 is the area used to evaluate the effectiveness of (4).

The correction to individual driver velocities (with a mean of 6.4 cm/s see Figure 18) is greater than the instrument/slippage error associated with CODE derived velocities (about 3 cm/s). However, after averaging all the corrected velocities within a bin, the correction to the mean velocities (with a mean of 1.9 cm/s see Figure 19) is less than the instrument/slippage error. Average EKE per bin as well as EKE averaged over all bins increased while MKE values stayed relatively the same. EKE is expected to decrease if wind slippage is removed (since wind effects do not necessarily correlate with the mean flow). Possible causes of increasing EKE could be related to the type and resolution of wind data or local influences not accounted for in the correction. When the final Eulerian mean flow is presented for the corrected and uncorrected cases (Figure 20), it is apparent that the corrected field is not better or more realistic compared to the uncorrected results. For the reasons above, the correction is not applied to any statistics presented in the results of this study.

E. ARRAY BIAS

Estimating Eulerian mean velocities using non-uniform Lagrangian data arrays include an “array” bias (Davis 1991). If bin size is small compared to the scales of variability for drifter concentration, mean flow, and diffusivity, the array bias can be expressed as:

$$\text{Array Bias: } A_i = -K_{ij}^E \frac{\partial_j C}{C}, \quad (5)$$

where K_{ij}^E is the asymptotic value of the lag-dependent diffusivity $K_{ij}(\tau)$ (see definition in Section F below) such that $K_{ij}^E = \lim_{\tau \rightarrow \infty} K_{ij}(\tau)$, and C is the drifter data concentration. K_{ij}^E was determined as the maximum value of $K_{ij}(\tau)$ over the range of τ from 0 to 20 days. Concentration was determined by the number of 6-hourly drifter observations divided by the area of the bin over water. With this array bias, the actual mean flow $\langle u \rangle_{cor}$ is related to the Eulerian mean flow estimate $\langle u_i \rangle$, through (Poulain, 2000):

$$\langle u \rangle_{cor} = \langle u_i \rangle + K_{ij}^E \frac{\partial_j C}{C}. \quad (6)$$

Finite central differences are computed using the four bins adjacent to the bin of interest to determine the gradient of concentration. For bins of interest that do not have the required adjacent bins (due to not meeting the threshold criterion or being over land), the gradient is not determined and the array bias for the bin of interest is not considered. Also, only the diagonal components of the diffusivity matrix are considered. The concentration of the bin of interest is used to scale the value obtained as the gradient. Diffusivity is estimated for each region in the meridional and zonal directions without considering variability of diffusivity within each region.

F. LAGRANGIAN STATISTICS

For Lagrangian statistics, computations are made on an ensemble of particles. In order to apply this type of statistics to drifters, the assumptions of stationarity and uniformity must be invoked. Assuming that the surface velocity statistics are stationary and uniform allows the computation of Lagrangian statistics for an ensemble of drifters arriving and leaving a finite size area independent of time. In this section, all drifter positions within the ensemble can be treated as deployment positions (respectively for each drifter). From each of these deployment positions, each drifter can be tracked as it arrived at the deployment position (negative time lags) and as it left the deployment position (positive time lag). Using the same notation as defined under Eulerian Statistics and defining $\langle \rangle_L(\tau)$ as the Lagrangian average (average over time and space) at time lag τ (time since deployment), the following statistics are used (Davis, 1991; Poulain, 2000):

Diffusivity: $\kappa_{ij}(\tau) = \langle u_i'(0)x_j'(\tau) \rangle_L(\tau)$ or

$$\kappa_{ij}(\tau) = \langle u_i(0) \rangle_L(0) * \langle x_j(-\tau) \rangle_L(-\tau) - \langle u_i(0)x_j(-\tau) \rangle_L(-\tau), \quad (7)$$

Lagrangian Velocity Covariance: $P_{ij}(\tau) = \langle u_i'(0)u_j'(\tau) \rangle_L(\tau)$ or

$$P_{ij}(\tau) = \langle u_i(0)u_j(\tau) \rangle_L(\tau) - \langle u_i(0) \rangle_L(0) * \langle u_j(\tau) \rangle_L(\tau), \quad (8)$$

where $x_i(\tau)$ is the i component displacement at time lag τ from an initial point $x_i(0) \equiv 0$, and $x_i'(\tau) = x_i(\tau) - \langle x_i(\tau) \rangle_L(\tau)$ and $u_i'(\tau) = u_i(\tau) - \langle u_i(\tau) \rangle_L(\tau)$ are the residual Lagrangian position and velocity components, respectively. Note that $\langle u_i(0) \rangle_L(0)$ is simply the Eulerian mean $\langle u_i \rangle$ over the geographical domain considered.

Lagrangian integral time and length scales are determined by scaling the diagonal elements of the diffusivity matrix with the Eulerian velocity variance and the Eulerian R.M.S. velocity, respectively (Poulain, 2000):

$$\text{Lagrangian Integral Time Scale: } T_{ij}(\tau) = \kappa_{ij}(\tau) / P_{ij}(0), \quad (9)$$

$$\text{Lagrangian Integral Length Scale: } L_{ij} = \kappa_{ij}(\tau) / \sqrt{P_{ij}(0)}. \quad (10)$$

When calculating Lagrangian statistics over a time lag of -20 to $+20$ days, drifters can travel substantial distances and the statistics become non-local. Asymptotic quantities of diffusivity, velocity covariance, length scale and time scale are affected. Corrected Lagrangian statistics are computed by using the Lagrangian statistics described above with the added step of removing the Eulerian mean flow from the individual drifter velocities. The Eulerian mean flow subtracted from each drifter's velocity is an interpolation of the Eulerian field using cubic splines at the drifter's location. This minimizes the effect of shear dispersion due to the Eulerian mean flow.

THIS PAGE INTENTIONALLY LEFT BLANK

V. RESULTS

A. EULERIAN

Eulerian statistical results for Regions 1 to 4 are presented in this section. To properly indicate the strengths and limitations of these statistics, a series of illustrations is provided on Mercator projections.

An illustration of the geographical locations of all 6-hourly data points is provided for each region. This illustration reveals areas of dense uniform coverage, areas of non uniform coverage, areas with little or no coverage, and areas where data may be available but provided by only a few independent drifters. The coast is shown as a geographical aid to the viewer.

Total 6-hourly drifter observations per bin are provided. In order to represent multiple overlapping bins, a square color-coded non-overlapping patch, which is centered over the bin's center, depicts the total of 6-hourly drifter observations. The color patch is not an indication of the bin size or shape, but merely the number of 6-hour observations contained within the bin. For bins with less than 40 6-hourly observations, no color patch is provided. The total of 6-hourly observations for each bin (regardless of threshold but not showing zeros) is indicated by a number displayed at the bin's center

MKE is presented as a color-coded graph that is similar to the graph provided for displaying the number of 6-hourly observations. A color-coded square patch indicating the MKE is provided at each bin's center. For bins that do not meet the threshold criterion, no color patch is provided. MKE values are posted for all bins that contain at

least one 6-hourly observation (without regard to threshold) at the bin's centers. A similar illustration is provided to show EKE values.

Eulerian mean velocities are displayed as arrows on a Mercator projection with the coast outlined. The direction and length of the arrow indicate direction and magnitude of the mean flow, respectively. The anchor point of each arrow is plotted at the center of mass of the 6-hourly observations in each bin (vice the bin's geographical center). No information is plotted for bins with less than 40 6-hourly observations.

Variance of flow is presented on a Mercator projection using an ellipse defined by the principal axes of velocity variance for each bin. The center of the ellipse is plotted at the center of mass for each bin. Again, no information is provided for bins with less than 40 6-hourly observations.

1. Region 1: The Alboran Sea/Algerian Current

Coverage of the region is adequate in the center of the region as well as along the southern coast (Figure 21). Bins meet the threshold criterion even when centered well on land within Algeria (Figure 22). Observations north of the Balearic Islands become sparse and are representative of only a few independent drifters. Bins begin to have fewer than 40 6-hourly observations for latitudes north of the Balearic Islands, and data along the coast of Spain and Sardinia is sparse. Figure 22 shows total 6-hourly observations peaking to well over three hundred in the western Alboran Sea and over 500 in the eastern Algerian Current. Another intensification of the number of observations exists as

flow converges through the Strait of Sicily with 6-hourly observations exceeding a thousand in a few bins.

MKE indicates strong flow (excess of $300 \text{ cm}^2/\text{s}^2$) in the Western Alboran Gyre (Figure 23). EKE is high (above $400 \text{ cm}^2/\text{s}^2$) throughout the Alboran Sea and is associated with the variability of the Alboran Gyres (Figure 24). Figure 25 displaying the Eulerian mean flow shows this gyre to be anticyclonic with typical velocities of 20-30 cm/s . MKE also indicates an intensification of the Algerian Current off the coast of Algeria near 1° E , 5° E , and 10° E (MKE in excess of $400 \text{ cm}^2/\text{s}^2$). MKE in the Algerian Current between these areas ranges from 100 to $200 \text{ cm}^2/\text{s}^2$ while values north of the Algerian Current rarely exceed $100 \text{ cm}^2/\text{s}^2$.

High EKE is focused close to the Algerian coast at the formation of the Algerian Current near 0° E . However, to the east, high EKE values exist in most of the Algerian basin. This is indicative of gyres being spun off from the Algerian Current and moving northeast over the Algerian basin (transferring energy from the Algerian Current across the Algerian basin). South of Sardinia, the EKE values decrease indicating less flow variability (MKE does not decrease in this area and may even slightly increase). Another slight and isolated increase in EKE is present near 10° E which does coincide with mean flow intensification indicated by MKE.

The Western Alboran Gyre and the Algerian Current are well defined in the mean flow diagram (Figure 25). A northward turning of the Algerian Current (separating from the coast) before it reaches Sardinia is well defined. The Algerian Current makes a

notable turn back southeast towards the coast at the southern tip of Sardinia. Then it once again re-intensifies east of Sardinia as it is bounded by the coast near 10° E (as is indicated by EKE and MKE). Flow magnitudes drastically decrease in the vicinity of the Sicily Strait with a stronger branch of the Algerian Current turning north along the coast of Sicily and not passing through the strait. This extension forms a noticeable cyclonic gyre between Sicily and Sardinia.

Variance is considerably larger in the direction of flow vice across the direction of flow within the Alboran Sea and along the Algerian Current (Figure 26), which are both, constrained by the coast and topography. Variance drops coincide with mean flow intensifications close to the Algerian coast near 1° E, 5° E, and 10° E. Variance also increases and becomes more isotropic west of the southern tip of Sardinia. This coincides with the northeast and subsequent southeast turns of mean flow. Once the southeastern turned flow intensifies off the coast of Tunis (and turns to follow the coast again), variance rapidly decreases and is once again oriented in the direction of flow.

Overall, the structure of Region 1 is unarguable characterized by the presence of the Western Alboran Gyre east of the Strait of Gibraltar and the relatively strong and focused Algerian Current along the Algerian coast. Almost all surface current descriptions of this region include these features. In addition to these features, the circulation over the Algerian basin is characterized by unstable nonstationary gyre circulation as previously described by Millot (1999). Although Ovchinnikov (1966) does not display this instability behavior, it is his geostrophic estimates of surface circulation

that do agree with the intensifications of the Algerian Current near 1° E, 5° E, and 10° E, with the northeastern and subsequent southeastern turn of the Algerian Current south of Sardinia, and with the cyclonic gyre that is evident between Sardinia and Sicily.

2. Region 2: The Ionian Sea

Coverage of the Ionian Sea is indicated by 6-hourly drifter positions (Figure 27). The number of observations in each bin (Figure 28) is remarkably uniform in space considering the significant amount and dispersion of the drifter deployments in this region. Bins only occasionally have less than 200 6-hourly observations. Higher concentrations (500 to 1000 6-hourly observations) are present in the northern Ionian Sea and on the east side of the Sicily Strait. Lack of sufficient data only exists in the very southern portion of the Gulf of Sirte. Few areas within the Ionian Sea fail to meet the 40 6-hourly observation threshold criterion.

MKE is relatively small throughout the Ionian Sea (typically less than $100 \text{ cm}^2/\text{s}^2$) while the majority of EKE values are near $150 \text{ cm}^2/\text{s}^2$ (Figures 29 and 30). There are two significant areas of low MKE. The first is south of Sicily (MKE typically less than $15 \text{ cm}^2/\text{s}^2$), and the other is east of Sicily (MKE less than $30 \text{ cm}^2/\text{s}^2$). EKE does not fluctuate significantly in Region 2, but there are relative peaks in EKE that correspond to the intensification of Algerian Current flow near 10° E as seen in Region 1, amplification of flow velocities in the AIS between Malta and Sicily, and the strengthening of flow near the African coast east of 22° E. MKE and EKE also show a slight increase of energies along the African coast near 14° E.

Surface current flow (Figure 31) indicates the AIS flows southeast through the Strait of Sicily (near 13° E) then branches into two major components. The branching of the AIS occurs south of Sicily where velocity variances exceed $500 \text{ cm}^2 / \text{s}^2$ (Figure 32). Here the AIS continues to flow southeastward away from Sicily and northeast towards Sicily. Low MKE characterizes the area between these two branches. The southern component of the AIS turns further south and continues until it is constrained by the African coast. Northeast of Malta, the northern component of the AIS turns east and flows eastward between Malta and Sicily. Ovchinnikov (1966), Robinson and Golnaraghi (1993), and Malanotte-Rizzoli et al. (1997) depict the AIS as flowing eastward south of Malta. As the northern branch of the AIS passes Sicily, it forms two extensions. The southern AIS extension continues in an eastward direction across the Ionian basin and the northern AIS extension turns north along the Italian coast (this northward turning is marked by high EKE values). Only this northward extension of the AIS is described in Robinson and Golnaraghi (1993), and Malanotte-Rizzoli et al. (1997). Ovchinnikov (1966) depicts only the southern extension of the AIS.

The northern extension of the AIS turns east then south as it is constrained by Italy, Strait of Otranto, and Greece forming the North Ionian Gyre and the southward flowing MIJ. The anticyclonic circulation of the northern extension of the AIS and the MIJ form the North Ionian Gyre. Robinson and Golnaraghi (1993) and Malanotte-Rizzoli et al (1997) describe the North Ionian Gyre as anticyclonic, whereas, Ovchinnikov (1966) describes it as cyclonic. The low MKE east of Sicily marks the center of this gyre.

The southward flow of the MIJ splits near 36° N with flow continuing south and flow veering east around a prevalent anticyclonic gyre. This anticyclone coincides with the Pelops gyre mentioned in Robinson and Golnaraghi (1993), and Malanotte-Rizzoli et al. (1997). The eastern current then turns south, east of the Pelops gyre and passes along the western edge of a cyclonic gyre southwest of Crete before joining the MMJ. This path is marked by EKE values in excess of $300 \text{ cm}^2 / \text{s}^2$, and the velocity variance in this area between the two gyres exceeds $400 \text{ cm}^2 / \text{s}^2$. Robinson and Golnaraghi (1993) depict the eastern current (Figure 5), whereas Malanotte-Rizzoli et al. (1997) indicate a central MIJ (Figure 4). The MIJ joins the southern extension of the AIS near 19° E, 34° N where both continue southward. Constrained by the African coast, the combined flows split to provide flow eastward into the Levantine Sea and southwestern flow along the African coast (no notable flow follows the coast into the Gulf of Sirte). Velocity variance in the area of the flow separation exceeds $400 \text{ cm}^2 / \text{s}^2$. The eastward flow forms the MMJ. Only Ovchinnikov (1966) describes the eastward flow into the Levantine basin and the southward flow back into the Ionian Sea (although the flow back into the Ionian Sea is depicted as traveling along the coast through the Gulf of Sirte).

3. Region 3: The Adriatic Sea/Tyrrhenian Sea

The characteristics of the Adriatic Sea derived from these data have been presented by Poulain (2000). Figures 33 through 38 are presented to validate the methods used in this study and to present characteristics of the Tyrrhenian Sea. The results for the Adriatic Sea are comparable to Poulain (2000)'s.

North of Sicily, drifter data become sparse. Although the center of the sea is represented to a fair degree, the coastal areas are representative of only a few independent drifters. Tyrrhenian Sea surface flow is not well defined due to lack of data and/or large variations of flow. The only noticeable stable flow characteristics are the northeastward north of Sicily (strong $200\text{--}300 \text{ cm}^2/\text{s}^2$ rather isotropic variance), the general northward flow over the entire basin with an intensification along the Italian coast near 41.5° N (relatively low variance of $100\text{--}200 \text{ cm}^2/\text{s}^2$ with MKE tripling as compared to adjacent areas), and gyre structures in the south Tyrrhenian Sea. Although the extreme south Tyrrhenian Sea has relatively large values of MKE and EKE, the main portion of the basin is characterized by low energy (MKE and EKE generally less than $50 \text{ cm}^2/\text{s}^2$ and $150 \text{ cm}^2/\text{s}^2$, respectively). Despite low energy signatures, a large cyclonic sub-basin gyre is evident in the southeastern Tyrrhenian Sea. West of this cyclone are indications of a much smaller anti-cyclone.

4. Region 4: The Levantine Sea

The Levantine Sea contains the lowest concentration of drifter observations as compared to the other regions (Figures 39 and 40) and lack of drifter data becomes a major source of uncertainty. East of Crete, number of 6-hourly observations per bin is about 100. The only large concentration occurs just southeast of the eastern tip of Crete where bin observations peak to over 400. Data are scarce in the Aegean Sea, along most of the Levantine Sea coast, in the northern portion of the basin, and in the center of the region near 26° E .

MKE for the region is generally less than $150 \text{ cm}^2/\text{s}^2$ with notable areas of minimum MKE in the center of the Levantine Sea at approximately 29° E and 33° E . A local minimum also occurs just south of the center of Crete. EKE minimums occur near the MKE minimums at 33° E and south of the center of Crete (Figure 42) indicating both minimum flow and minimum variance. However, the MKE minimum at approximately 29° E corresponds to high EKE values of about $300 \text{ cm}^2/\text{s}^2$ indicating large variability of flow (and possible flow reversals). MKE and EKE local peaks occur southeast of the eastern end of Crete indicating strong flow with large variability.

Surface flow of the Levantine Sea is outlined in Figure 43. Eastward flow is evident throughout the area between Crete and the African coast, but the MMJ is concentrated near the center of the Levantine Sea. No westward flow is evident in this area, which contradicts the flow described by Ovchinnikov (1966). The path of the MMJ is not well determined as it passes south of Crete (drifter observations becoming sparse in this area may be a contributing factor). However a well-defined anticyclonic gyre is present southeast of the eastern tip of Crete. Velocities in excess of 40 cm/s are present within this 150-200 km gyre. MKE is about $300 \text{ cm}^2/\text{s}^2$ in this area while EKE is typically $400\text{-}500 \text{ cm}^2/\text{s}^2$. This gyre corresponds to the Ierapetra gyre noted in Larnicol et al. (1995), and Matteoda and Glenn (1996). Variance along the edge of this gyre is nearly $500 \text{ cm}^2/\text{s}^2$ and increases to over $1000 \text{ cm}^2/\text{s}^2$ in the center of the gyre (Figure 44). East of this gyre, the MMJ becomes evident flowing to the east. This location

corresponds to Robinson and Golnaraghi (1993) but is significantly north of the flow described by Ovchinnikov (1966).

Flow along the eastern basin of the Levantine is decidedly north, exceeding 30 *cm/s*. This contradicts Robinson and Golnaraghi (1993)'s notion of the MMJ turning south at the eastern edge of the basin but coincides with Ovchinnikov (1966)'s results of northward geostrophic flow along the entire eastern Levantine basin.

Possibly due to the non-stationarity of the circulation features, and in particular seasonal variability, and/or the lack of drifter observations, no other permanent gyre circulation as noted in Robinson and Golnaraghi (1993) can be positively confirmed by this study.

B. SEASONALITY

Even with comprehensive data of the size used in this study, temporal separation of data often results in scattered and low concentration of observations. This is particularly the case for Regions 1 and 4. The effect of seasonality in these two regions cannot be adequately assessed due to poor geographical distribution of the drifter data. When temporally separated into two extended 6-month long seasons, the data distribution is adequate to estimate Eulerian statistics in the Ionian Sea (Figures 45 and 46).

1. Region 2: The Ionian Sea

Figures 47 and 48 indicate 6-hourly observations per bin are rarely less than a hundred when divided temporally into winter and summer. Average observations per bin are about 200 for the summer which containing slightly more data than the winter.

For summer, eastward flow of the AIS is stronger and less variable than in winter (Figures 49-52). The path of the summer AIS also has more significant southward meanders at 13° E and 15° E than are seen in the winter. Large eastward velocities exist north of Malta in the summer while westward flow is prevalent between Malta and the African coast (the threshold criterion is not met in the summer for a portion of the area south of Malta). In winter however, significant eastward flow exists south of Malta.

Another significant effect of the seasonality is the intensification of the MIJ in the summer. Southern velocities of the MIJ reach 30 cm/s in the summer but rarely reach 20 cm/s in the winter. Although the summer flow magnitudes are much stronger, the flow variance is relatively small (less than $100 \text{ cm}^2/\text{s}^2$) and less than winter flow variance (Figures 51 and 52). MKE of the southern flow of the MIJ exceeds $300 \text{ cm}^2/\text{s}^2$ in the summer vice less than $50 \text{ cm}^2/\text{s}^2$ in the winter. Although greater values of mean flow are present in the summer, EKE is higher, in general, for the winter than the summer.

The last area of notable seasonality is north of the African coast between 22° E and 23° E. Here, the winter MMJ has strong $20\text{-}30 \text{ cm/s}$ mean flows with flow variance averaging nearly $500 \text{ cm}^2/\text{s}^2$. In summer, however, there is no significant eastward mean flow, and flow variances are generally less than half the winter values.

2. Region 3: The Adriatic Sea/Tyrrhenian Sea

Seasonal variation of the Adriatic with finer spatial (20 *km* radial bins vice 40 *km* used in this study) and temporal (four 3 month seasons vice two 6 month seasons used in this study) resolution is described by Poulain (2000).

C. ARRAY BIAS

1. Region 1: The Alboran Sea/Algerian Current

The Alboran Sea contains significant zonal diffusivity due to the presence of the Algerian Current. Applying this diffusivity to the entire Region 1 is not appropriate. In order to obtain applicable array bias, local diffusivities must be calculated and applied, which was not done in this study.

2. Region 2: The Ionian Sea

The array bias for this region indicates various zones of convergence and divergence corresponding to local minimums or maximums in drifter data concentration, respectively (Figures 28 and 53). Array bias values are typically small within this region, but locally at several points, bias exceeds 5 *cm/s*. The large values of array bias at some coastal boundaries may not be appropriate as they were calculated using diffusivity defined for the entire Ionian basin.

The corrected mean flow of the AIS, AIS extensions, MIJ, and MMJ is only slightly different than the uncorrected values (Figure 54). The areas of larger array bias, specifically along the southeastern and northwestern coastal boundaries, have less realistic corrected mean flow.

3. Region 3: The Adriatic Sea/Tyrrhenian Sea

The Tyrrhenian Sea is lacking data to determine the array bias accurately. It is also not appropriate to apply a diffusivity derived from combining two separate seas (Tyrrhenian sea and Adriatic sea) to each individually. For these reasons, array bias was not considered for Region 3. However, array bias as computed from the Eulerian statistics using radial bins with a 40 *km* radius do concur with array bias calculated on a smaller Eulerian scale for the Adriatic Sea by Poulain (2000).

4. Region 4: The Levantine Sea

Array bias in the Levantine Sea is drastically oriented in the zonal direction. The variations in the zonal flow of the basin result in large zonal diffusivities. Region 4 however contains the MIJ as it passes west of Crete. Applying a regionally defined (and zonal oriented) diffusivity to the array bias calculation is not appropriate over the entire region. Therefore, array bias was not analyzed for Region 4.

D. LAGRANGIAN

The Lagrangian statistics, diffusivity, velocity covariance, integral time scale, and integral space scale were computed. Both the uncorrected and corrected (Eulerian mean flow subtracted from each drifter's velocity) Lagrangian statistics are presented for each region. The corrected Lagrangian statistics show better results (better asymptotic approach to constant plateau values) than the uncorrected statistics for all four regions. The corrected Lagrangian diffusivity should decrease due to the partial removal of

dispersion related to the mean flow, while the zero time lag value of velocity covariance when the Eulerian mean is removed should approach the Eulerian EKE values.

A summary of all the corrected Lagrangian statistics for Regions 1 through 4 is presented in Table 2. The table entries represent the time independent values for the Lagrangian parameters. Values of diffusivity range from $1.7 \cdot 10^7 \text{ cm}^2 / \text{s}$ for the zonal direction in Region 3 (due to the low zonal variations of the geographically constrained Adriatic Sea) to $6.4 \cdot 10^7 \text{ cm}^2 / \text{s}$ in the zonal direction of Region 1 (due to the large zonal variations of the Algerian Current). Lagrangian integral time scales are 1 to 3 days, and the length scales range from 14 km (due to the low meridional values of diffusivity and the relatively large velocity variance in Region 4) to 38 km (due to the large zonal diffusivity in Region 1).

1. Region 1: The Alboran Sea/Algerian Current

Due to the presence of the mostly zonal Algerian Current, the zonal components of the uncorrected Lagrangian statistics are significantly larger than the meridional components (Figure 55). The relatively strong flow in the Algerian Current also results in the largest values (zonal components of variance, diffusivity, integral time and length scales) for all uncorrected Lagrangian statistics (Figures 55-58).

A large difference between the corrected and uncorrected Lagrangian statistics is evident due to removing the relative large amount of zonal shear caused by the Algerian Current. This results in a significant decrease in the corrected zonal Lagrangian statistics. The meridional components of the corrected Lagrangian statistics are nearly unaffected

reflecting the lack of meridional variance of the velocity field. Although corrected Lagrangian statistics are less affected by the zonal Algerian current, the variations of the current result in the highest zonal values for Lagrangian statistics of all regions (Table 2). The corrected Lagrangian statistics for Region 1 are comparable to the Lagrangian statistics for the Algerian Current calculated by Salas et al. (2000).

2. Region 2: The Ionian Sea

The Ionian Sea shows no significant predominance of Lagrangian statistics in the zonal or meridional directions (Figure 56). This is due to the isotropic characteristics of the flow fluctuations throughout the basin. Meridional components of this region's uncorrected Lagrangian statistics are slightly larger than the zonal components, and this difference is only slightly increased when the predominant zonal mean flow is removed for determining the corrected Lagrangian statistics.

3. Region 3: The Adriatic Sea/Tyrrhenian Sea

Due to the size (much longer than wide) and orientation (the basin is more meridional than zonal) of the Adriatic Sea, the Lagrangian statistics for the meridional components are noticeable larger than the zonal components (Figure 57). The presence of the Tyrrhenian Sea with its predominately south to north flow exaggerates this effect although only slightly due to the relatively small amount of data when compared to the Adriatic Sea. Corrected values of the Lagrangian statistics are significantly less than the uncorrected due to removing the shear from the well-defined sub-basin gyres. The

presence of the Tyrrhenian Sea should again not significantly affect the characteristics of the corrected Lagrangian statistics.

Due to the small and confined Adriatic Sea (not significantly affected by the relatively small amount of data in the Tyrrhenian Sea), the zonal corrected Lagrangian statistics are minimal for this region (Table 2). The corrected Lagrangian statistics summarized in Table 2 are of the same magnitude as the results of Poulain (1999; 2000).

4. Region 4: The Levantine Sea

The orientation and large zonal flow significantly predominates the Lagrangian statistics in the zonal direction (Figure 58). With the significantly zonal mean flow removed, the corrected Lagrangian statistics have larger zonal values (Table 2). This reflects the poor north south variation of the velocity field when compared to east west variation.

VI. DISCUSSION AND CONCLUSIONS

This study analyzes data from 521 satellite-tracked drifters deployed throughout the Mediterranean Sea from 1986 to 1999. Eulerian and Lagrangian statistics of the surface circulation are examined for most of the Mediterranean Sea. Seasonal variation and array bias for the Ionian Sea are also investigated.

In order to best represent flow throughout the Mediterranean Sea as a combination of a deterministic mean and fluctuations due to temporal and mesoscale variability, a Eulerian grid system composed of 20 *km* radius circular overlapping bins with 20 *km* spacing is used. The Eulerian statistics are presented as charts of Mean Kinetic Energy (MKE), Eddy Kinetic Energy (EKE), mean flow, and velocity variance.

Eulerian results reveal several major flow patterns throughout the Mediterranean Sea. The anticyclonic Western Alboran Gyre is prevalent in the Alboran Sea, whereas, the presence of the Eastern Alboran Gyre is uncertain. The Algerian Current is well sampled and shows intensifications of flow near 1° E, 5° E, and 10° E, a northward meander near 8° E, and a general dispersion of energy northeastward across the Algerian basin. The large zonal variations of the Algerian Current result in Lagrangian statistics that are predominately zonal even with the mean flow removed. These corrected Lagrangian statistics are less than the Lagrangian statistics presented by Salas et al. (1999), but are of the same magnitude.

The Tyrrhenian Sea is characterized by a general northward flow across the entire basin. Exceptions to this general flow are the eastward flow along the north coast of

Sicily and two gyres in the south Tyrrhenian Sea. The anticyclonic and cyclonic gyres are located near 12° E and 14° E, respectively. Lagrangian statistics for the combined Tyrrhenian and Adriatic Seas are significantly more representative of the Adriatic Sea due to the overwhelmingly greater number of observations in the Adriatic Sea as compared to the Tyrrhenian Sea.

Flow in Adriatic Sea is cyclonic on a global scale. There exist three large and well defined cyclonic gyres in the south, central, and north portions of the basin. The bathymetry of the basin significantly affects the sub-basin circulation with the central and southern gyres coinciding with the Jabuka and south Adriatic pits, respectively (Poulain, 2000). A less well defined and more isolated smaller cyclonic gyre is present in the extreme north portion of the basin. Eulerian and corrected Lagrangian statistics correlate well with the results of Poulain (2000).

The Ionian Sea has several distinct flow paths. The Atlantic Ionian Stream (AIS) enters the Ionian Sea about midway in the Sicily Strait. South of Sicily, the AIS branches into a southward component that flows to the coast of Africa, and a northeast component that flows between Sicily and Malta. In the summer, the AIS is stronger with less flow variance than in winter. Between Malta and the African coast, flow is westward in the summer vice eastward in the winter. East of Sicily, the northeast component of the AIS extends north forming the northern AIS extension and continues east forming the southern AIS extension. The northern AIS extension travels along the coastal barrier of the northern Ionian Sea forming the North Ionian Gyre and the Mid-Ionian Jet as it turns east then south along the coast of Greece. The MIJ has greater flow velocities with less

variance in the summer than in the winter. Flow branches from the MIJ near 36° N, travels around the anticyclonic Pelops gyre, turns south to pass west of the Cretan Cyclone, and joins the MMJ near 23° E. The main MIJ continues south and combines with the southern AIS extension. The combined flow continues southeastward until it is constrained by the African coast where it branches east to the MMJ in the winter (no notable flow from the MIJ branches east to the Levantine Sea in the summer) and southwest back into the Ionian basin. No reversal from anticyclonic to cyclonic of the North Ionian Gyre was noticed from the drifter measurements. This is an indication that the seasonal reversal related to seasonal variability of the wind forcing might be hampered by interannual variability.

When Eulerian mean flow is corrected for array bias in Region 2, slight improvements of the AIS, AIS extensions, MIJ, and MMJ result. The slight improvement of these main flow characteristics is insignificant compared to the unrealistic corrected mean flow prevalent in the southwest and northeast coastal areas of the Ionian Sea. The regionally derived values of diffusivity are not appropriate for these coastal regions.

West of Crete, the path of the MMJ is uncertain. In this area, the Ierapetra anticyclonic gyre is well sampled. The MMJ becomes evident east of the Ierapetra gyre and branches near 31° E to continue east and southeast. The MMJ continues to the edge of the basin where flow along the eastern coast of the Levantine Sea is distinctively northward.

Mediterranean Sea surface circulation as derived from our drifter data between 1986 and 1999 is qualitatively summarized in Figure 59. Although this new description of the mean pathways might contradict some of the references noted at some locations, it is the first description derived from direct flow measurements on a Mediterranean basin scale. Our description is not only qualitative, but because the study employed accurate Lagrangian velocity measurements, quantitative statistics are calculated to augment the qualitative summary.

VII. RECOMMENDATIONS FOR FUTURE WORK

Although the array bias and wind slippage errors were addressed in this thesis, further error analysis could be performed. A more extensive evaluation of Lagrangian sampling errors could be explored. Due to the presence of inherent wind slippage, further analysis is required to better assess the water-following capabilities of the drifters used.

The drifter data set used in this study includes Sea Surface Temperatures (SST). This SST information was not used or addressed in this study. Significant information could be learned about horizontal heat transports using the combined Lagrangian velocity and SST data.

With satellite altimetry charts available for the Mediterranean Sea, much can be learned from the comparison and melding of remote sensing data with the Lagrangian drifter data of this study.

Type	Drifter	Drogue Depth	Totals	Origin (w/numbers)
1	CODE	N/A	247	NAVOCEANO (6) NPS (119) SACLANTCEN (122)
2	CMOD	4 m 100 m	41 181	NAVOCEANO (222)
3	SVP/ TRISTAR	10 m 15 m 300 m	7 14 1	ENEA (7) ION (11) NPS (3) SACLANTCEN (1)
4	A111/A104	10 m	17	ICN (17)
5	Others	0 m 10m	6 6	CNRS (5) TELESPAZIO (7)

Table 1. Drifter types with origin.

Region		Variance cm^2 / s^2	Diffusivity $10^{-7} cm^2 / s$	Time Scale days	Length Scale km
Region 1- Alboran Sea/ Algerian Current	Zonal	275.3	6.4	2.7	38.4
	Meridional	224.5	2.2	1.2	14.8
Region 2- Ionian Sea	Zonal	151.1	2.8	2.1	22.8
	Meridional	168.7	3.2	2.2	25
Region 3- Adriatic Sea/ Tyrrhenian Sea	Zonal	94.2	1.7	2.0	17.1
	Meridional	122.1	2.3	2.2	21.1
Region 4- Levantine Sea	Zonal	223.8	4.4	2.3	29.1
	Meridional	183.3	1.9	1.2	14

Table 2. Corrected Lagrangian statistics (with the Eulerian mean flow removed): velocity variance, diffusivity, and Lagrangian time and length scales for Regions 1-4.

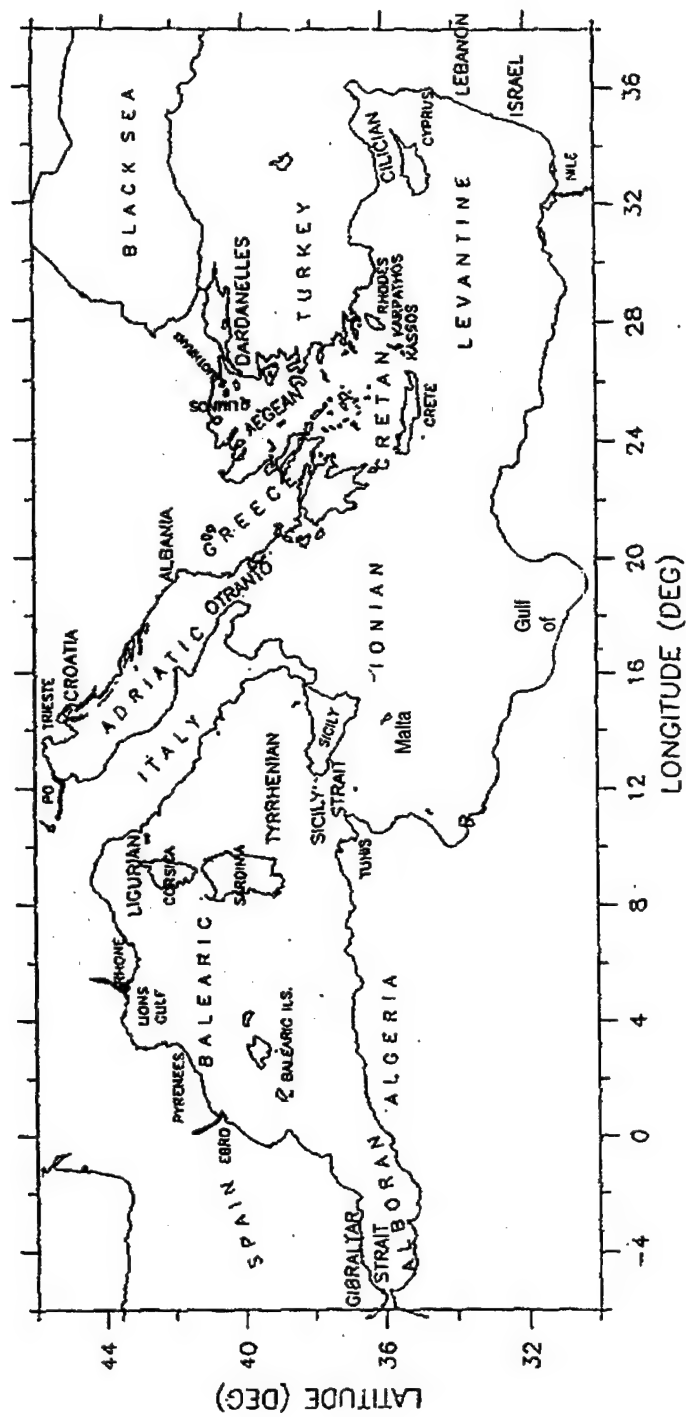


Figure 1. Mediterranean Sea with areas of interest labeled.

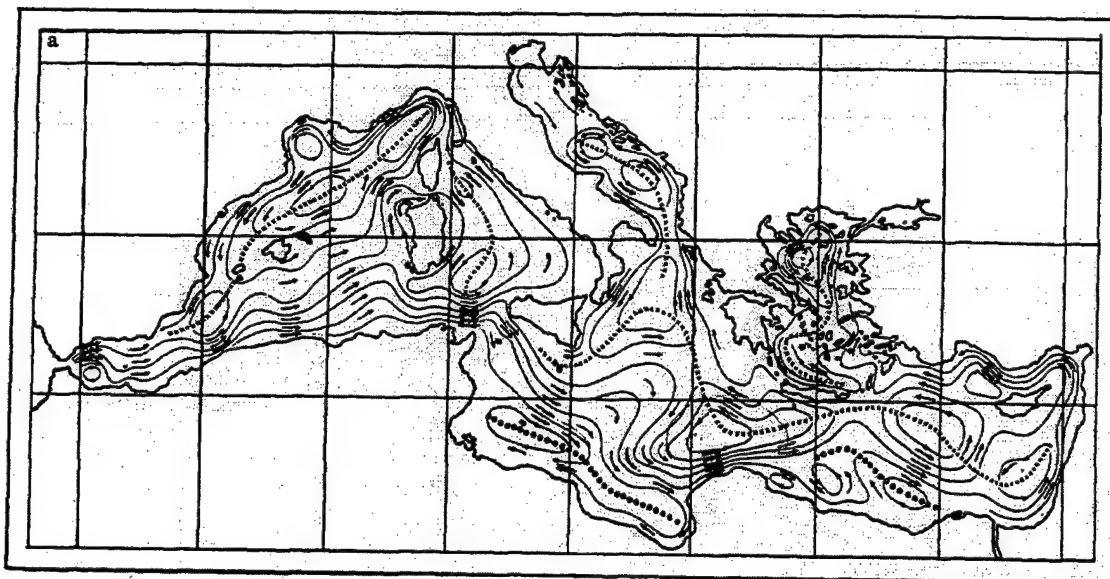


Figure 2. Mediterranean geostrophic surface currents derived from hydrographic data in winter (from Ovchinnikov, 1966).

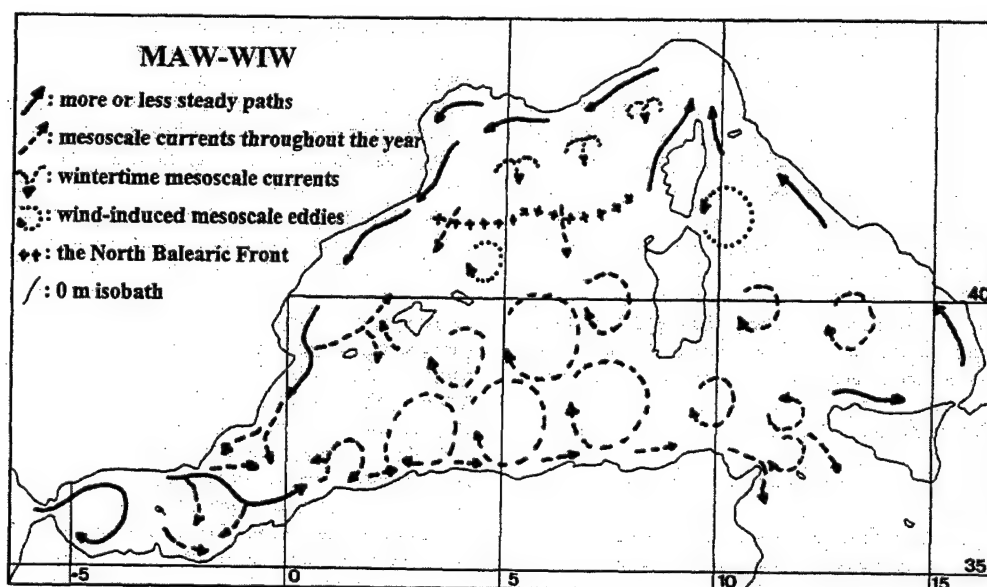


Figure 3. Circulation paths of the Modified Atlantic Water (MAW) and the Winter Intermediate Water (WIW) in the Western Mediterranean Basin (From Millot, 1999).

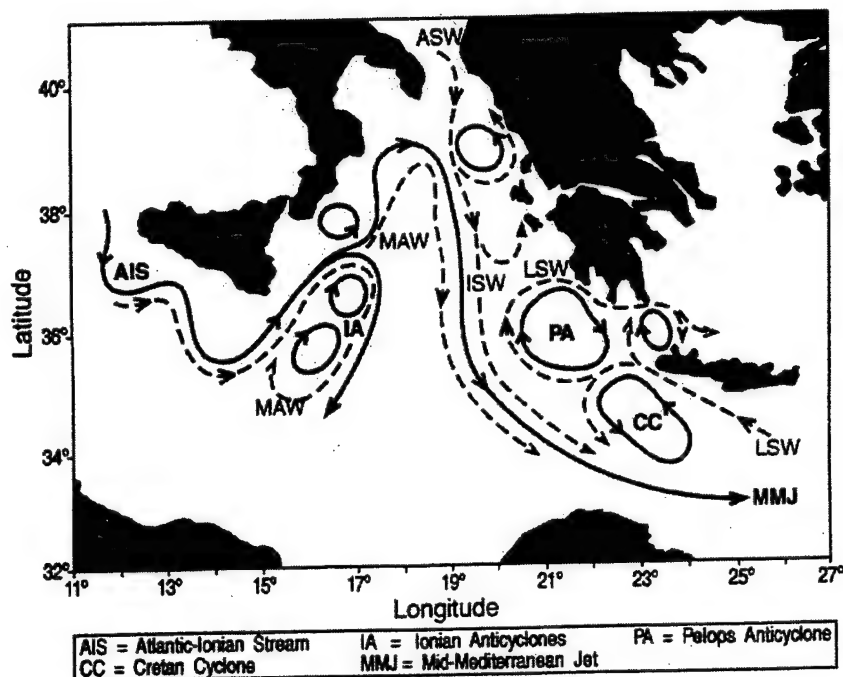


Figure 4. Ionian Sea upper thermocline circulation. Solid lines denote permanent dynamic features. Dashed lines mark water mass pathways (from Malanotte-Rizzoli et al., 1997).

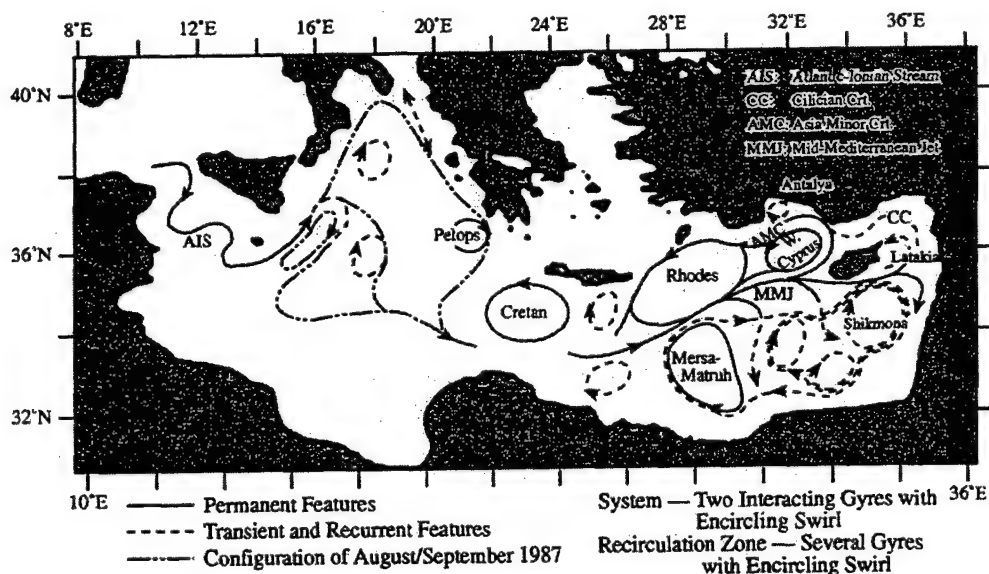


Figure 5. Upper thermocline general circulation obtained from melding of data and dynamics in the Eastern Mediterranean Basin (from Robinson and Golnaraghi, 1993).

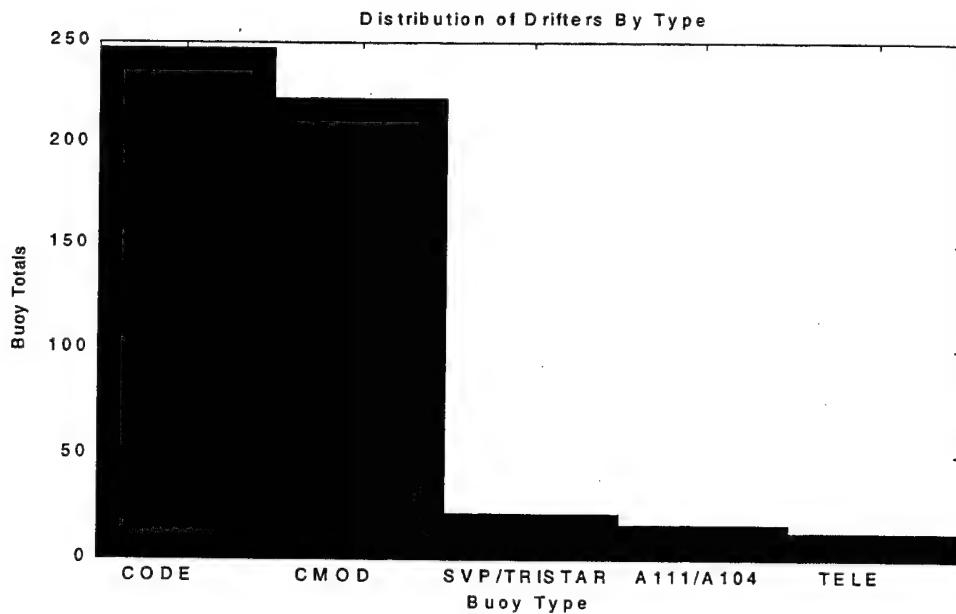


Figure 6. Distribution of the total number of drifters for the five drifter types (CODE, CMOD, SVP/TRISTAR, A111/A104, and Other-denoted TELE).

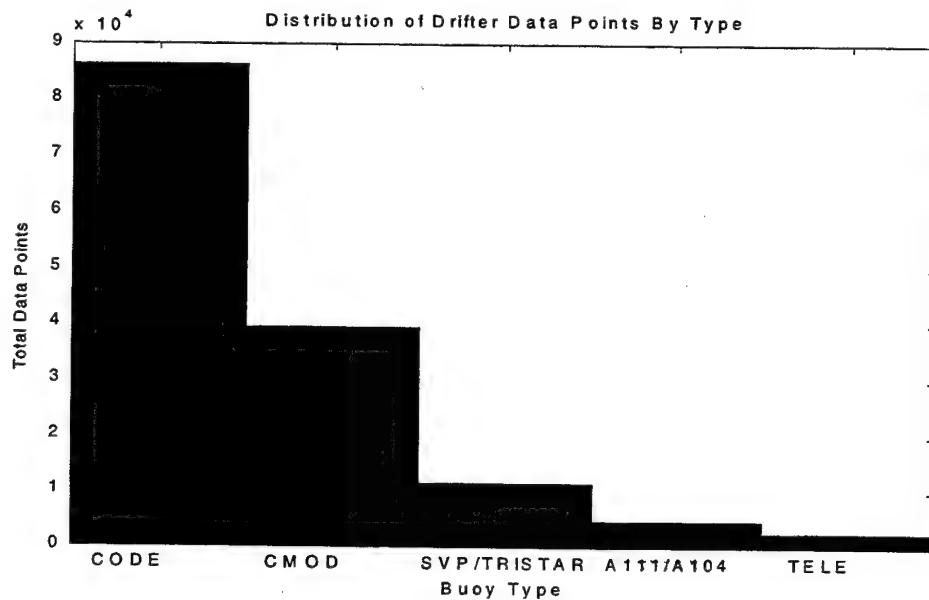


Figure 7. Distribution of the total number of the total 6-hourly drifter observation points for the five drifter types (CODE, CMOD, SVP/TRISTAR, A111/A104, and Other-denoted TELE).

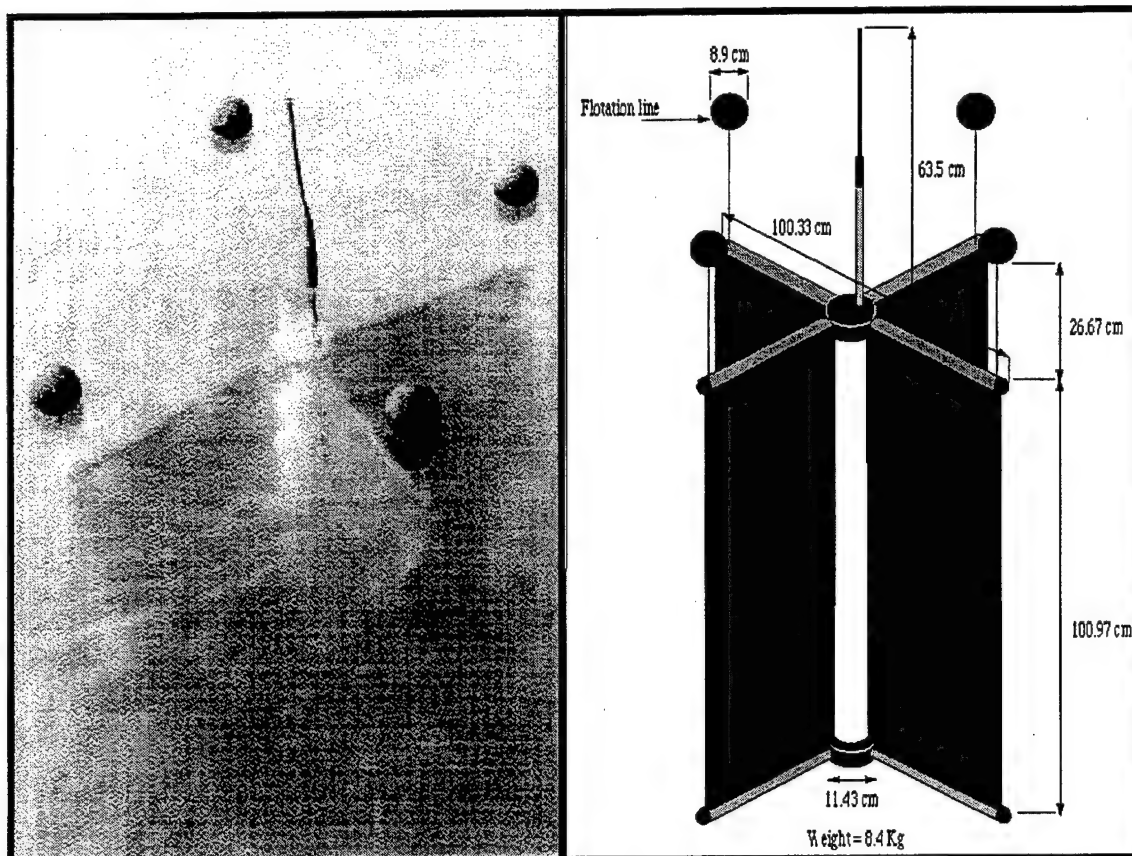


Figure 8. Photograph and schematic diagram of the modified CODE drifter (from Poulain et al., 2000a).

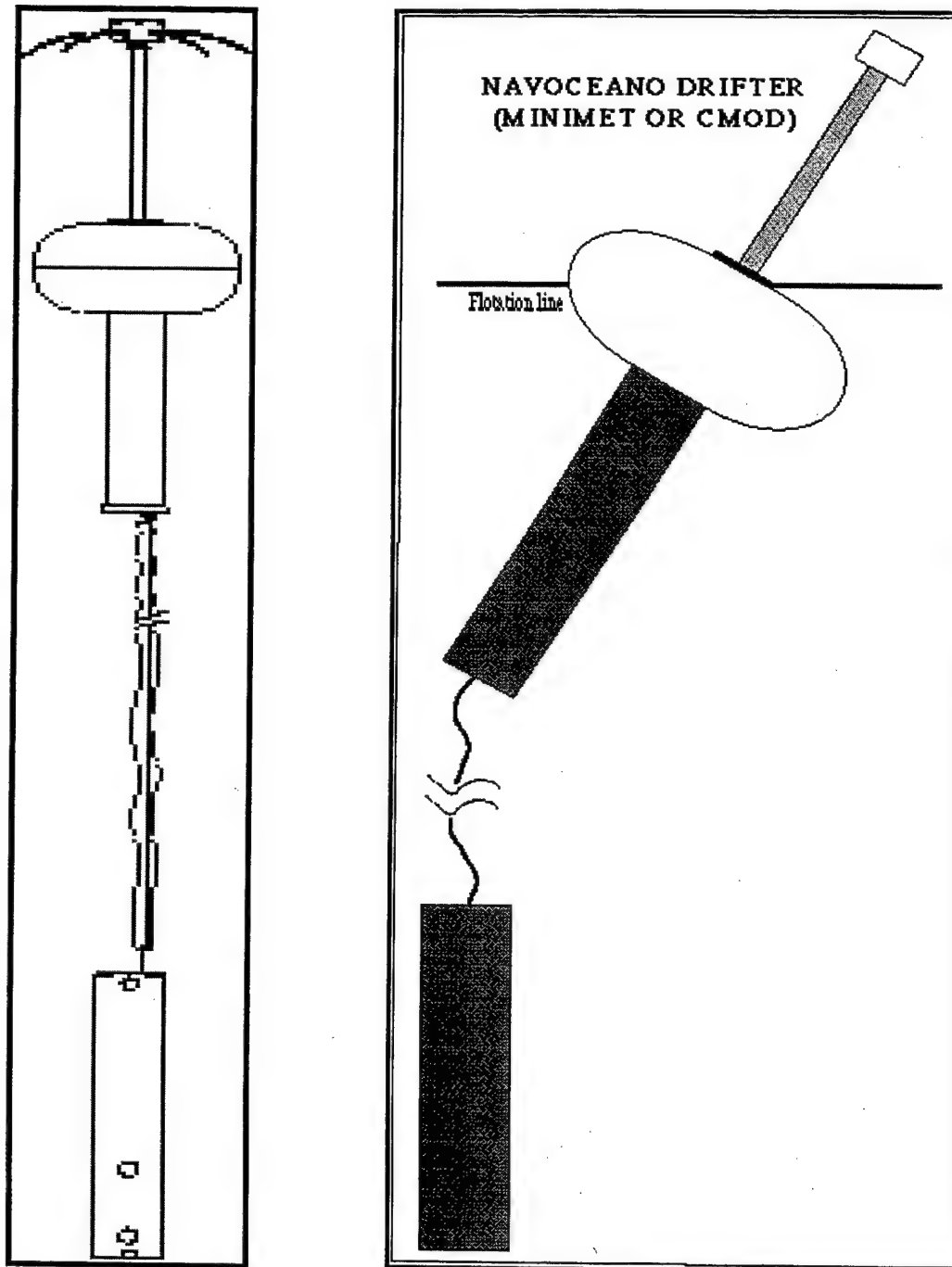


Figure 9. Schematics of the CMOD drifter components and floating characteristics (from Poulain et al., 2000a).

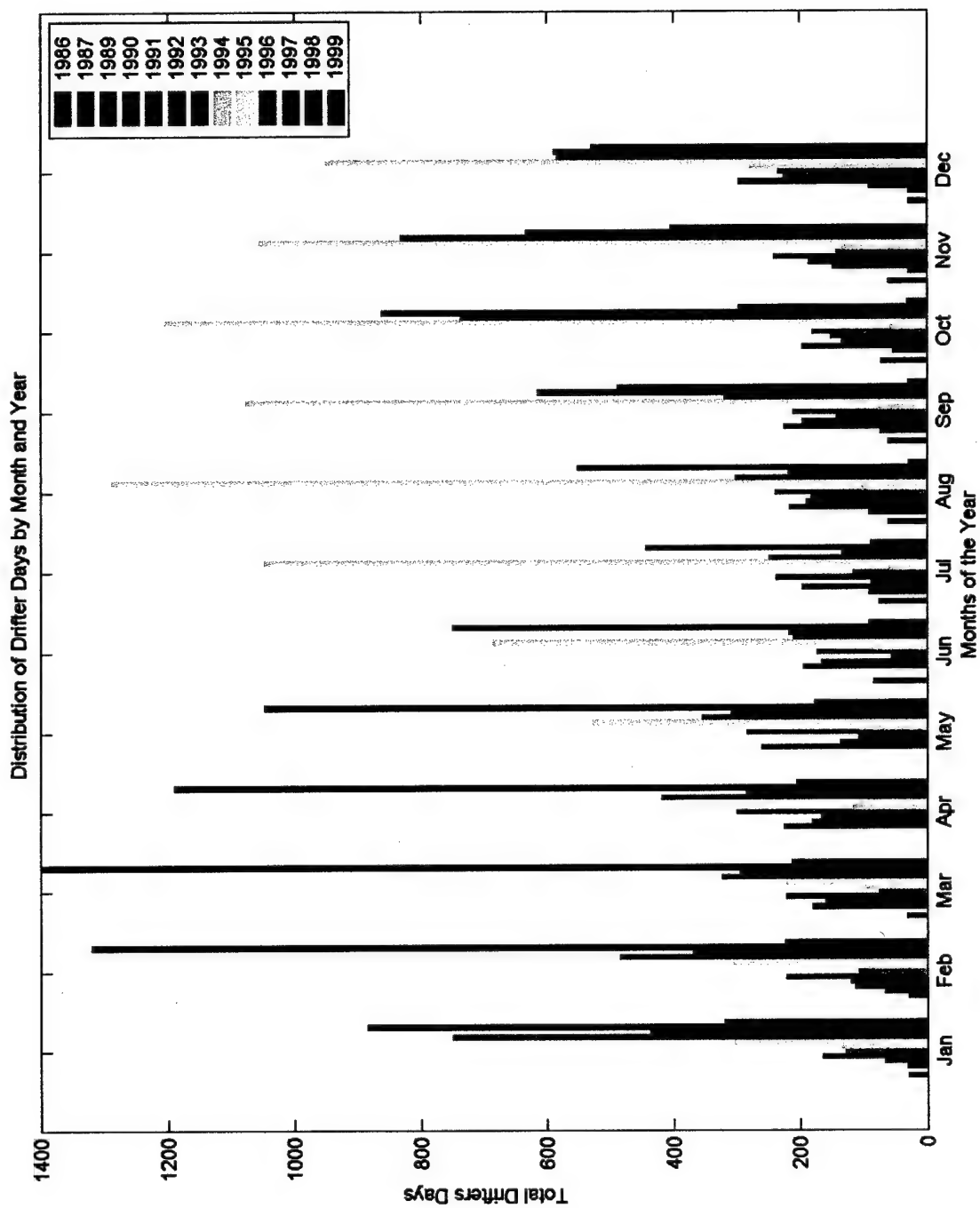


Figure 10. Drifter coverage by month and year. The number of drifter days (four 6-hourly observations) is plotted for each month of each year

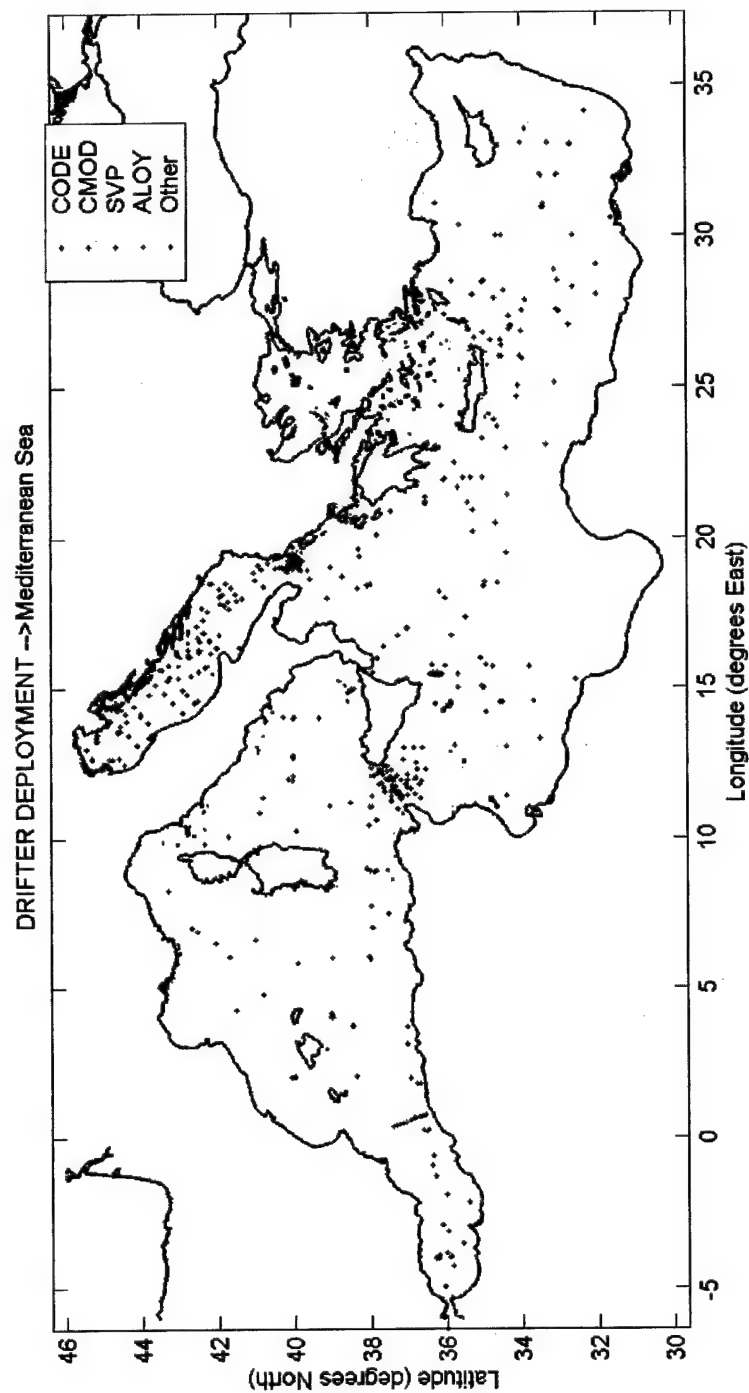


Figure 11. Drifter deployment positions. The dots are color-coded with respect to the drifter type.

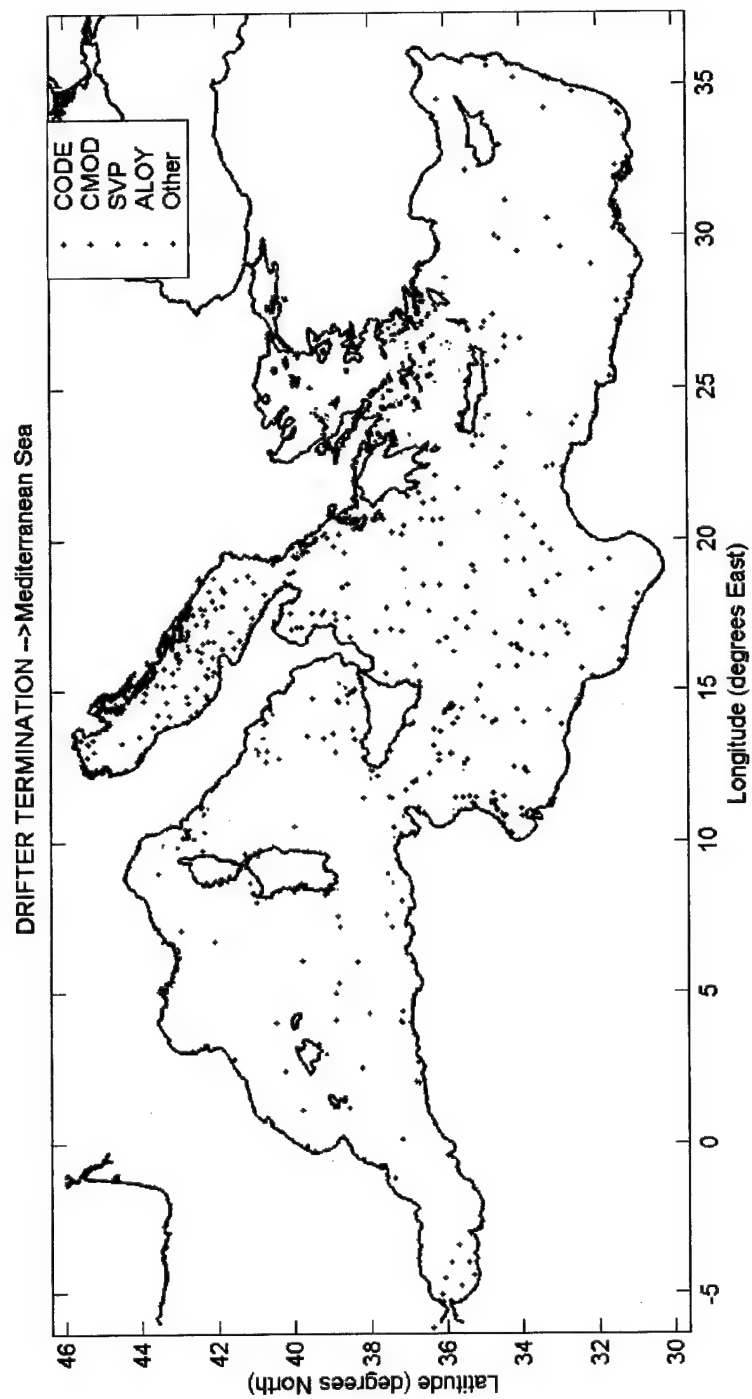


Figure 12. Drifter termination positions. The dots are color-coded with respect to the drifter type.

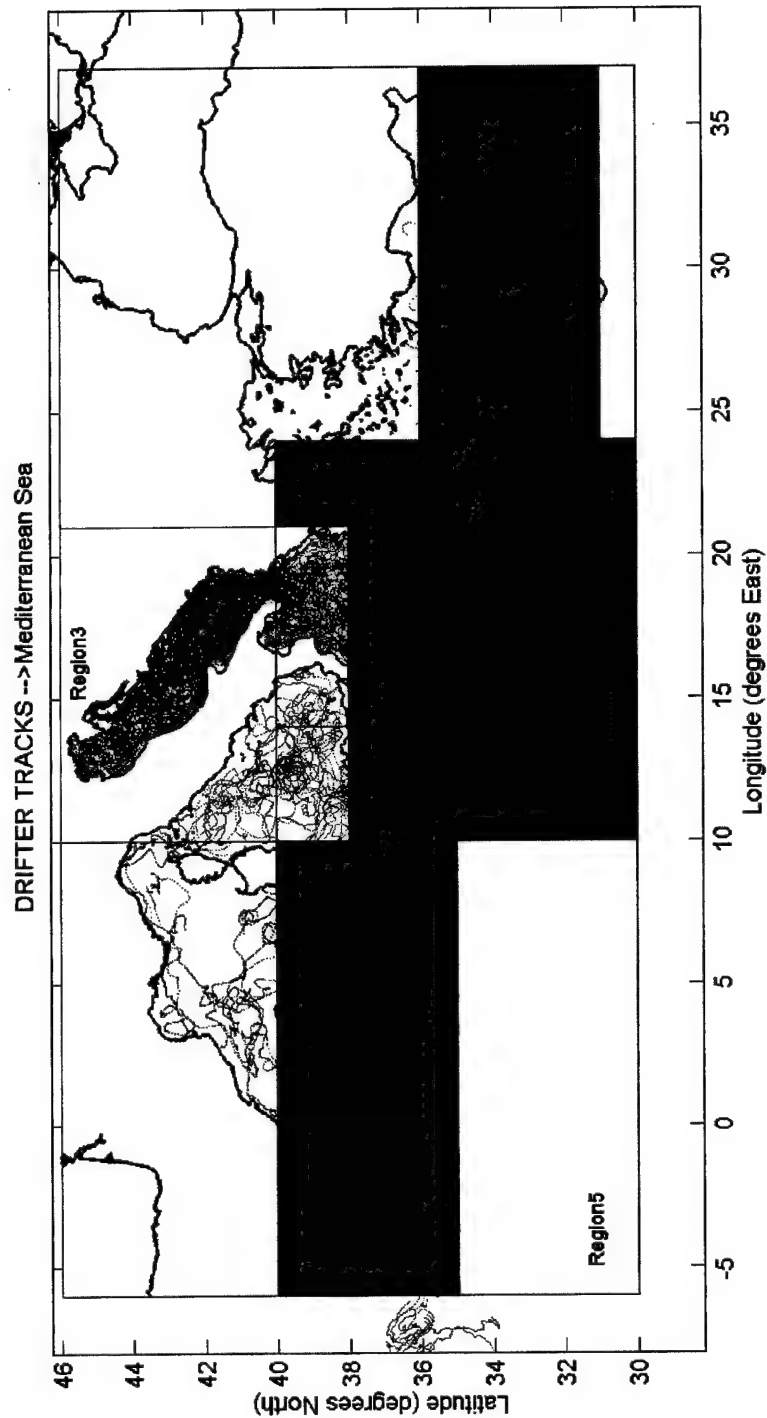


Figure 13. Regions of study. The regions overlap one another, but all regions are rectangular as defined by latitude and longitude lines. The positions of the 6-hourly observations are overlaid in red.

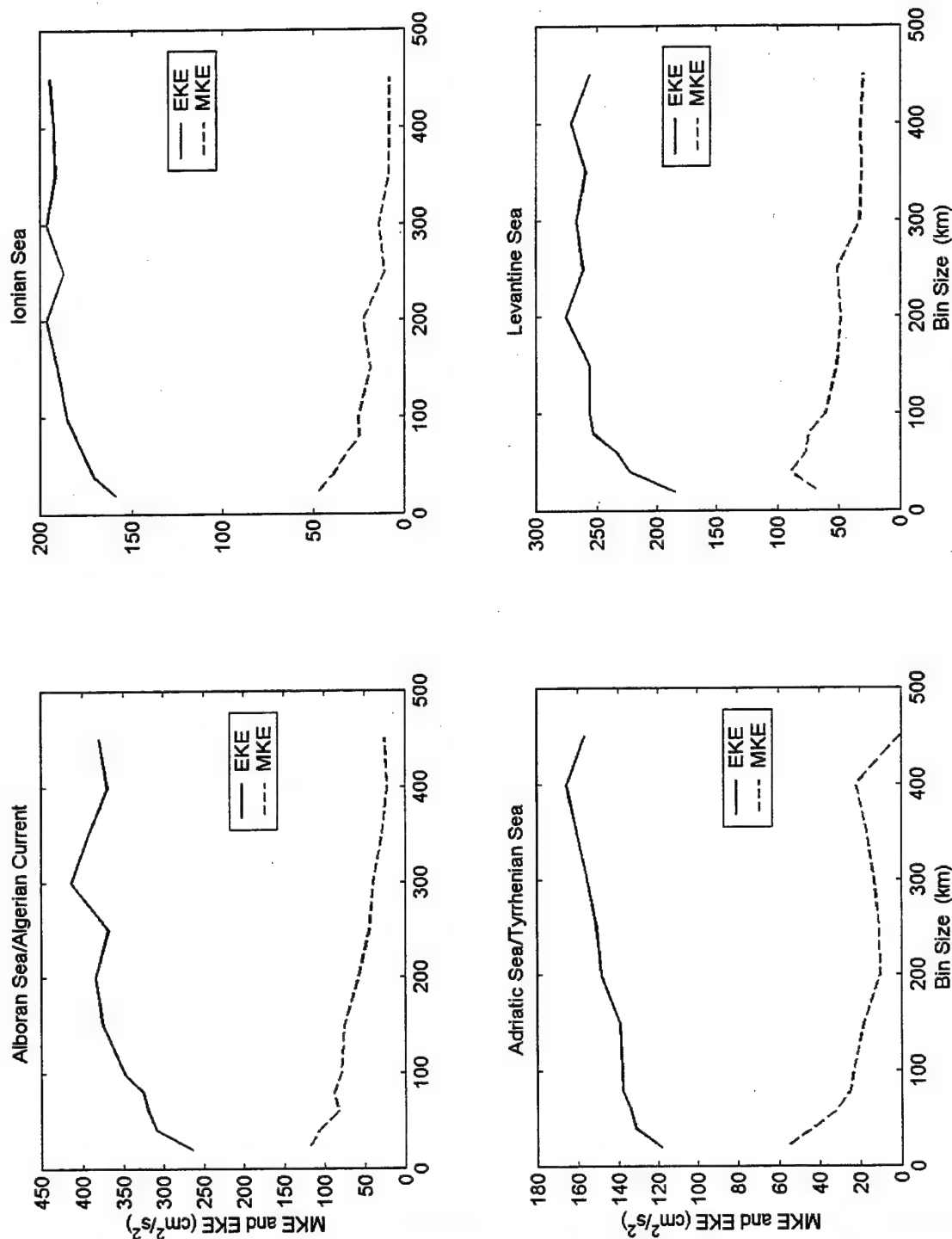


Figure 14. Sensitivity analysis for Regions 1-4. For each region, Eulerian statistics utilizing bins of varying sizes were computed. The average energies (MKE and EKE) of all the bins required to cover the region is displayed for each bin size (bin size refers to the radius of the circular bins).

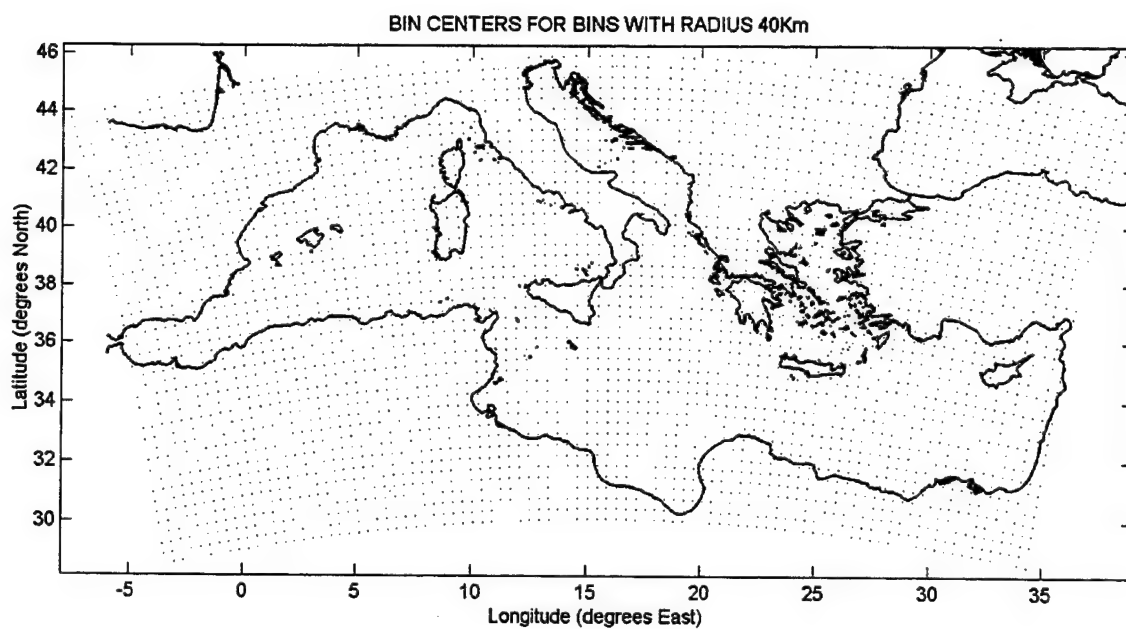


Figure 15. Bin centers. The locations of 40 km radius circular bin centers are denoted for uniform bin spacing between bin centers.

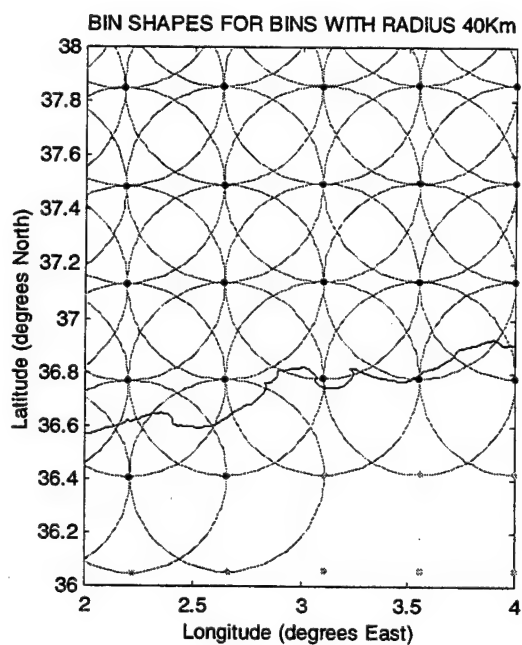


Figure 16. Bin shape and distribution. Schematic shows on a Mercator projection the locations and orientation of 40 km radius circular bins with 40 km between bin centers.

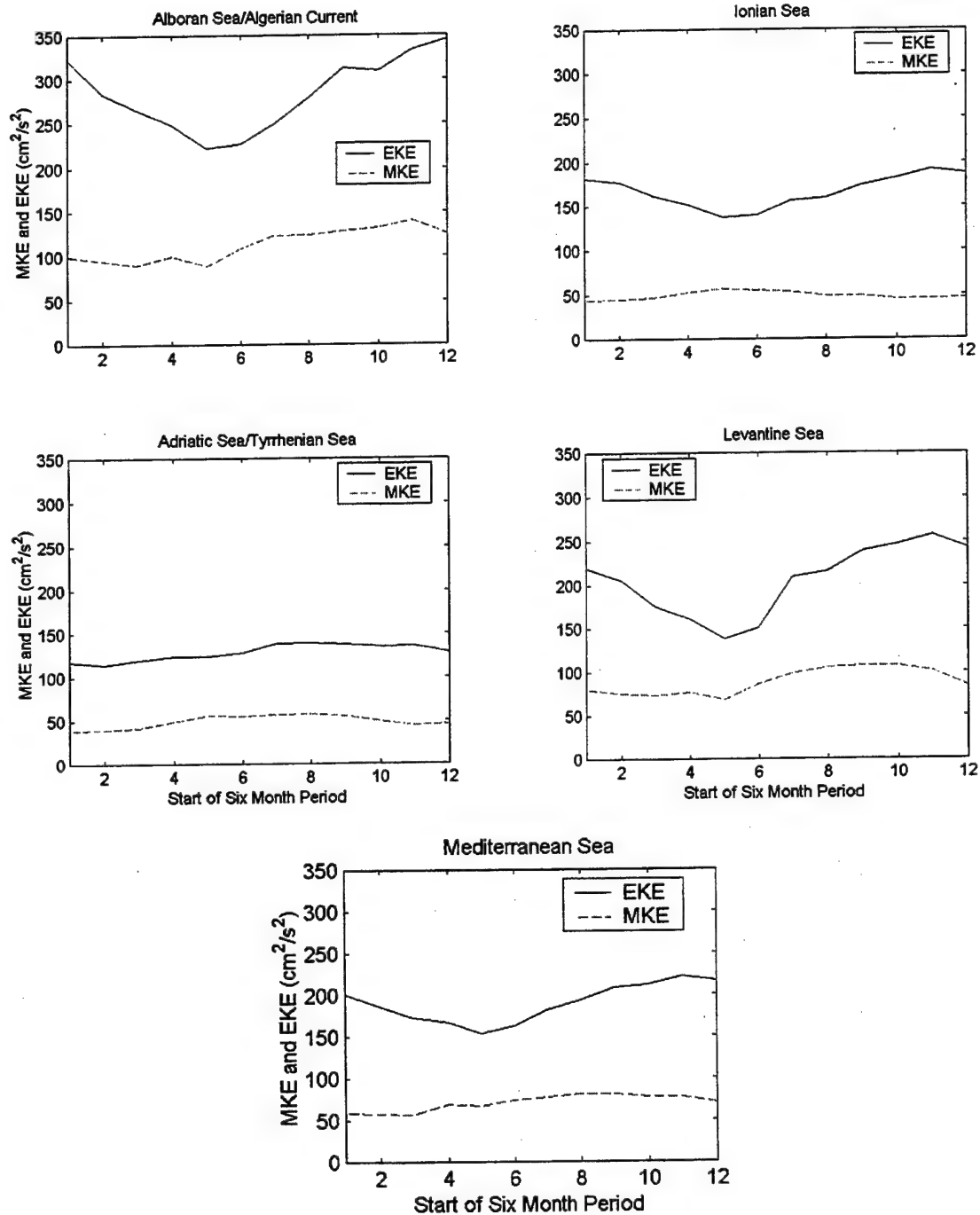


Figure 17. Seasonal analysis. For 40 km radius bins with 40 km spacing between bin centers, the EKE and MKE averaged over all bins is displayed for the six month period beginning with the month annotated. Results are shows for Regions 1 through 4.

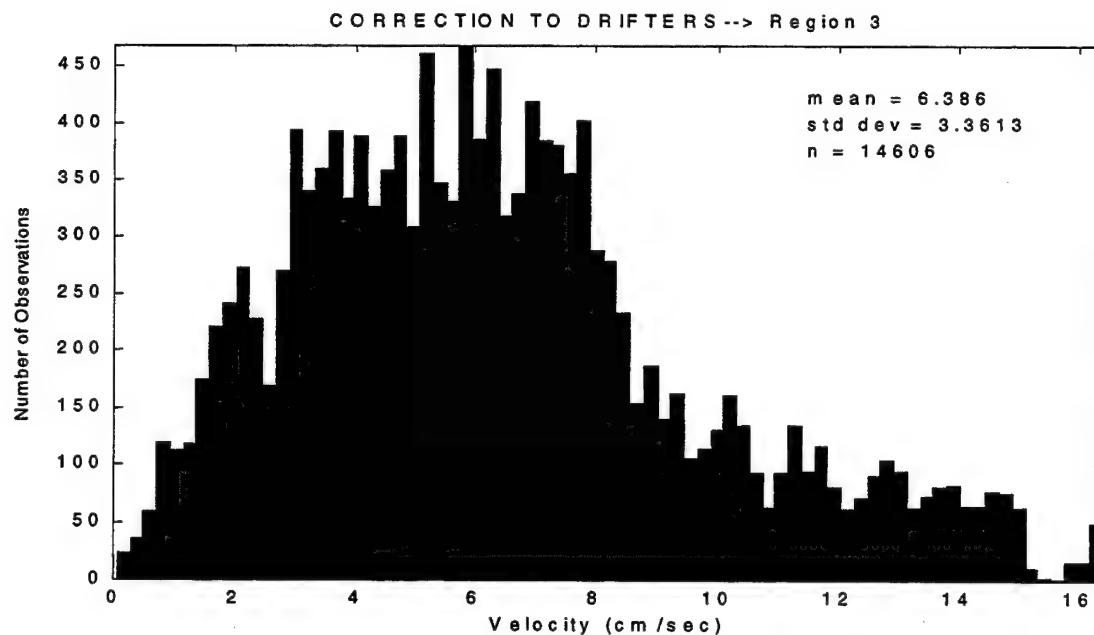


Figure 18. Distribution of the magnitude of wind slippage correction for individual CODE drifter velocities from 1995 in Region 3.

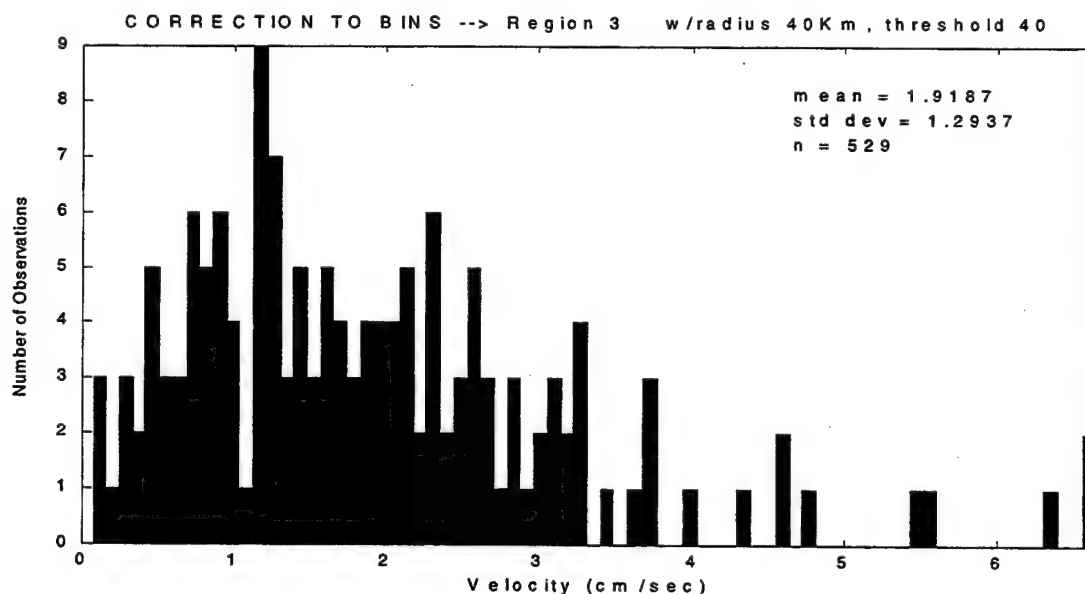


Figure 19. Distribution of the magnitude of the difference between bin average velocities for corrected and uncorrected drifter data (CODE drifters in 1995 for Region 3).

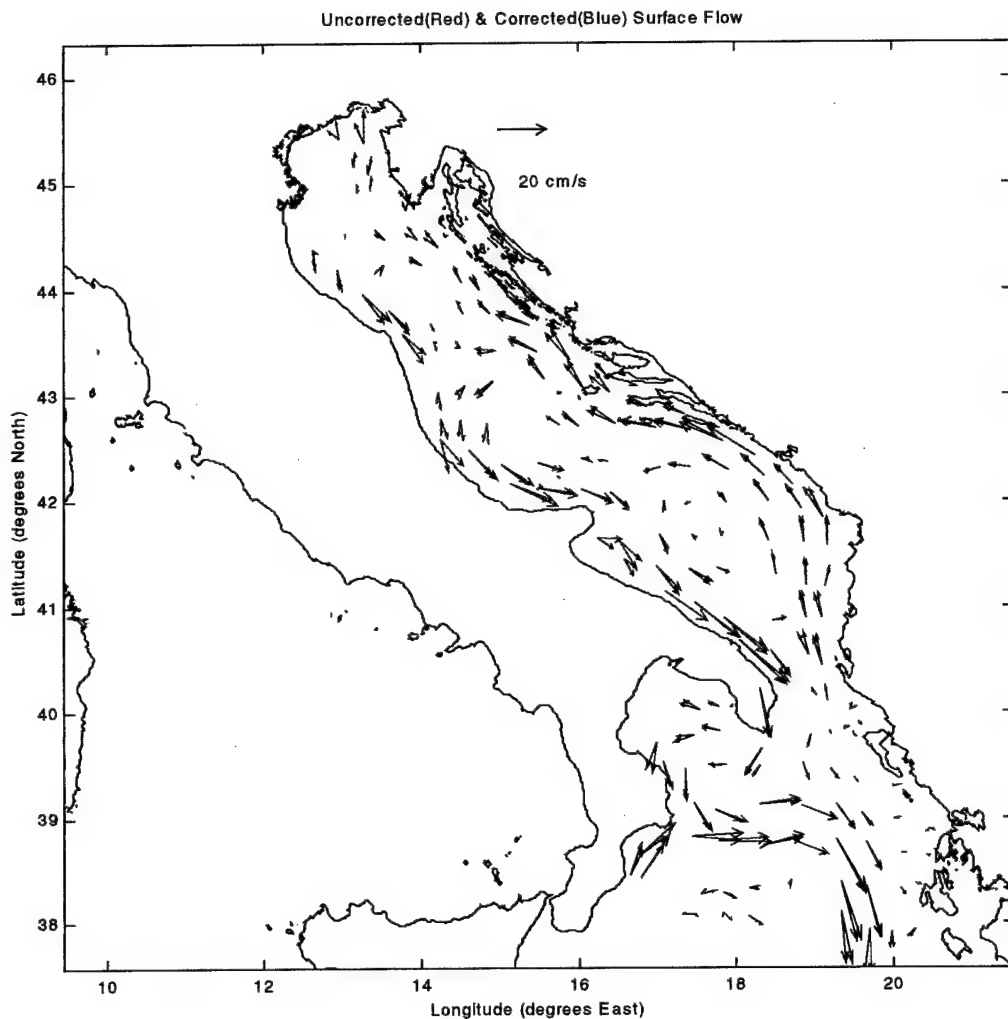


Figure 20. Correction of CODE drifter wind slippage. The blue (red) arrows indicate the uncorrected (corrected) bin averages of CODE drifter velocities from 1995 in Region 3 using 40 km radius circular bins whose centers are spaced at 40 km.

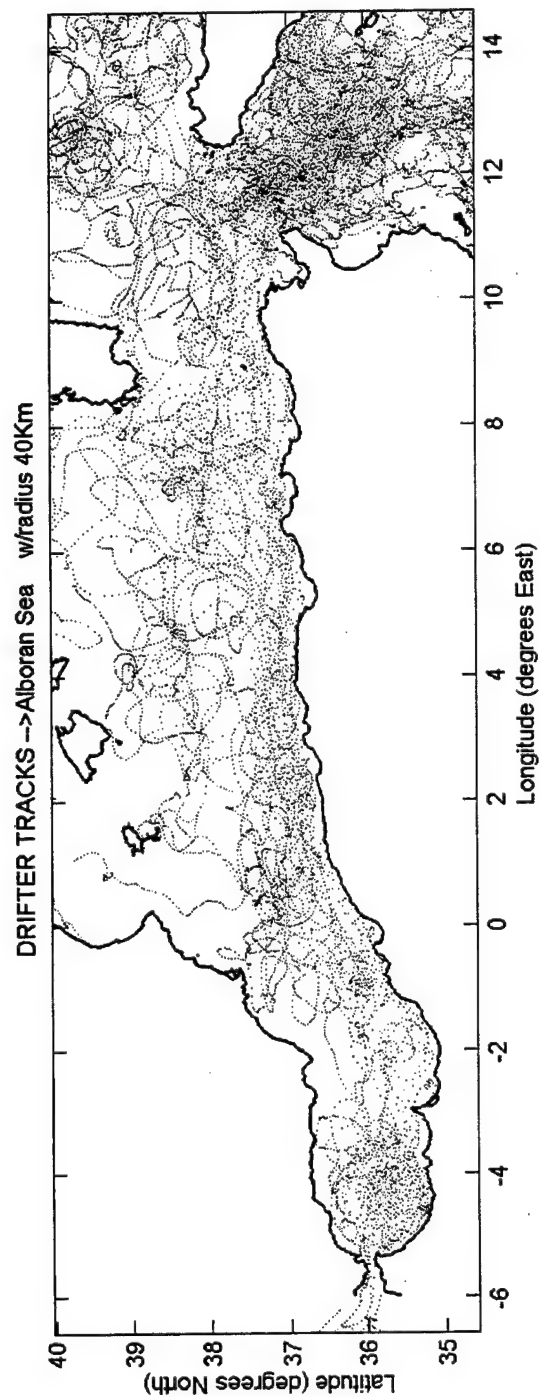


Figure 21. Region 1 drifter observations. Each 6-hourly drifter observation, which falls within any of the 40 km radius circular bins used to cover the entire area of the region, is plotted.

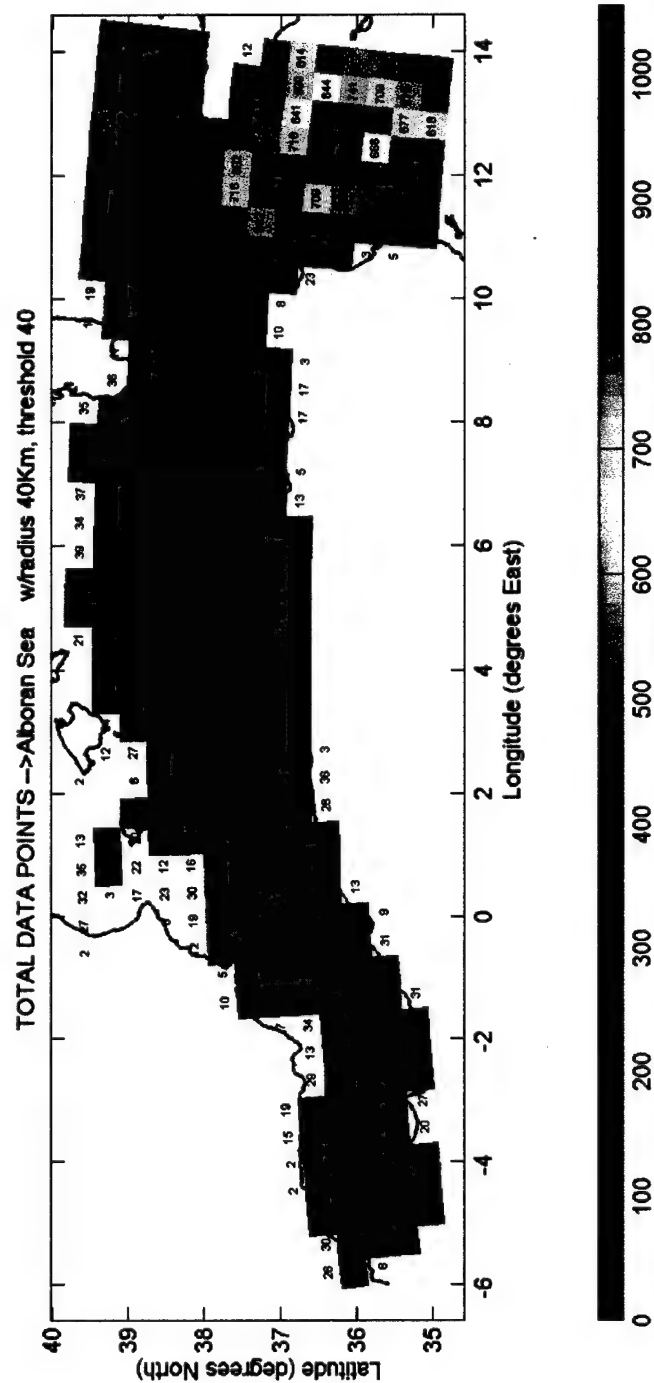


Figure 22. Region 1 data density. The total number of 6-hourly drifter observations per 40 km radius circular bin is displayed at the bin's center. A square color patch is also displayed at the bins center indicating the same quantity. A number within an uncolored patch indicates that the bin did not meet the threshold criterion of 40 6-hourly drifter observations.

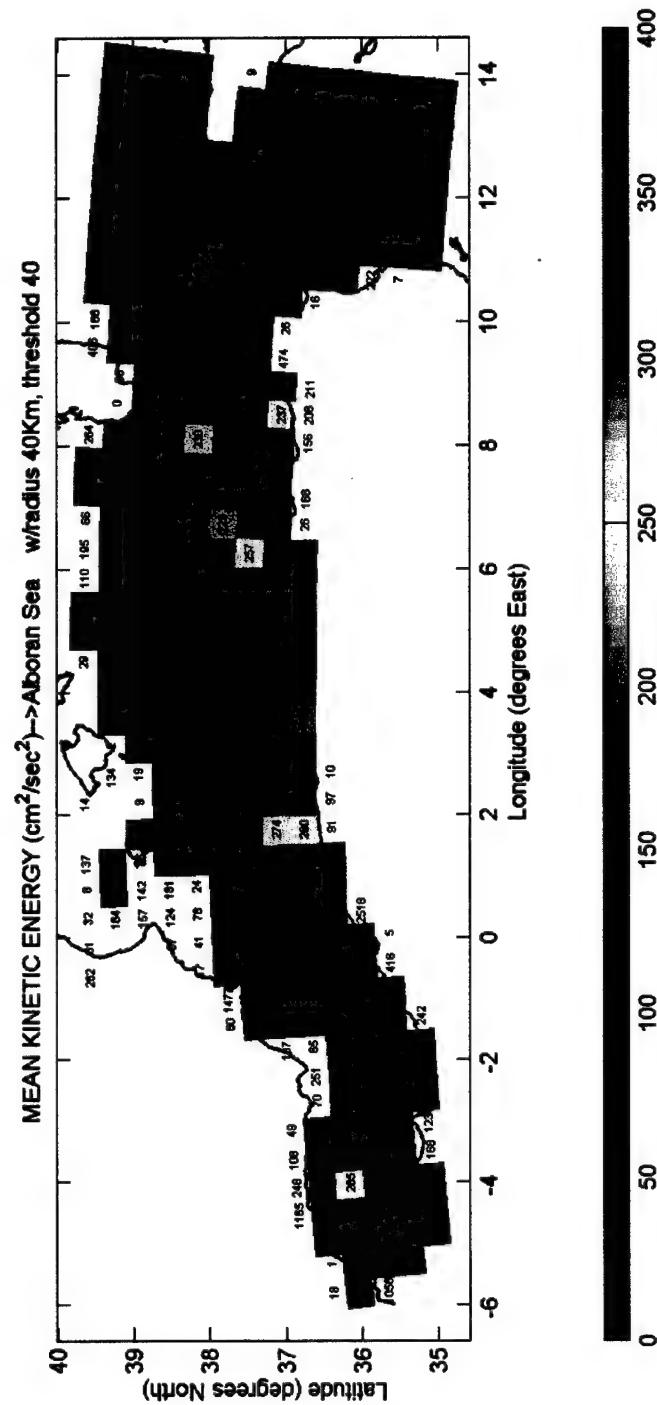


Figure 23. Region 1 MKE. The Mean Kinetic Energy (MKE) per 40 km radius circular bin is displayed at the bin's center. A square color patch is also displayed at the bins center indicating the same quantity. A number within an uncolored patch indicates that the bin did not meet the threshold criterion of 40 6-hourly drifter observations.

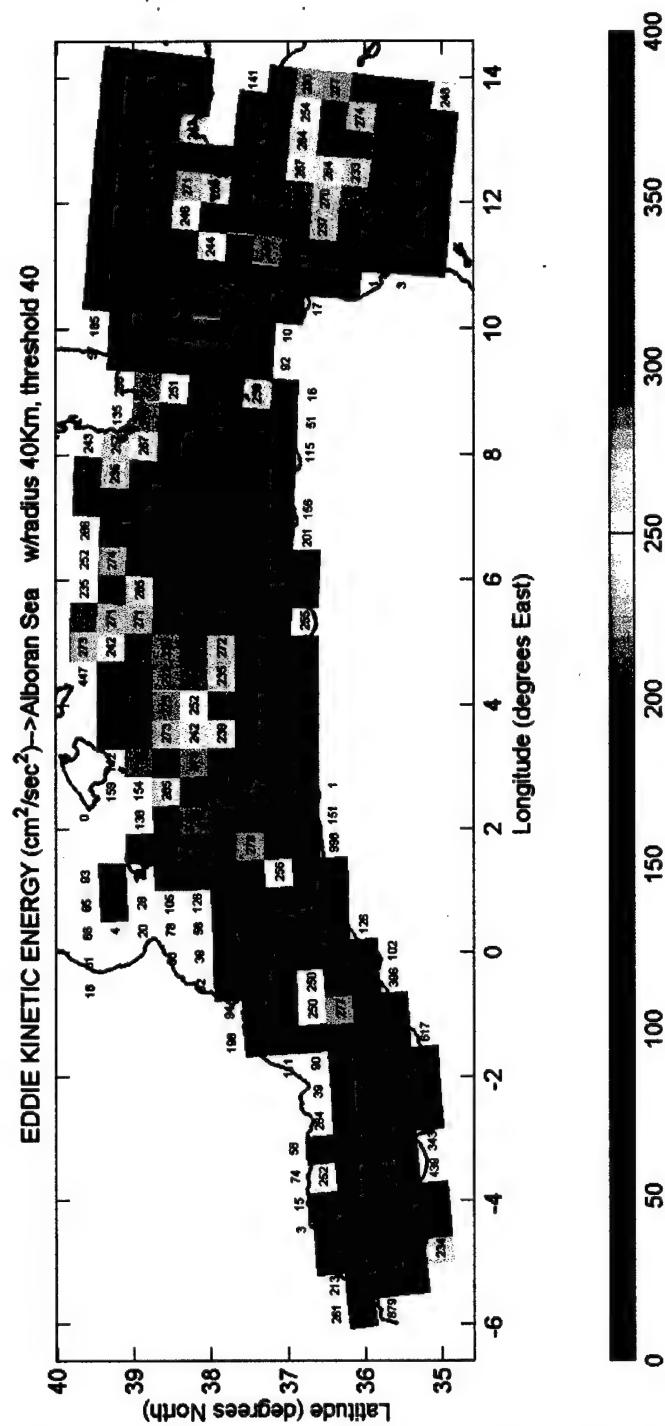


Figure 24. Region 1 EKE. The Eddy Kinetic Energy (EKE) per 40 km radius circular bin is displayed at the bin's center. A square color patch is also displayed at the bins center indicating the same quantity. A number within an uncolored patch indicates that the bin did not meet the threshold criterion of 40 6-hourly drifter observations.

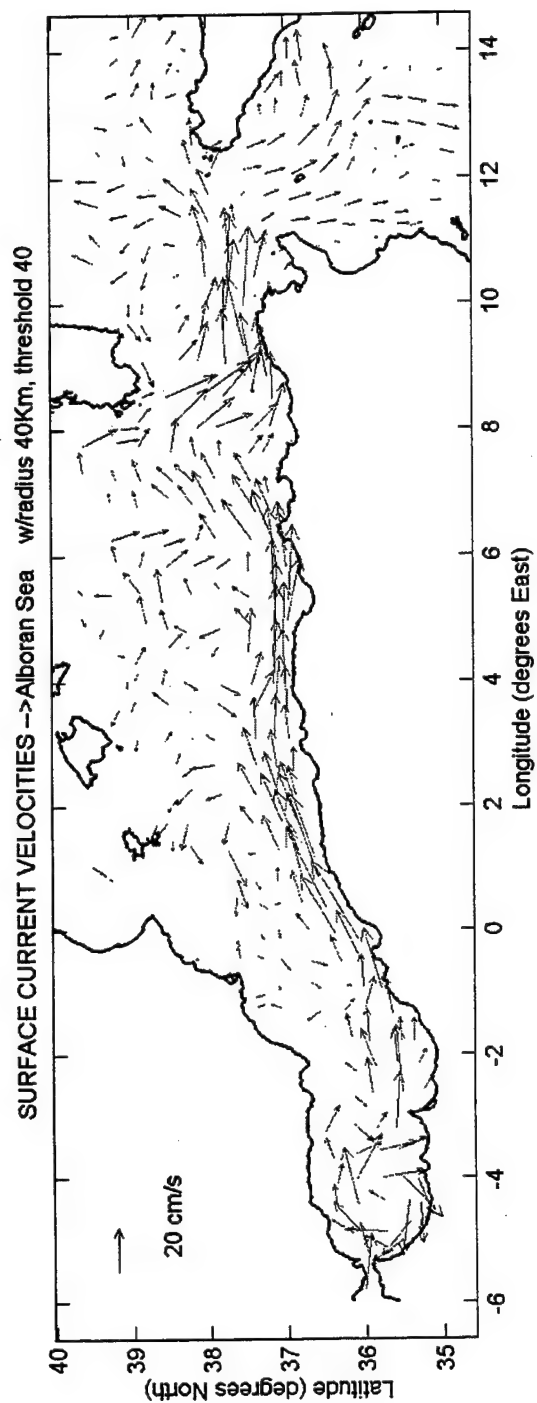


Figure 25. Region 1 surface flow. The average drifter velocity per 40 km radius circular bin is displayed at the center of mass of the drifter observations within each bin.

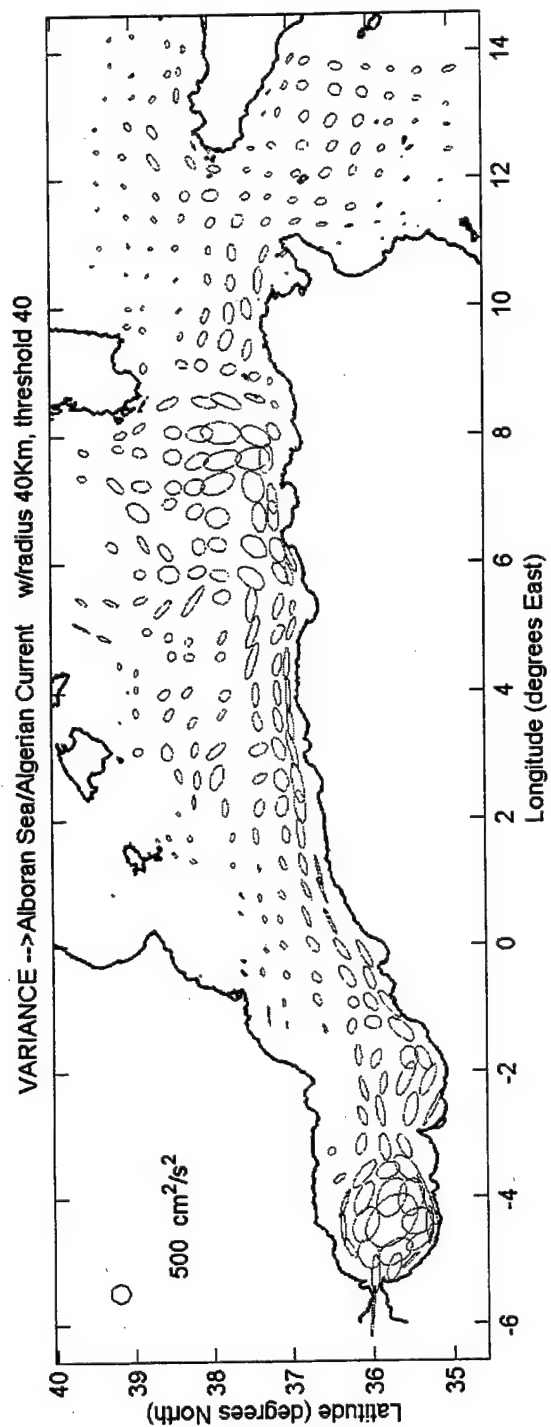


Figure 26. Region 1 surface flow variance. An ellipse defined by the principal axes of variance for each bin represents variance of surface flow. The ellipse is centered at the center of mass of the drifter observations within each bin.

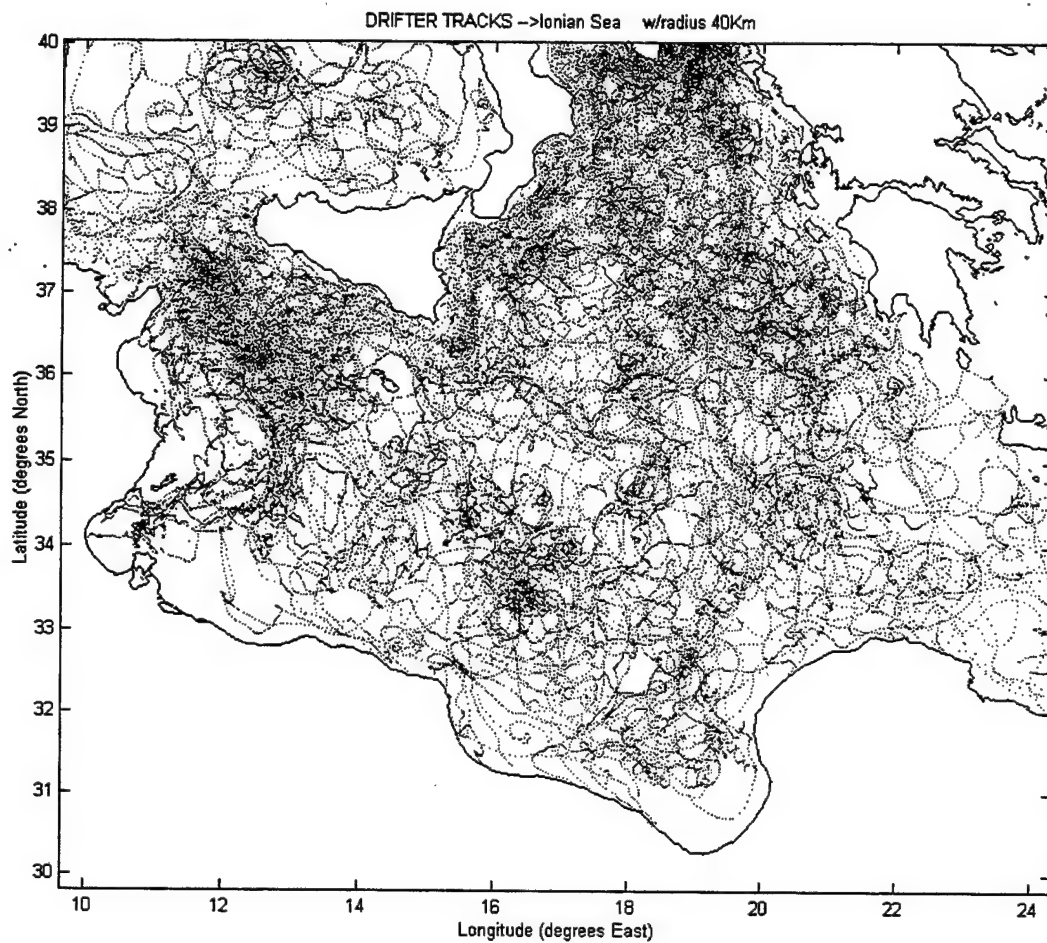


Figure 27. Region 2 drifter observations. Each 6-hourly drifter observation, which falls within any of the 40 km radius circular bins used to cover the entire area of the region, is plotted.

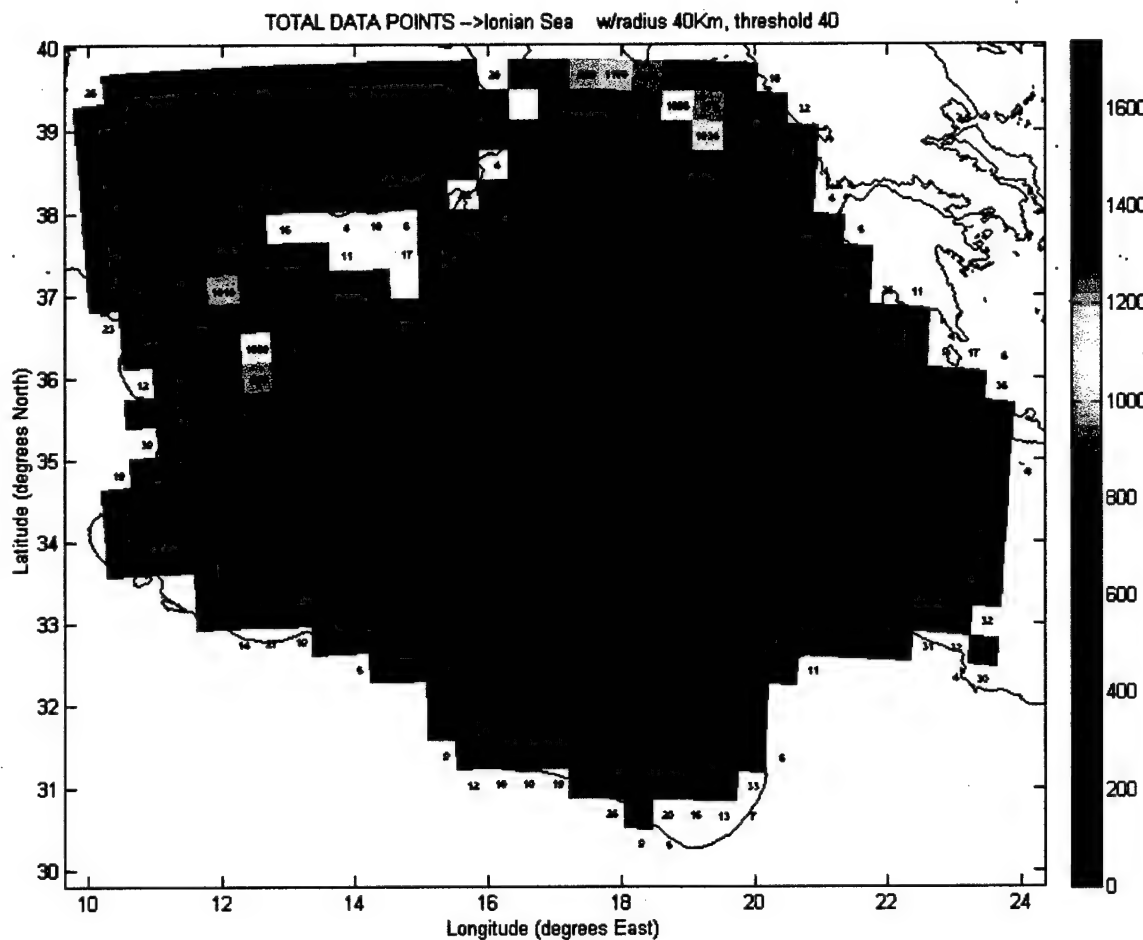


Figure 28. Region 2 data density. The total number of 6-hourly drifter observations per 40 km radius circular bin is displayed at the bin's center. A square color patch is also displayed at the bins center indicating the same quantity. A number within an uncolored patch indicates that the bin did not meet the threshold criterion of 40 6-hourly drifter observations.

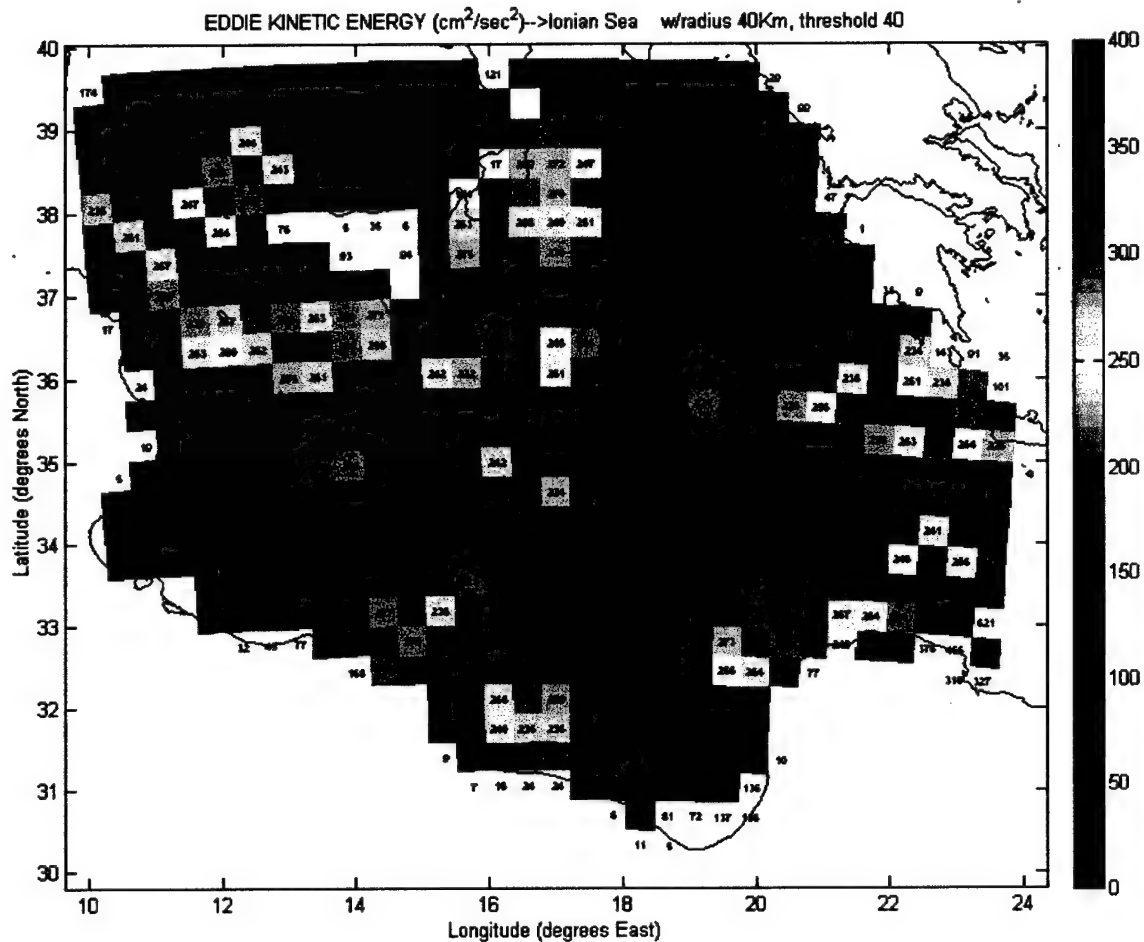


Figure 30. Region 2 EKE. The Eddy Kinetic Energy (EKE) per 40 km radius circular bin is displayed at the bin's center. A square color patch is also displayed at the bins center indicating the same quantity. A number within an uncolored patch indicates that the bin did not meet the threshold criterion of 40 6-hourly drifter observations.

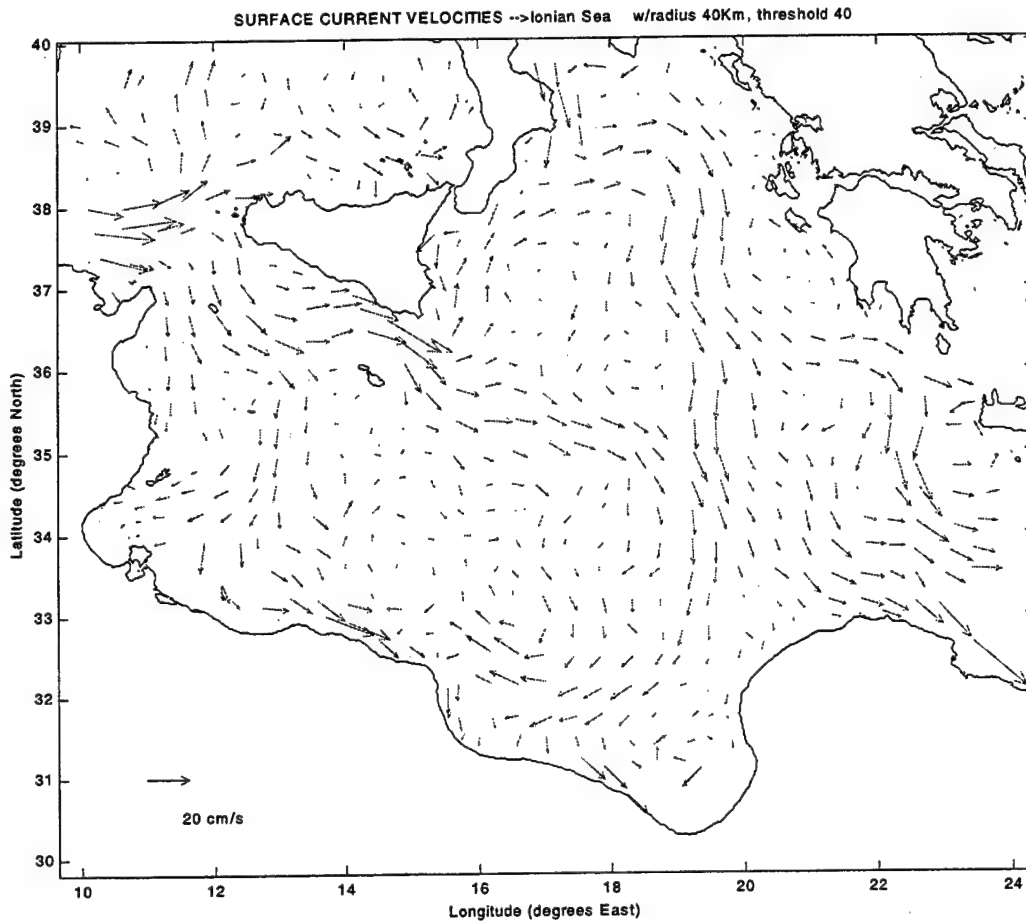


Figure 31. Region 2 surface flow. The average drifter velocity per 40 km radius circular bin is displayed at the center of mass of the drifter observations within each bin.

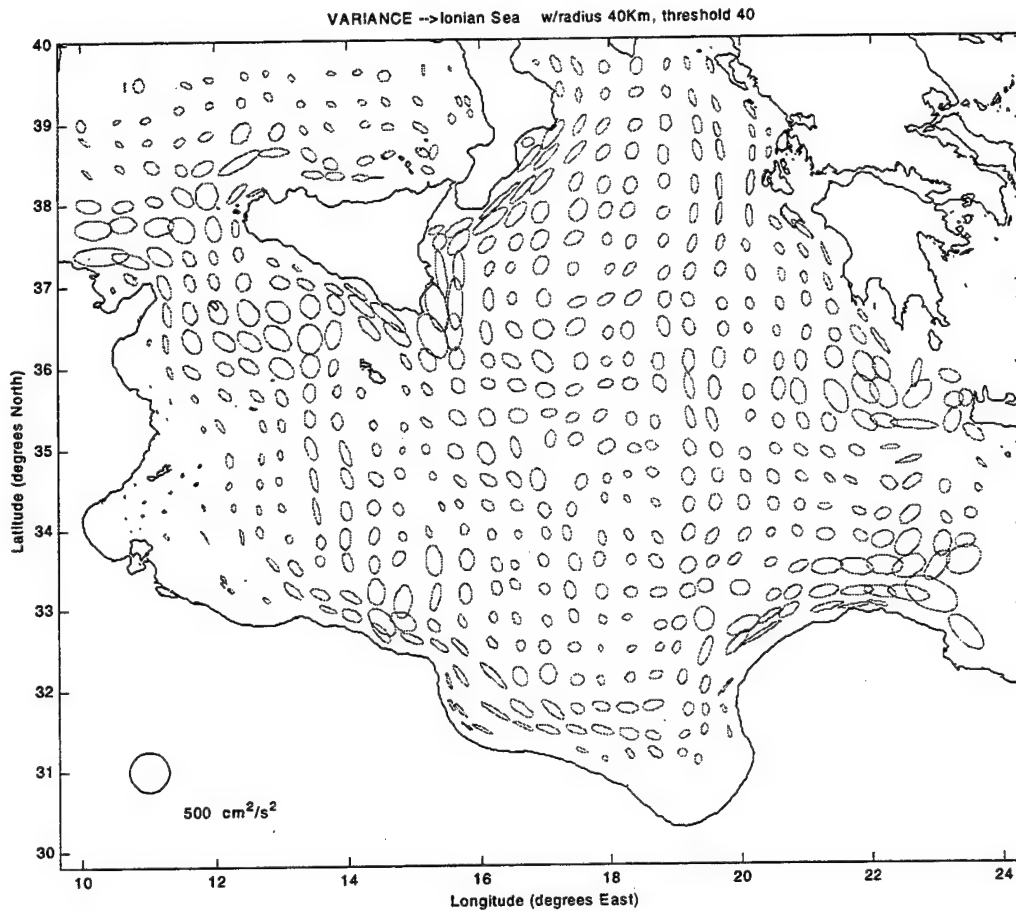


Figure 32. Region 2 flow variance. An ellipse defined by the principal axes of variance for each bin represents variance of surface flow. The ellipse is centered at the center of mass of the drifter observations within each bin.

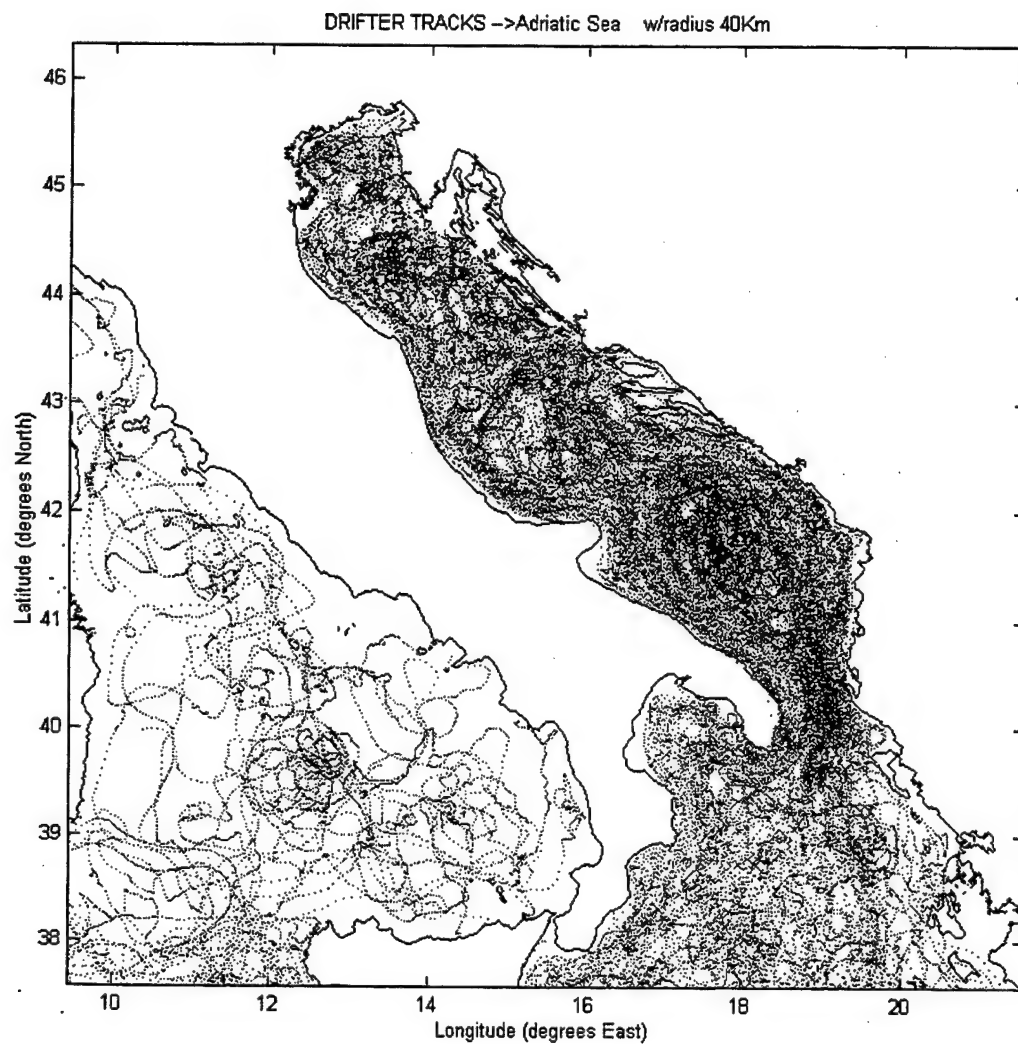


Figure 33. Region 3 drifter observations. Each 6-hourly drifter observation, which falls within any of the 40 km radius circular bins used to cover the entire area of the region, is plotted.

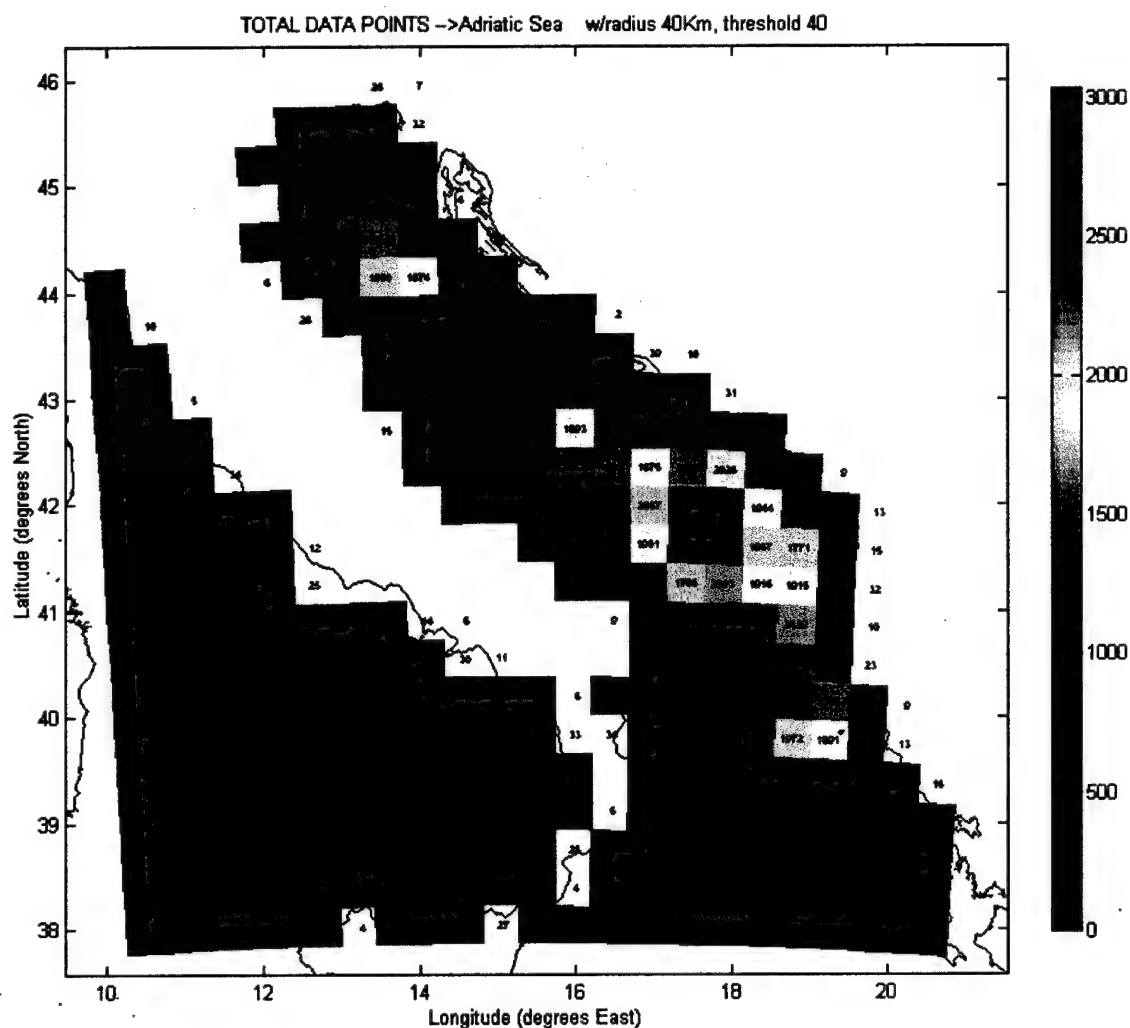


Figure 34. Region 3 data density. The total number of 6-hourly drifter observations per 40 km radius circular bin is displayed at the bin's center. A square color patch is also displayed at the bins center indicating the same quantity. A number within an uncolored patch indicates that the bin did not meet the threshold criterion of 40 6-hourly drifter observations.

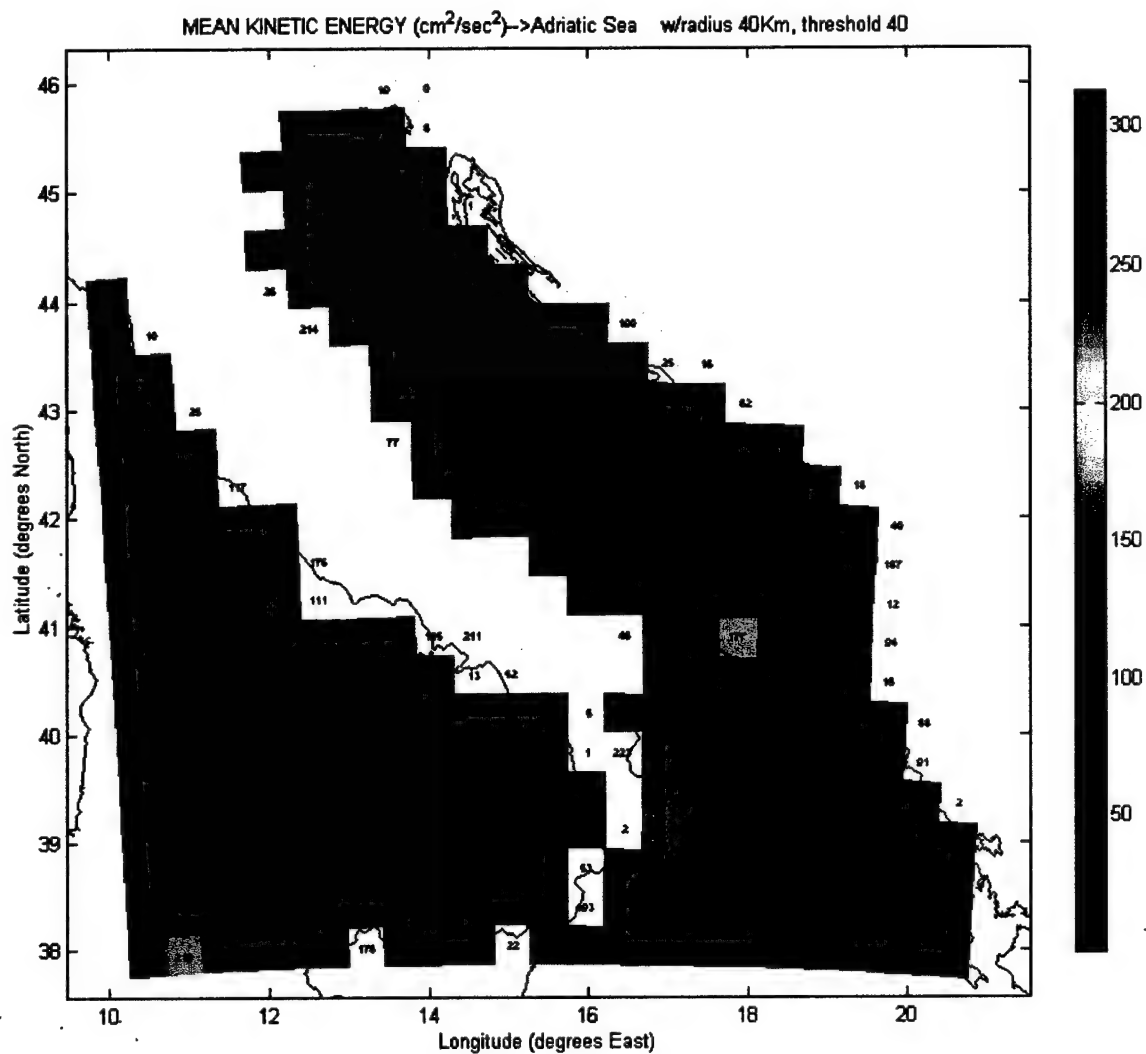


Figure 35. Region 3 MKE. The Mean Kinetic Energy (MKE) per 40 km radius circular bin is displayed at the bin's center. A square color patch is also displayed at the bins center indicating the same quantity. A number within an uncolored patch indicates that the bin did not meet the threshold criterion of 40 6-hourly drifter observations.

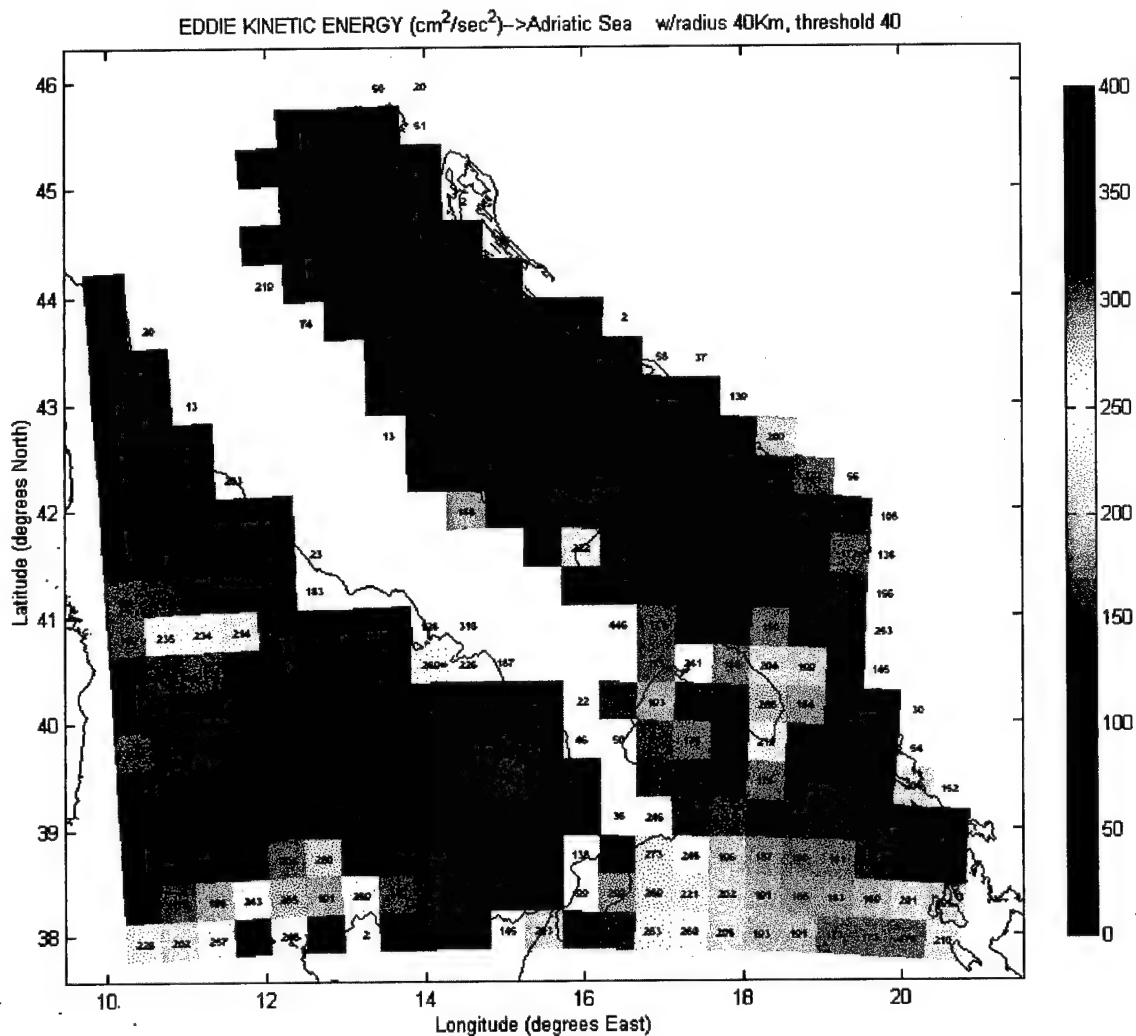


Figure 36. Region 3 EKE. The Eddy Kinetic Energy (EKE) per 40 km radius circular bin is displayed at the bin's center. A square color patch is also displayed at the bins center indicating the same quantity. A number within an uncolored patch indicates that the bin did not meet the threshold criterion of 40 6-hourly drifter observations.

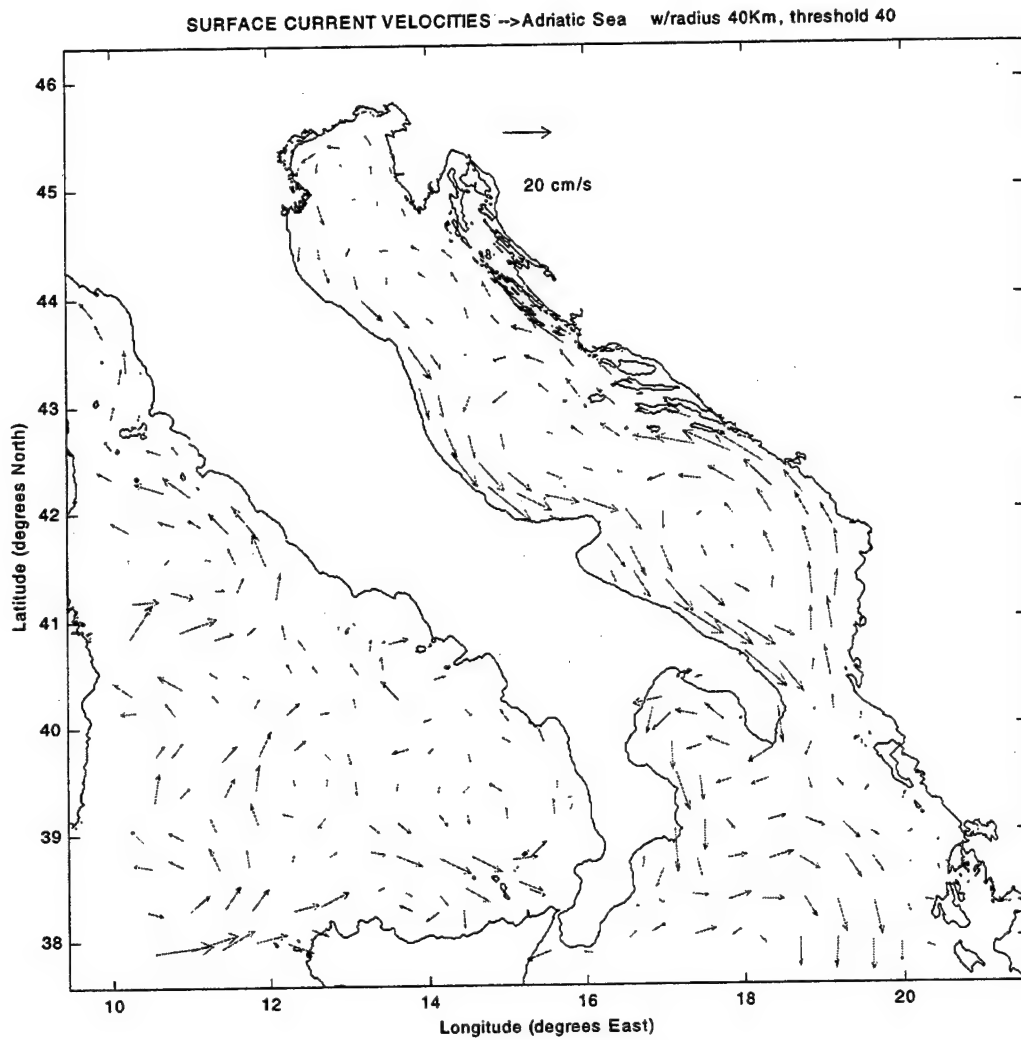


Figure 37. Region 3 surface flow. The average drifter velocity per 40 km radius circular bin is displayed at the center of mass of the drifter observations within each bin.

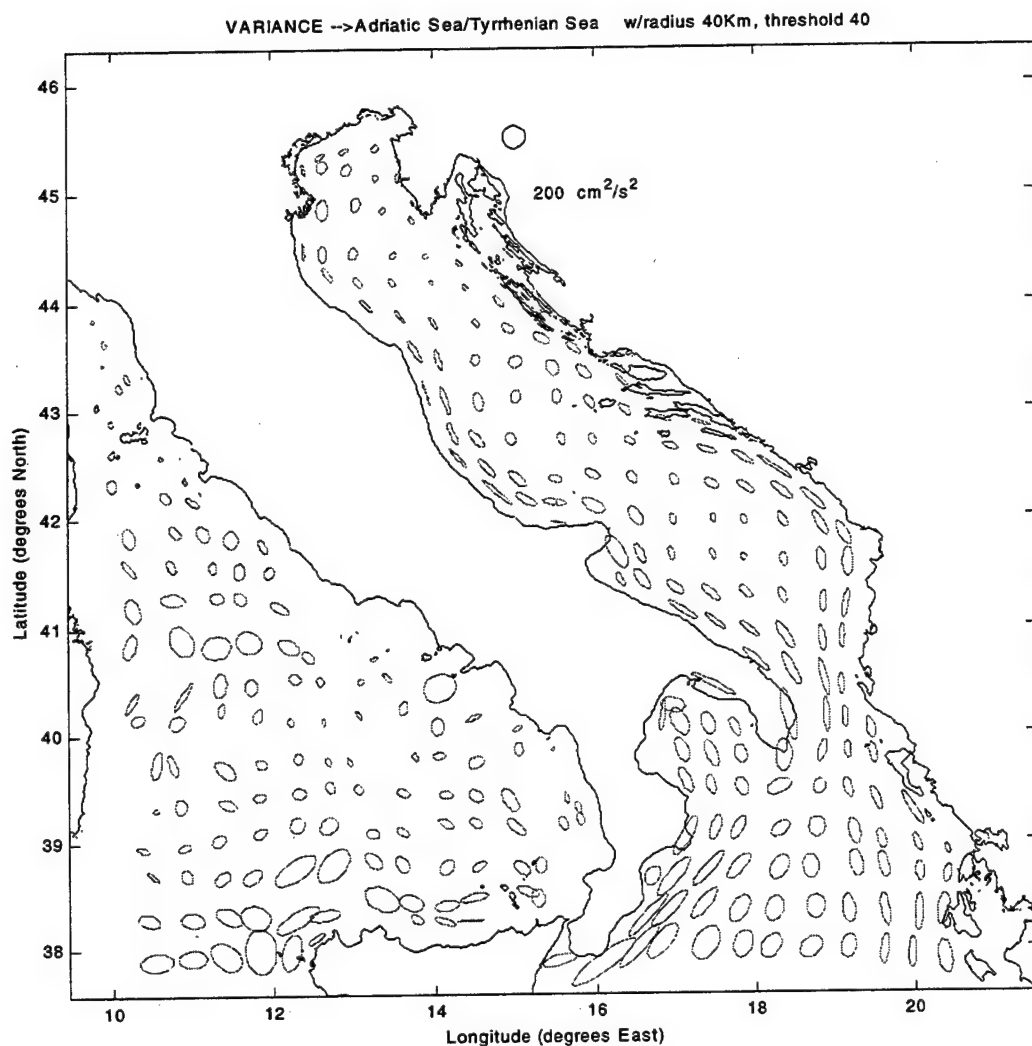


Figure 38. Region 3 flow variance. An ellipse defined by the principal axes of variance for each bin represents variance of surface flow. The ellipse is centered at the center of mass of the drifter observations within each bin.

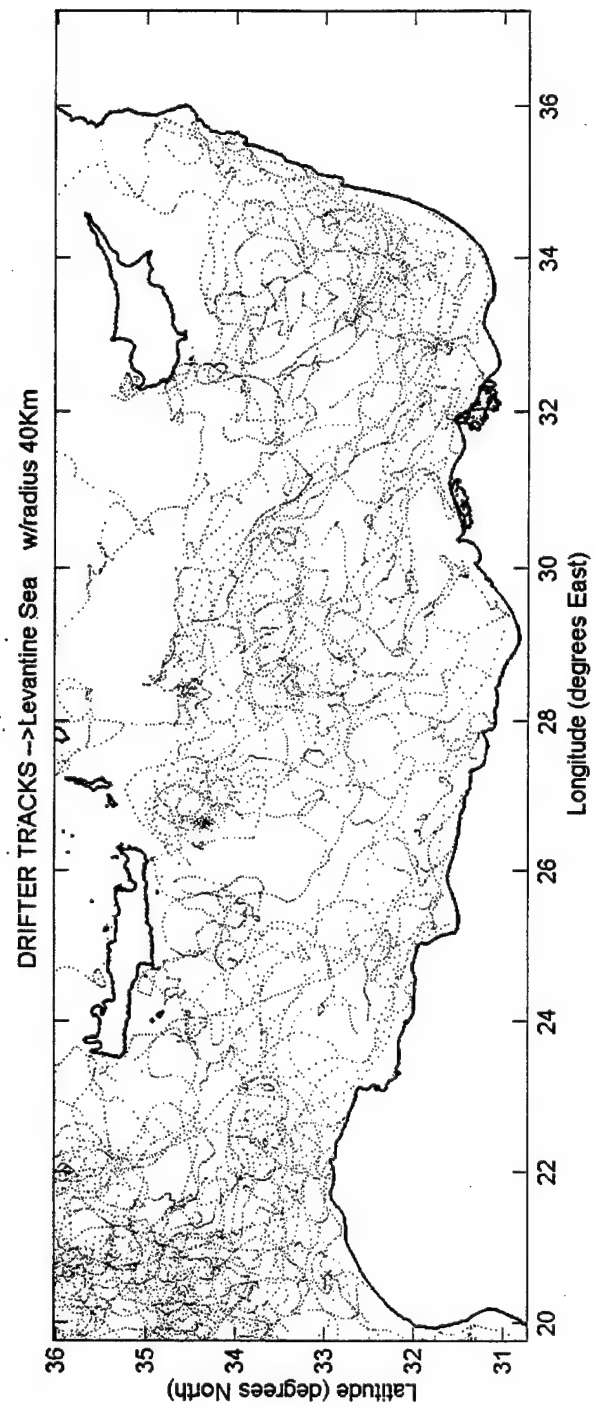


Figure 39. Region 4 drifter observations. Each 6-hourly drifter observation, which falls within any of the 40 km radius circular bins used to cover the entire area of the region, is plotted.

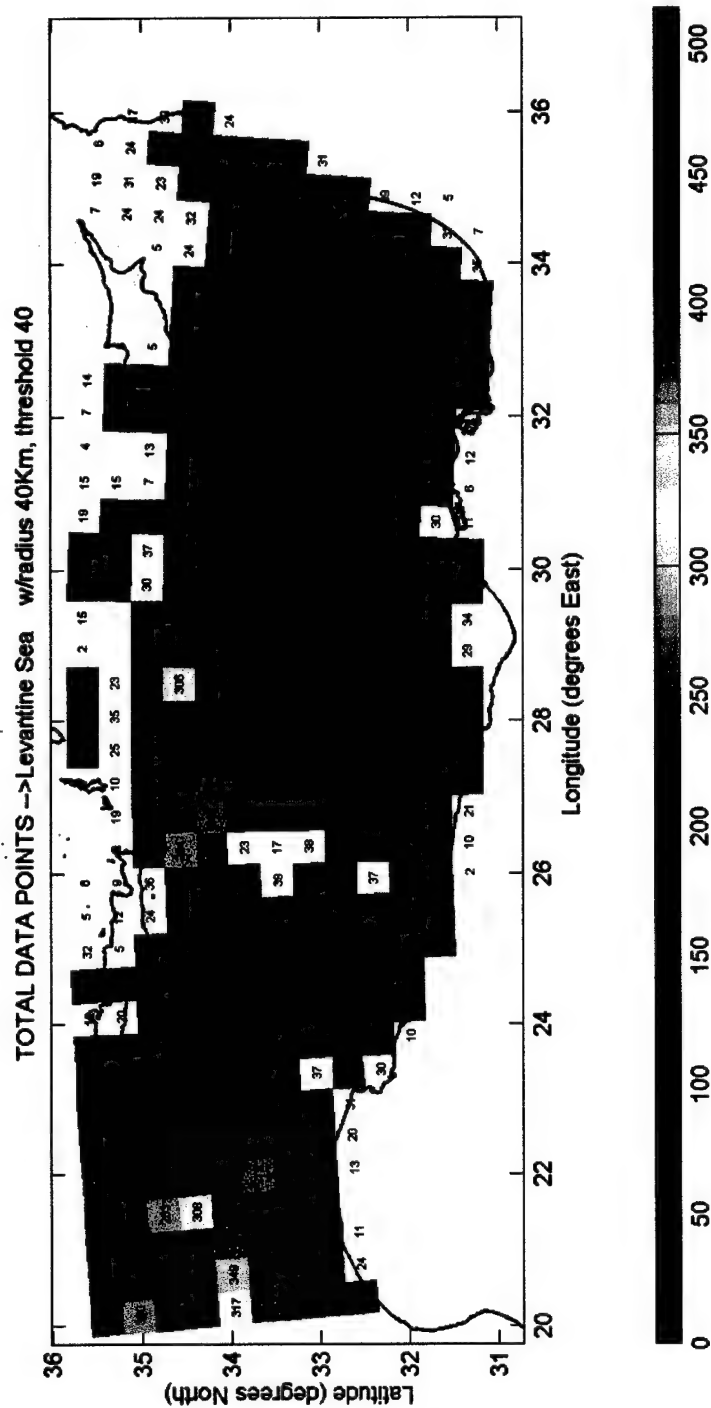


Figure 40. Region 4 data density. The total number of 6-hourly drifter observations per 40 km radius circular bin is displayed at the bin's center. A square color patch is also displayed at the bins center indicating the same quantity. A number within an uncolored patch indicates that the bin did not meet the threshold criterion of 40 6-hourly drifter observations.

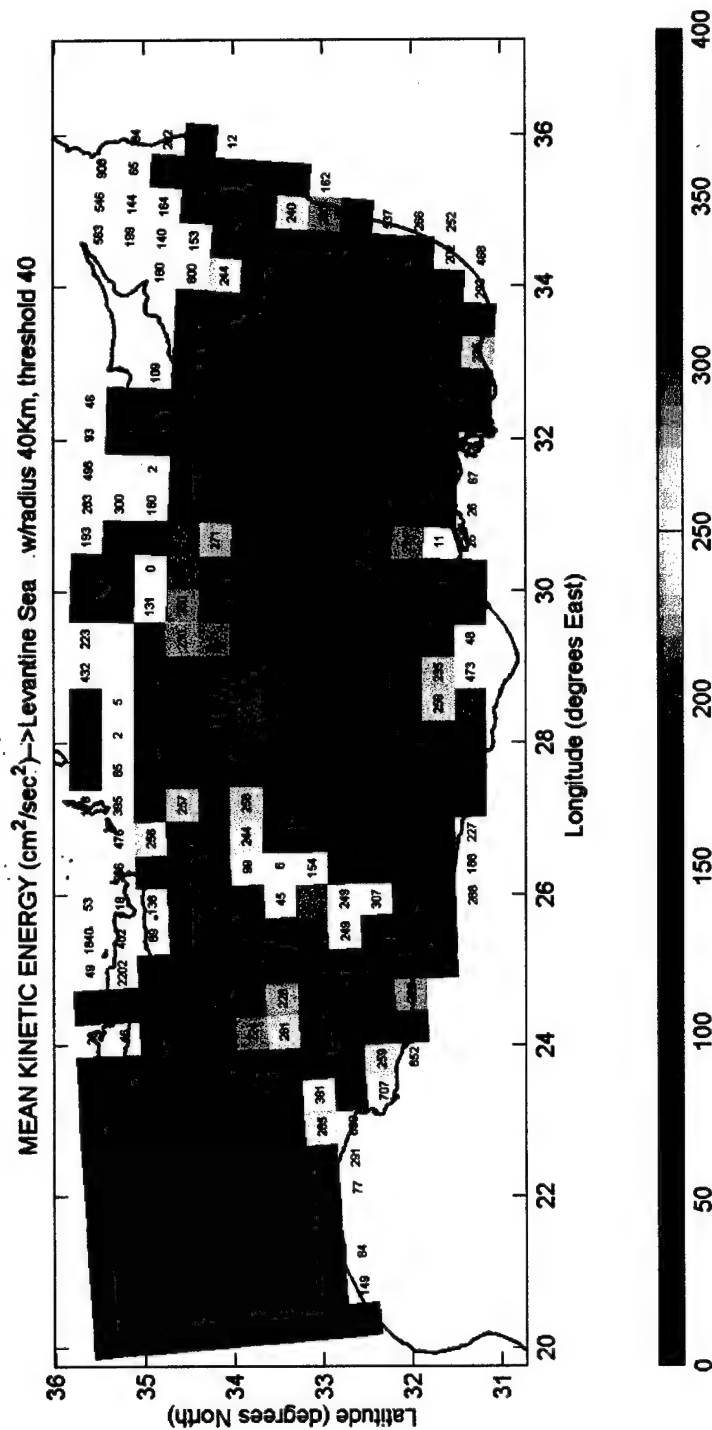


Figure 41. Region 4 MKE. The Mean Kinetic Energy (MKE) per 40 km radius circular bin is displayed at the bin's center. A square color patch is also displayed at the bins center indicating the same quantity. A number within an uncolored patch indicates that the bin did not meet the threshold criterion of 40 6-hourly drifter observations.

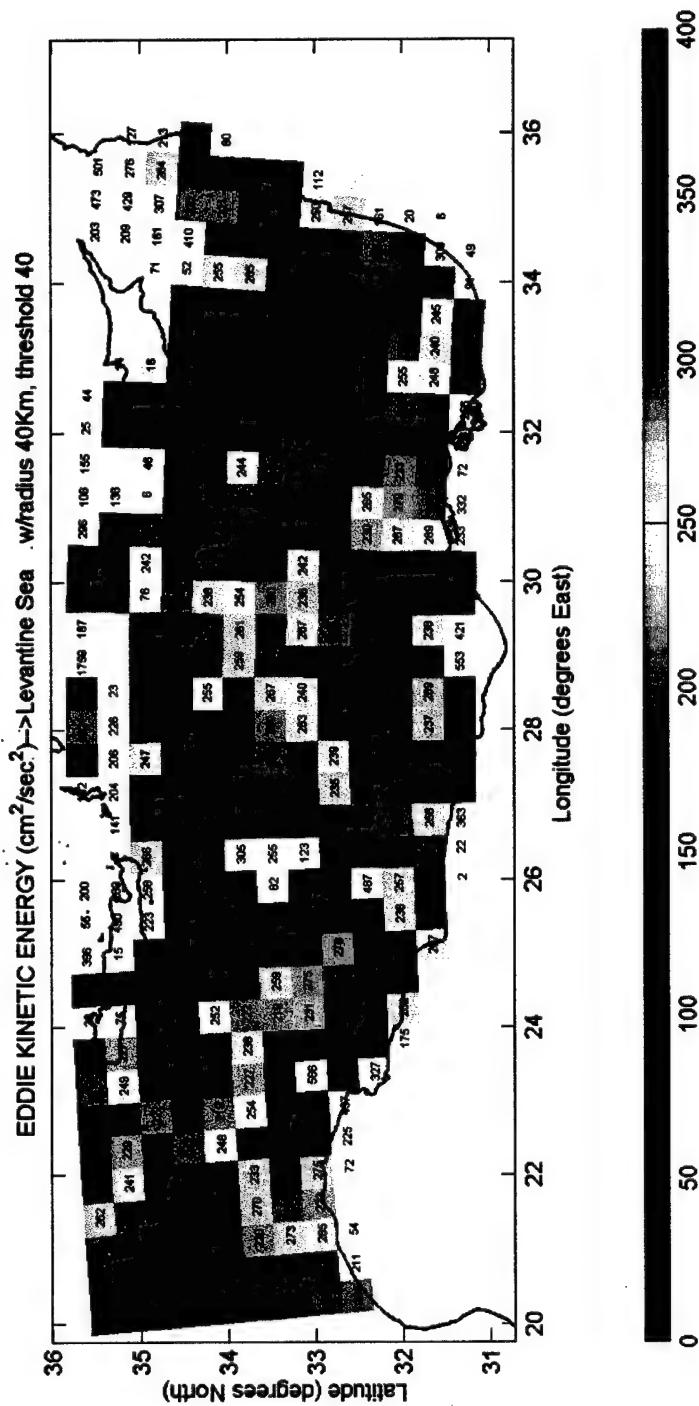


Figure 42. Region 4 EKE. The Eddy Kinetic Energy (EKE) per 40 km radius circular bin is displayed at the bin's center. A square color patch is also displayed at the bins center indicating the same quantity. A number within an uncolored patch indicates that the bin did not meet the threshold criterion of 40 6-hourly drifter observations.

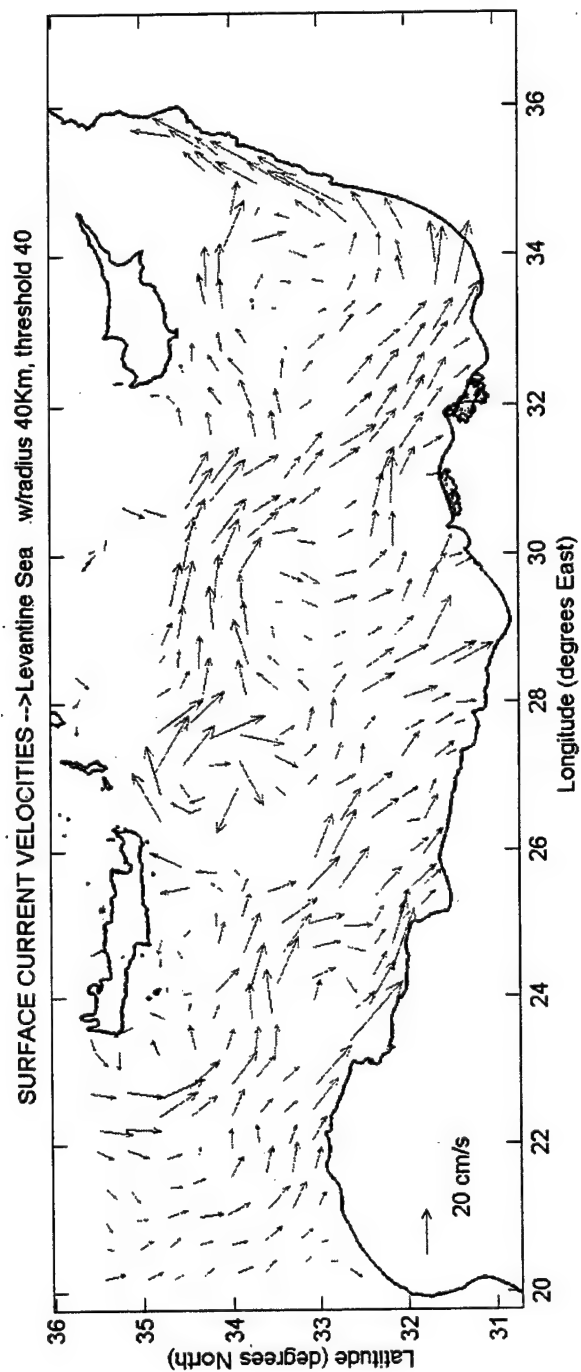


Figure 43. Region 4 surface flow. The average drifter velocity per 40 km radius circular bin is displayed at the center of mass of drifter observations within each bin.

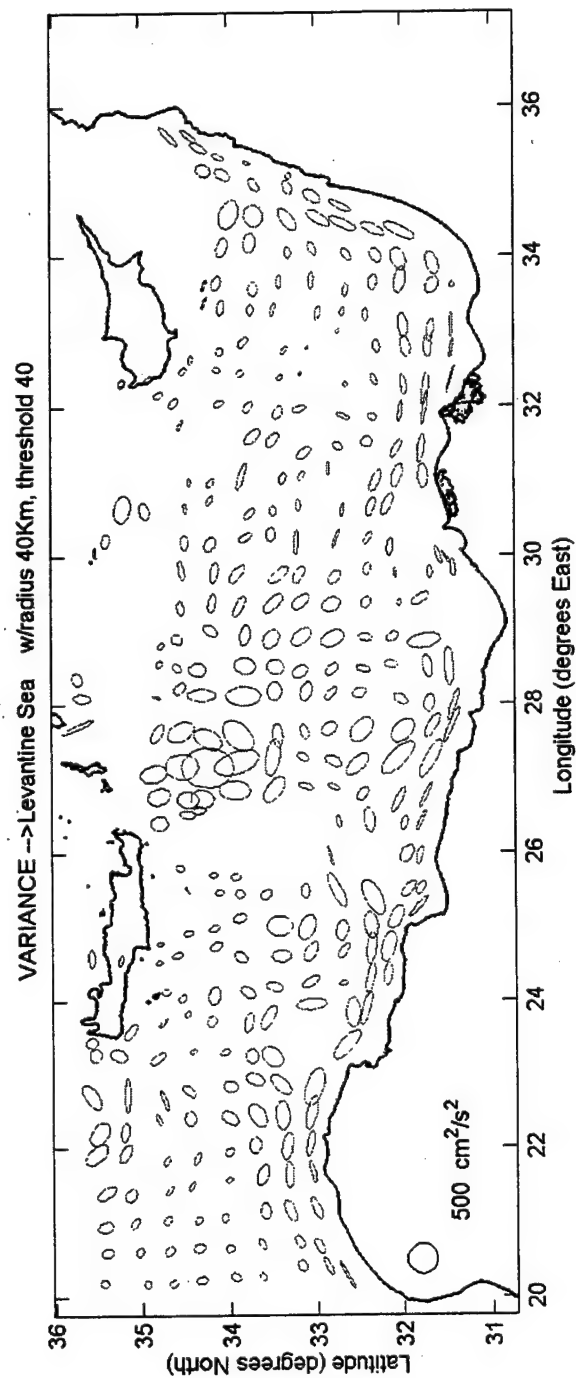


Figure 44. Region 4 flow variance. An ellipse defined by the principal axes of variance for each bin represents variance of surface flow. The ellipse is centered at the center of mass of the drifter observations within each bin.

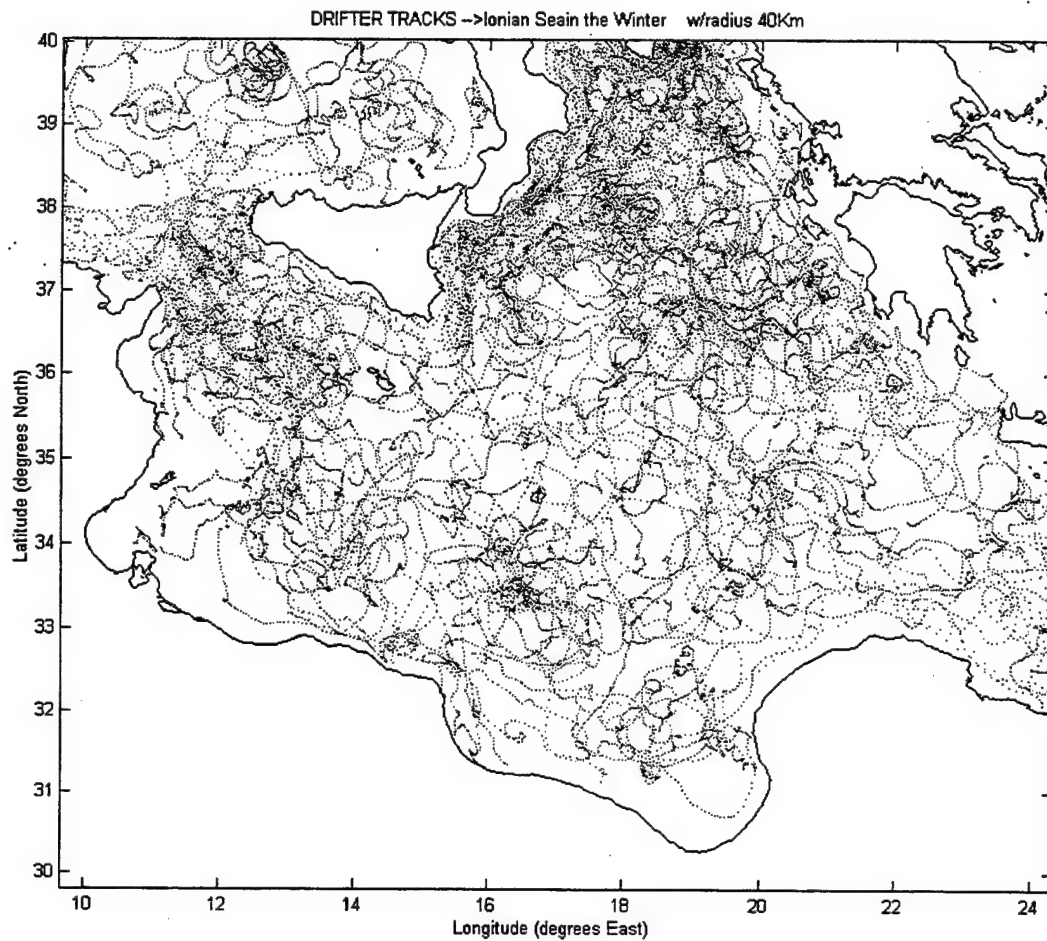


Figure 45. Region 2 winter 6-hourly observations. Each winter 6-hourly drifter observation, which falls within any of the 40 km radius circular bins used to cover the entire area of the region, is plotted. Winter is considered as the 6-month period beginning in November and ending in April.

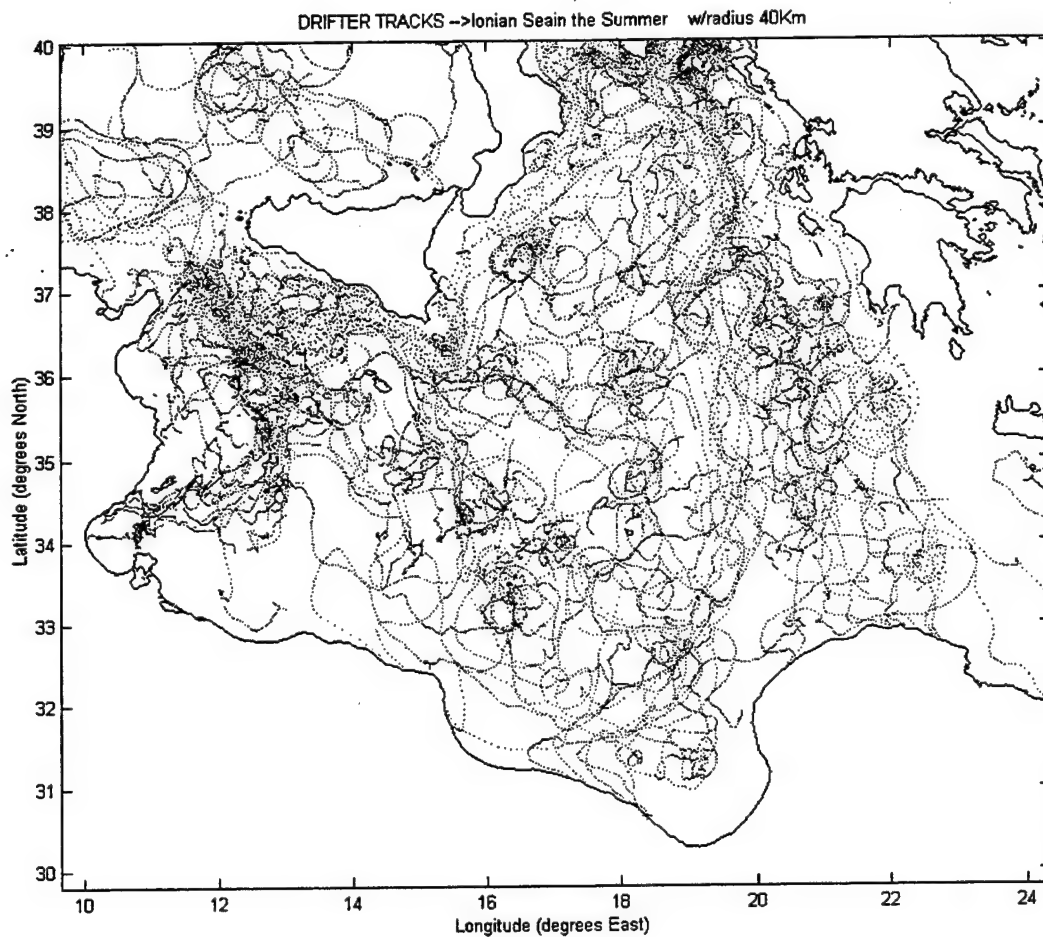


Figure 46. Region 2 summer 6-hourly observations. Each summer 6-hourly drifter observation, which falls within any of the 40 km radius circular bins used to cover the entire area of the region, is plotted. Summer is defined as the 6-month period beginning in May and ending in October.

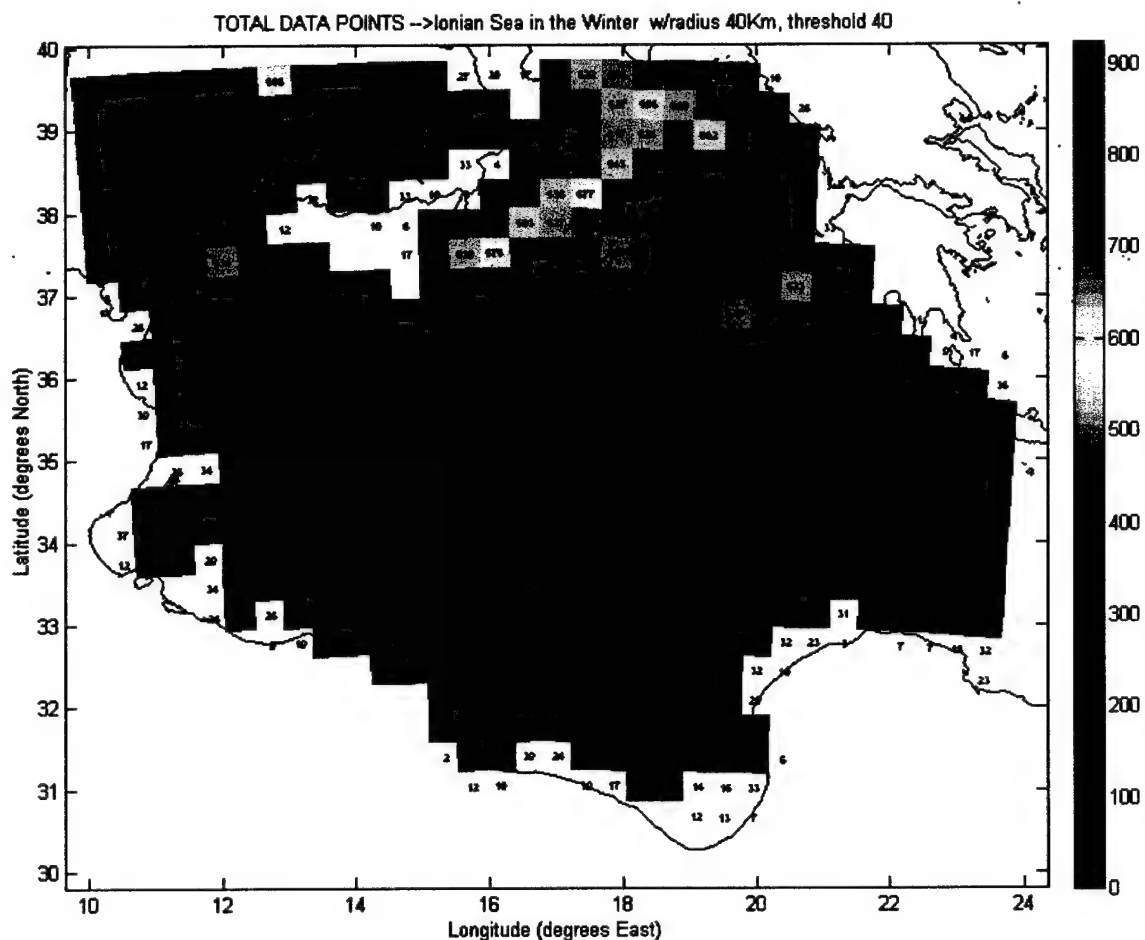


Figure 47. Region 2 winter data density. The total number of winter 6-hourly drifter observations per 40 km radius circular bin is displayed at the bin's center. A square color patch is also displayed at the bins center indicating the same quantity. A number within an uncolored patch indicates that the bin did not meet the threshold criterion of 40 6-hourly drifter observations. Winter is defined as the 6-month period beginning in November and ending in April.

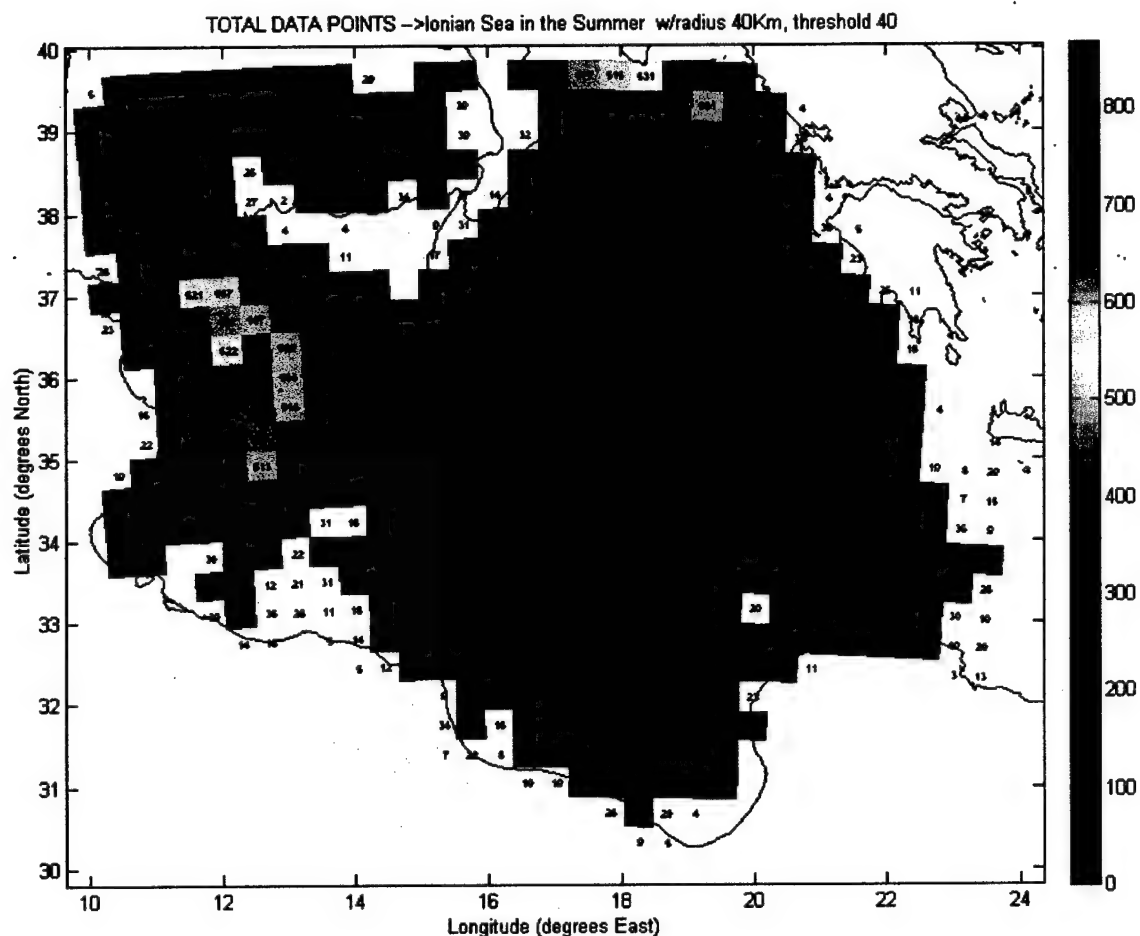


Figure 48. Region 2 summer data density. The total number of summer 6-hourly drifter observations per 40 km radius circular bin is displayed at the bin's center. A square color patch is also displayed at the bins center indicating the same quantity. A number within an uncolored patch indicates that the bin did not meet the threshold criterion of 40 6-hourly drifter observations. Summer is defined as the 6-month period beginning in May and ending in October.

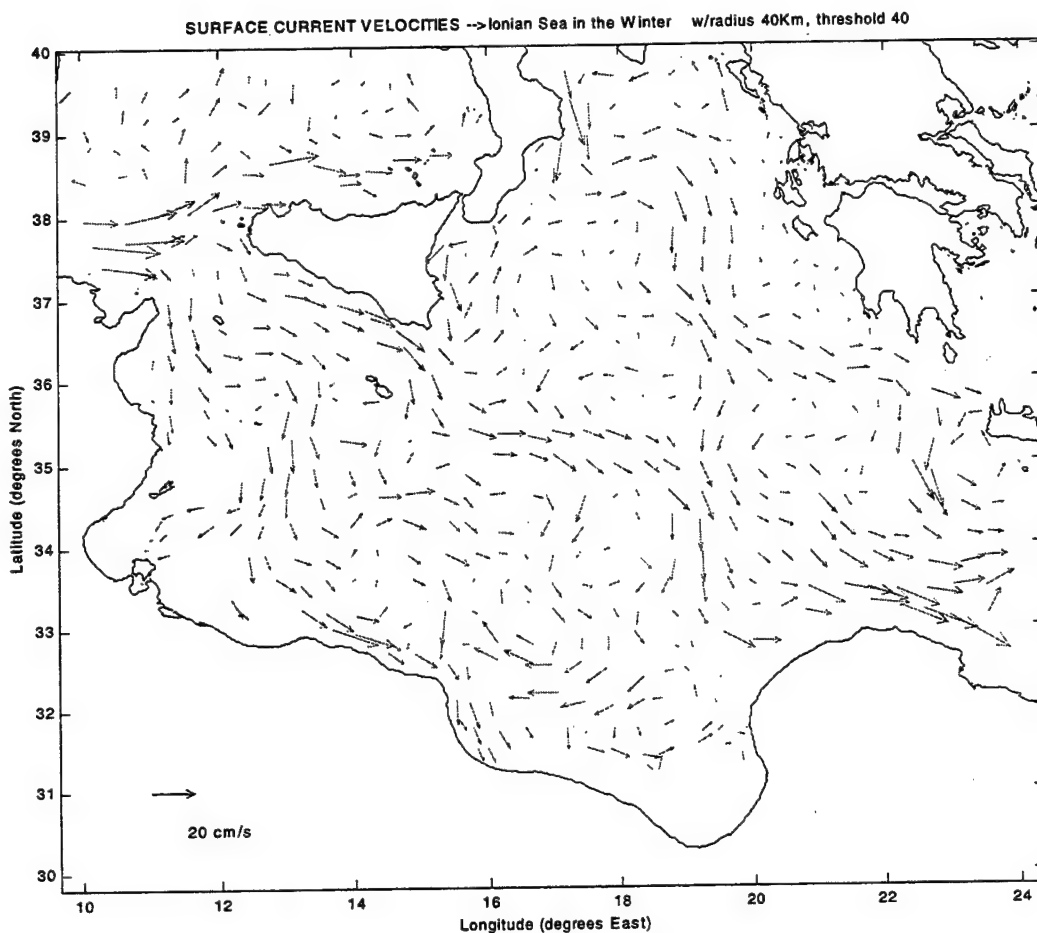


Figure 49. Region 2 winter surface flow. The average drifter velocity per 40 km radius circular bin is displayed at the center of mass of drifter observations within each bin. Winter is defined as the 6-month period beginning in November and ending in April.

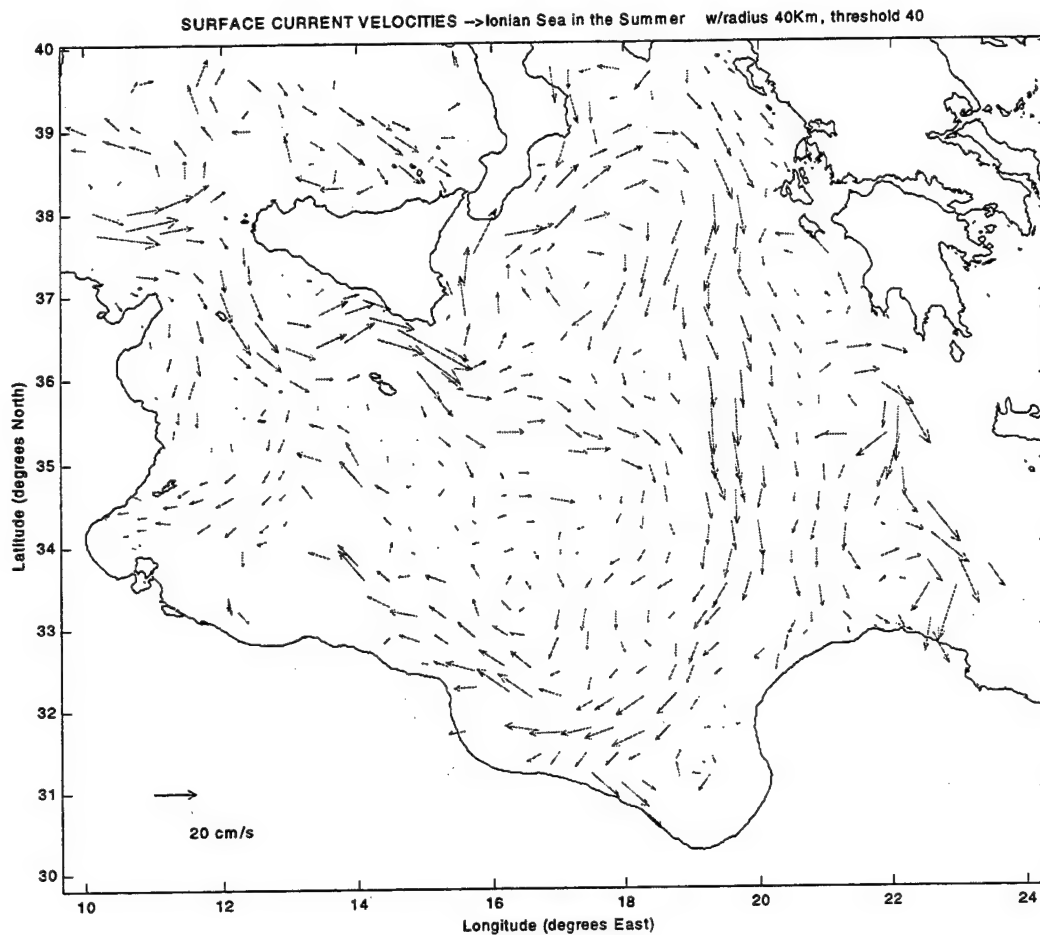


Figure 50. Region 2 summer surface flow. The average drifter velocity per 40 km radius circular bin is displayed at the center of mass of drifter observations within each bin. Summer is defined as the 6-month period beginning in May and ending in October.

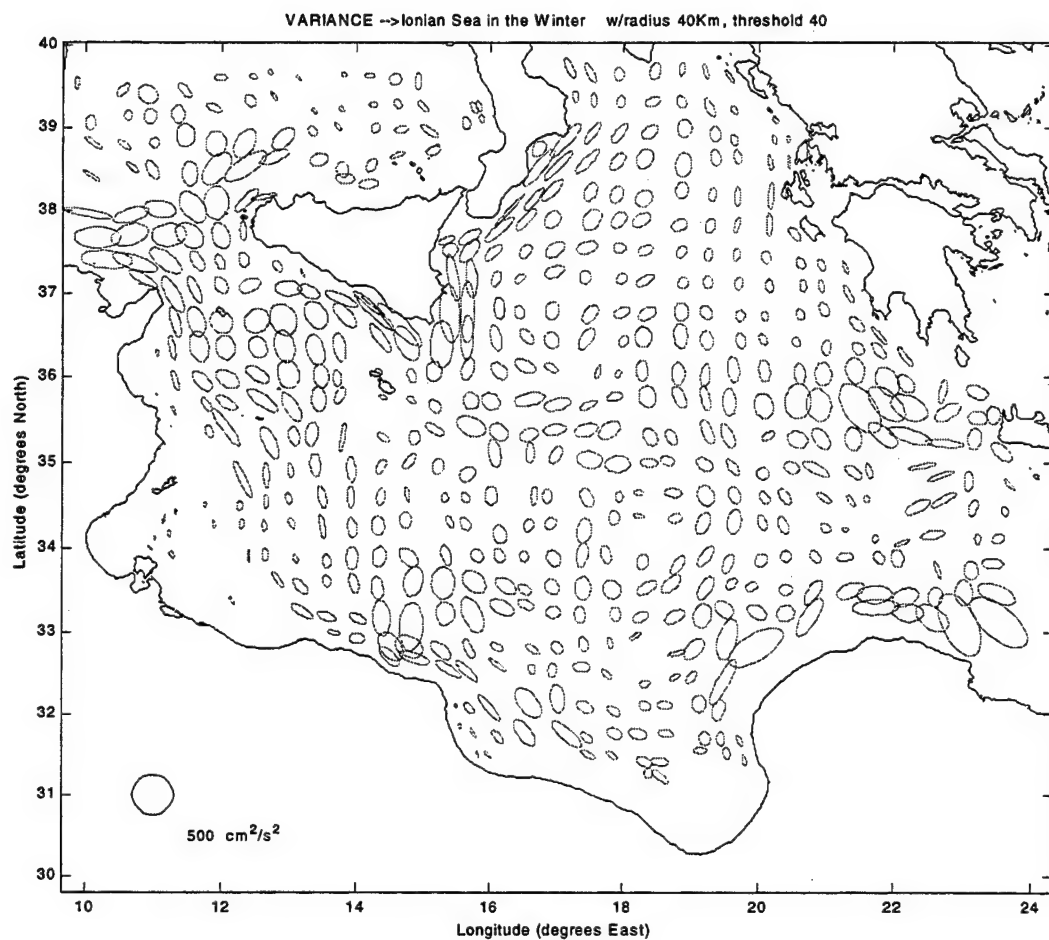


Figure 51. Region 2 winter flow variance. An ellipse defined by the principal axes of variance for each bin represents variance of surface flow. The ellipse is centered at the center of mass of drifter observations within each bin. Winter is defined as the 6-month period beginning in November and ending in April.

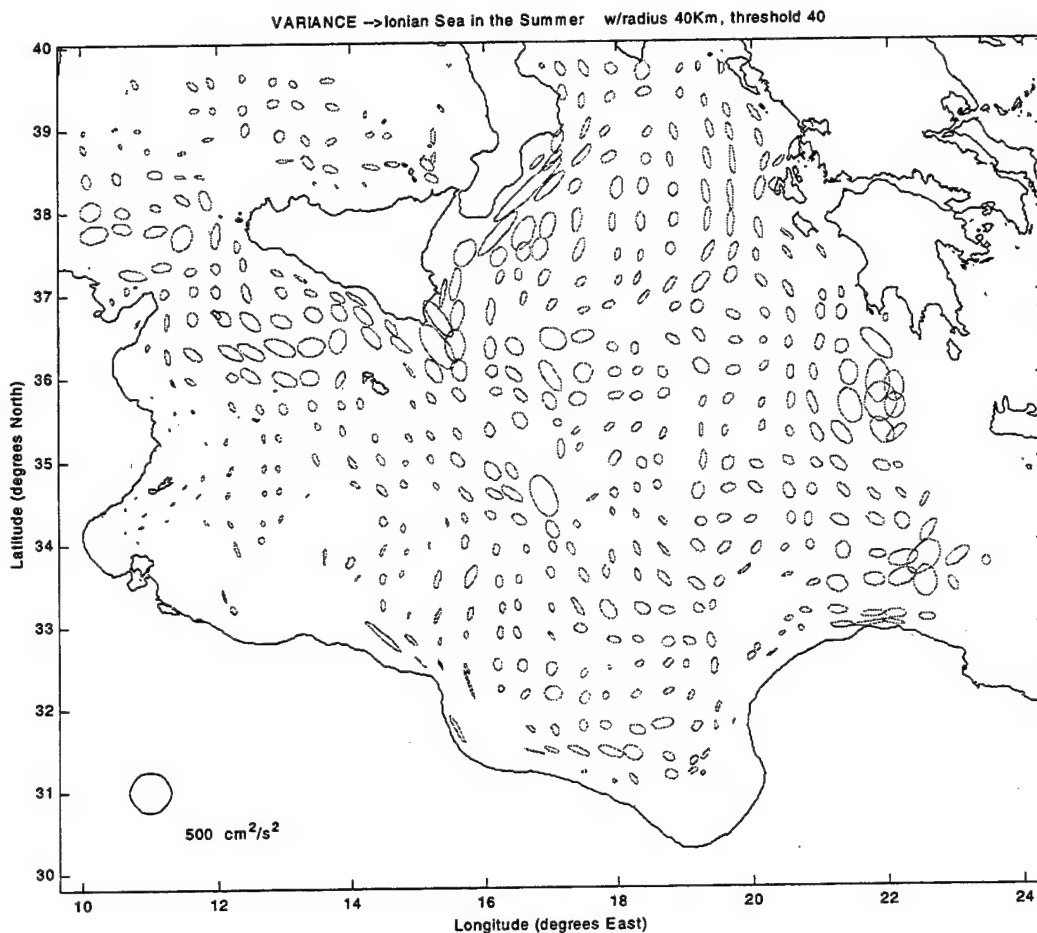


Figure 52. Region 2 summer flow variance. An ellipse defined by the principal axes of variance for each bin represents variance of surface flow. The ellipse is centered at the center of mass of drifter observations within each bin. Summer is defined as the 6-month period beginning in May and ending in October.

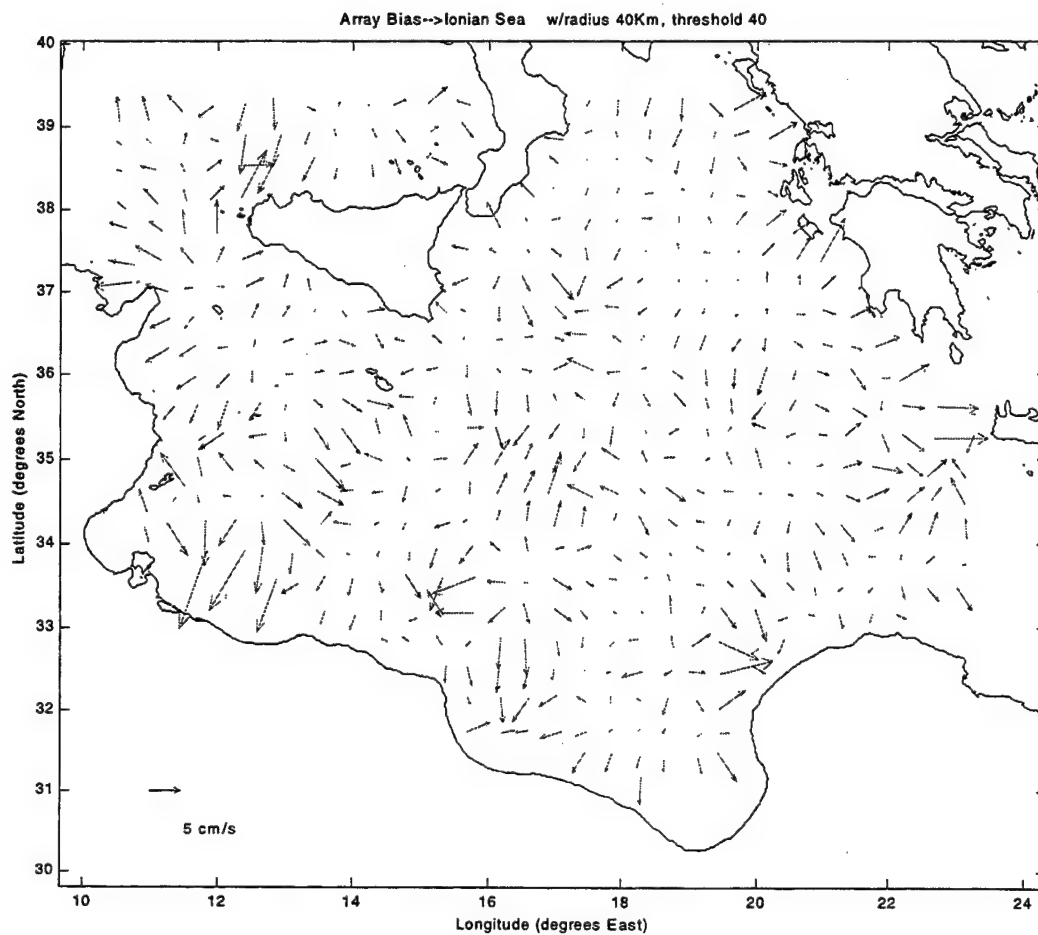


Figure 53. Region 2 array bias. The array bias per 40 km radius circular bin is displayed at the center of mass of drifter observations within each bin.

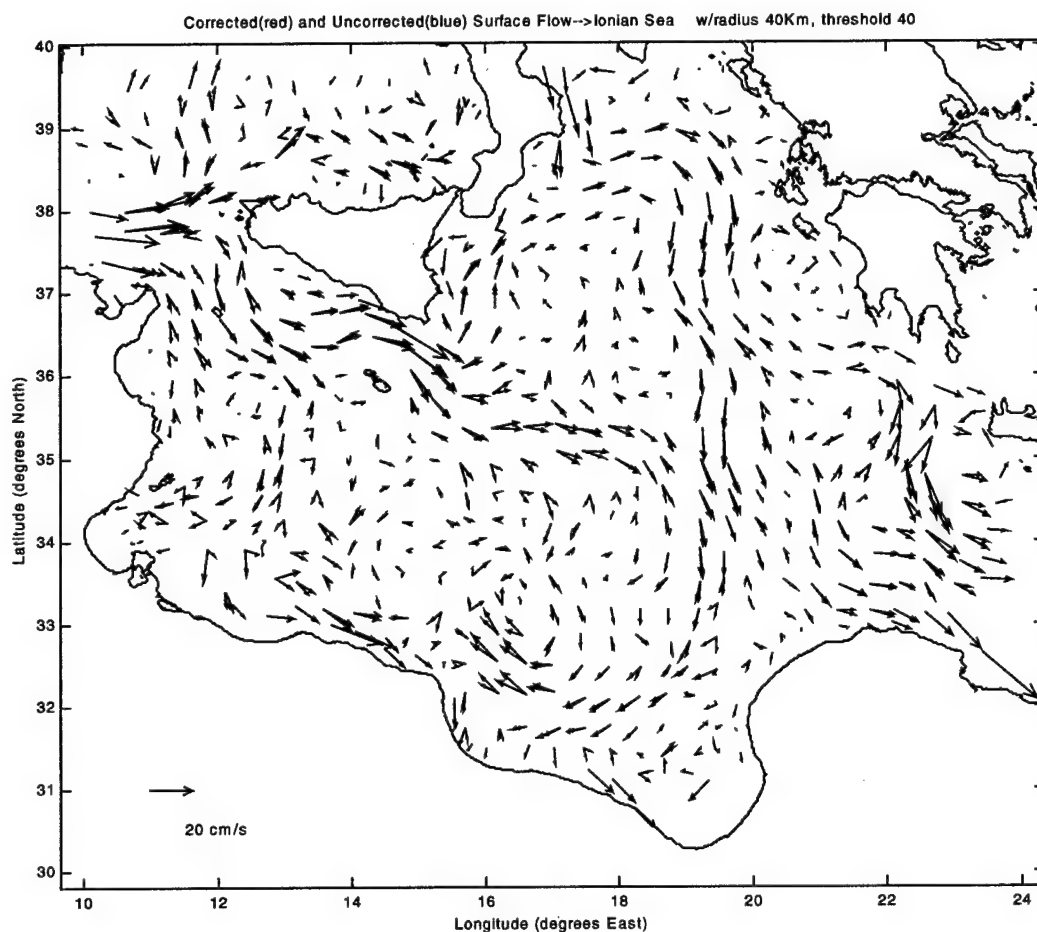


Figure 54. Region 2 surface flow (array bias corrected). The mean surface flow corrected (red) and uncorrected (blue) for the array bias per 40 km radius circular bin is displayed at the center of mass of drifter observations within each bin.

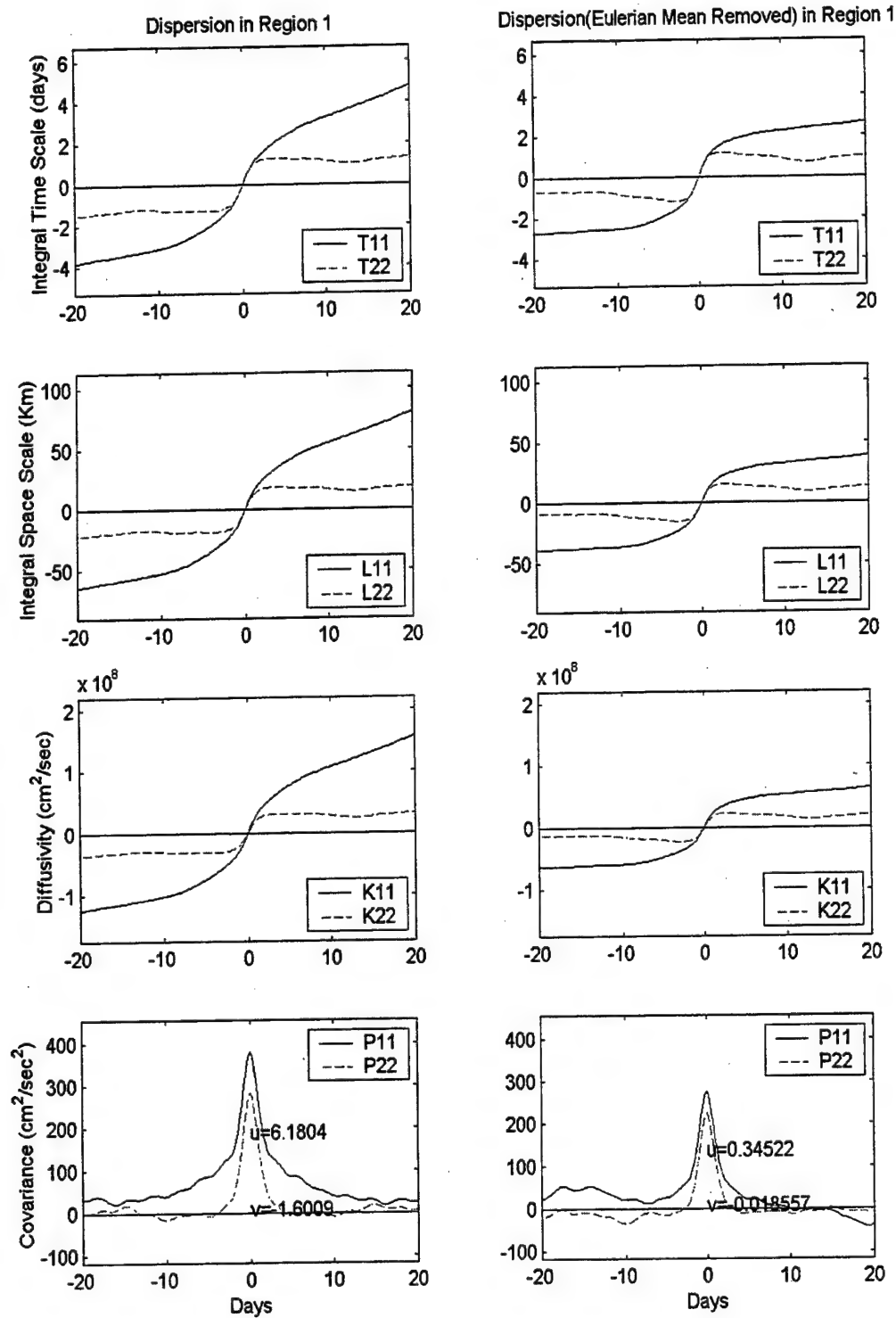


Figure 55. Region 1 Lagrangian statistics without (left) and with (right) the Eulerian mean flow removed for time lags between +20 and -20 days.

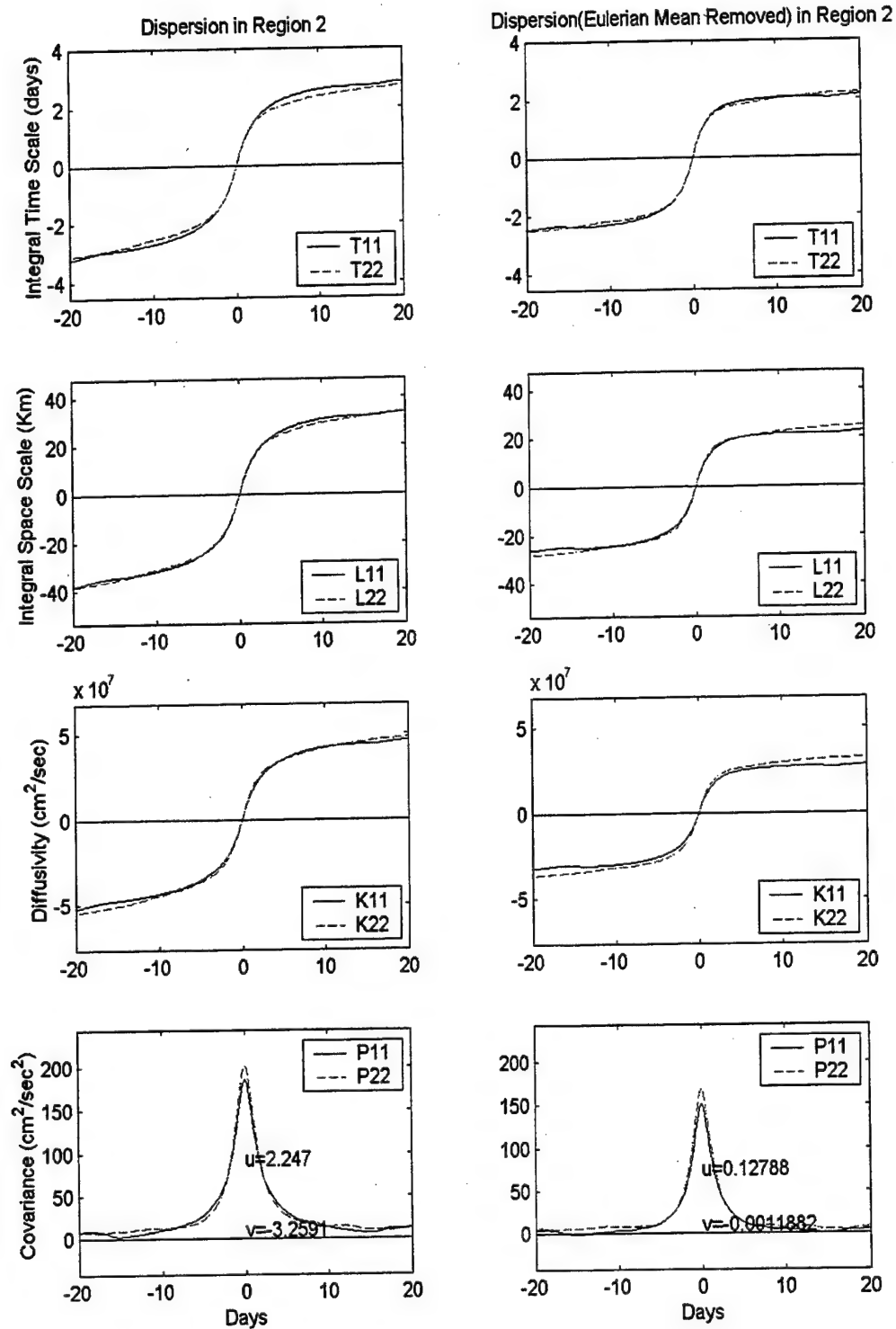


Figure 56. Region 2 Lagrangian statistics without (left) and with (right) the Eulerian mean flow removed for time lags between +20 and -20 days.

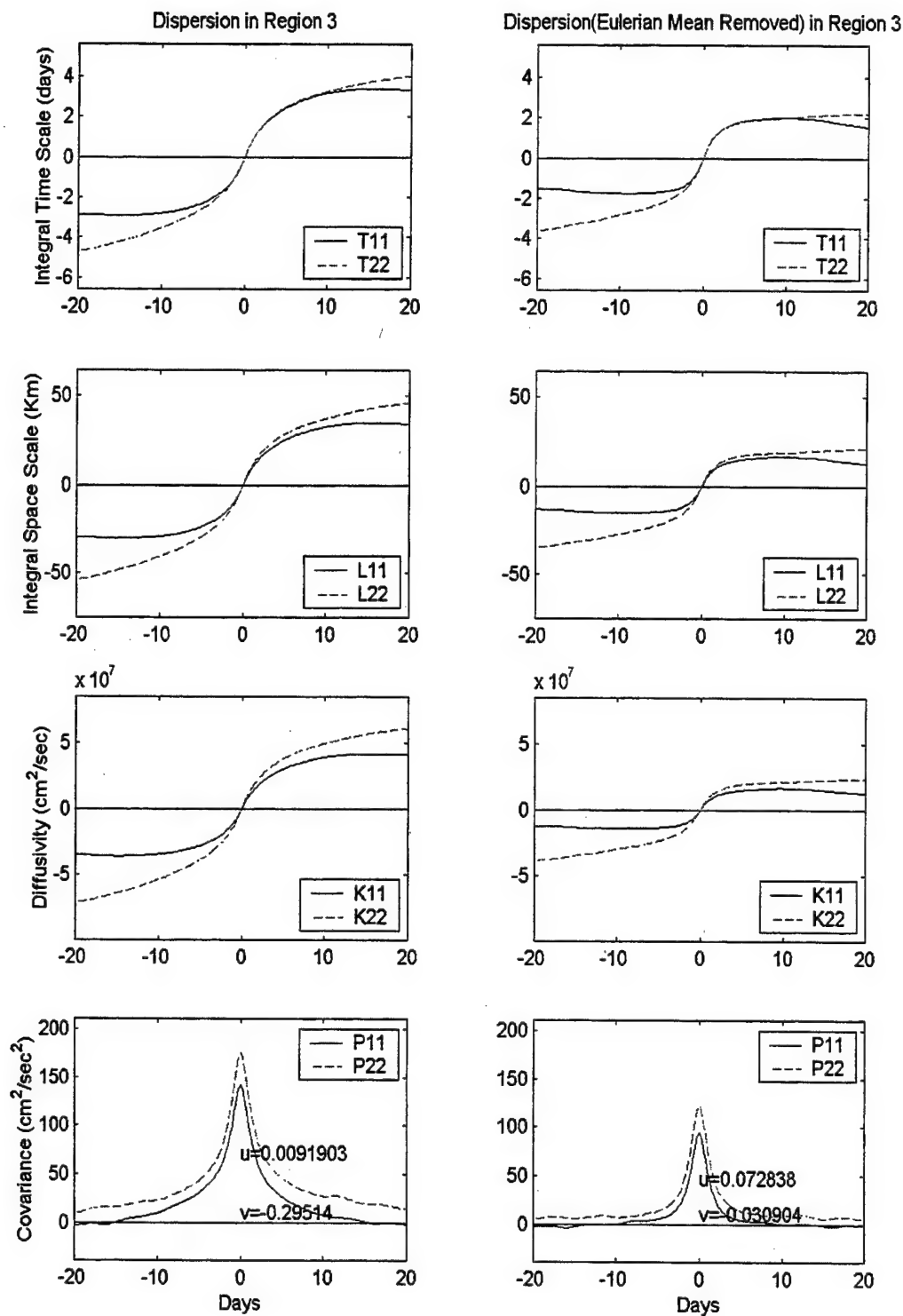


Figure 57. Region 3 Lagrangian statistics without (left) and with (right) the Eulerian mean flow removed for time lags between +20 and -20 days.

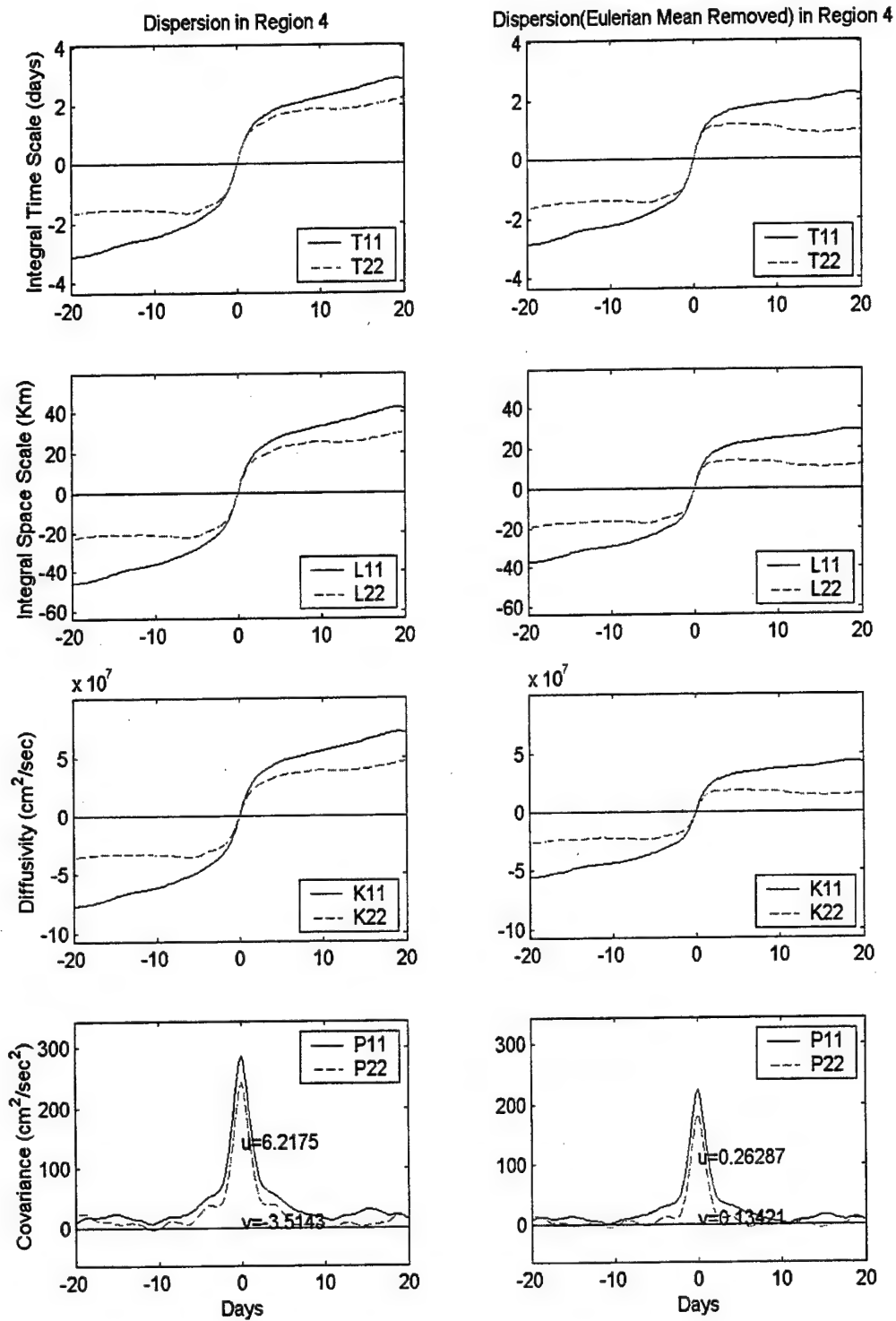


Figure 58. Region 4 Lagrangian statistics without (left) and with (right) the Eulerian mean flow removed for time lags between +20 and -20 days.

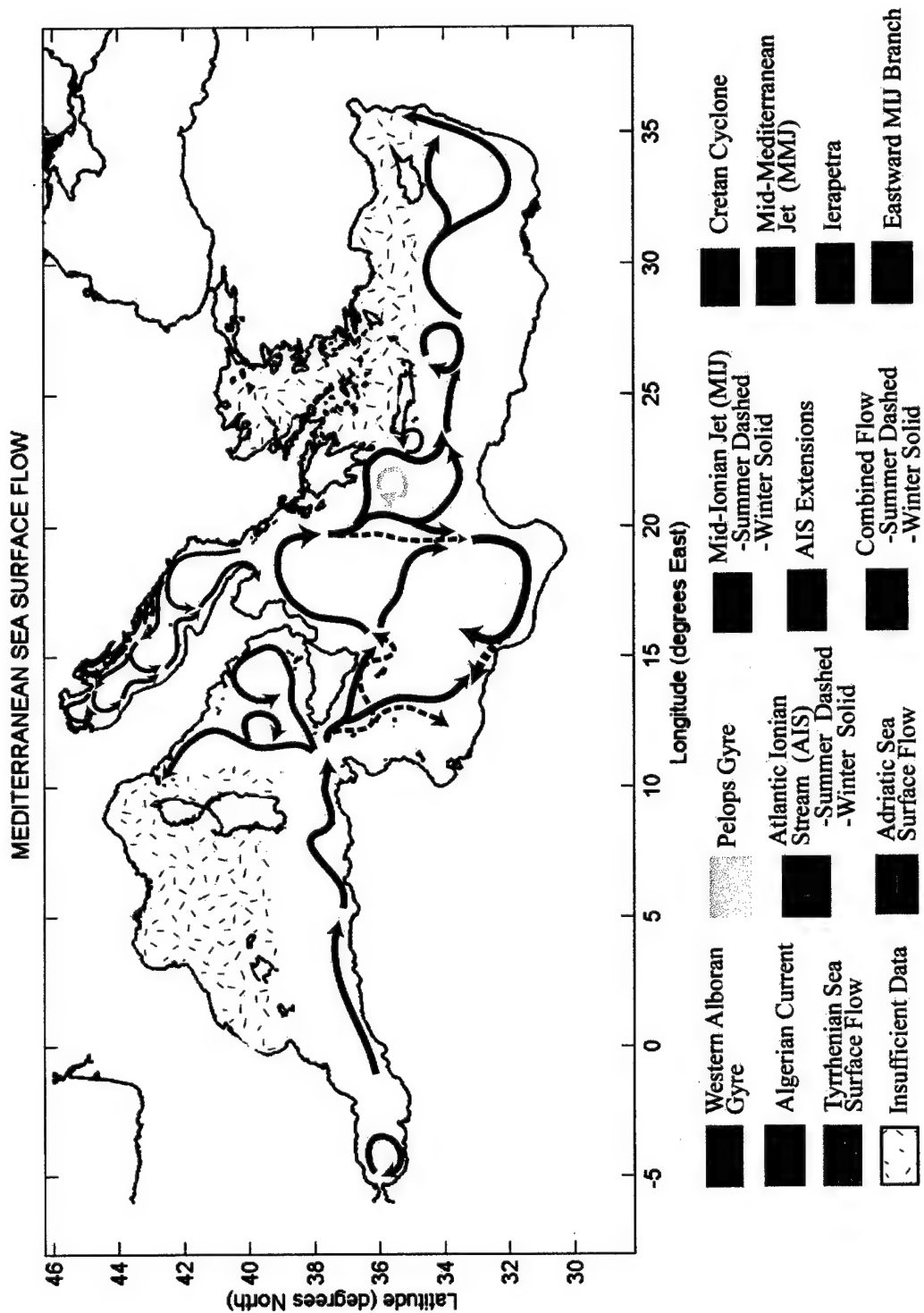


Figure 59. Mediterranean Sea surface circulation derived from drifter data (1986-1999). Arrows indicate the locations and directions of the major currents observed, but do not indicate the relative strength of the currents.

LIST OF REFERENCES

- Artegiani, A., D. Bregant, E. Paschini, N. Pinardi, F. Raicich and A. Russo, "The Adriatic Sea general circulation, Part II: Baroclinic Circulation Structure," *J. Phys. Oceanogr.*, vol. 27, pp. 1515-1532, 1997.
- Borzelli, G., R. Ligi and E. Ferulano, "Surface circulation in the northern Adriatic Sea as revealed by a drifter experiment," *Il Nuovo Cimento*, vol. 15, pp. 265-274, 1992.
- Davis, R. E., "Drifter observations of coastal currents during CODE. The method and descriptive view," *J. Geophysics. Res.*, vol. 90, pp. 4741-4655, 1985.
- Davis, R. E., "Observing the general circulation with floats," *Deep-Sea Res.*, vol. 38, Suppl. 1, pp. S531-S571, 1991.
- Emery, W. J. and R. Thomson, *Data analysis methods in physical oceanography*, Pergamon, Elsevier Science Ltd., Oxford, UK, p. 624, 1998.
- Feruglio, G., "Risultati di esperienze con galleggiati per lo studio delle correnti del Mare Adriatico negli anni 1910-1914," *Memoria*, LV, Italy, pp. 3-92, 1920.
- Font, J., C. Millot, J. Salas, A. Julia, and O. Chic, "The drift of Modified Atlantic Water from the Alboran Sea to the eastern Mediterranean," *Scientia Marina*, vol. 62(3), pp. 211-216, 1998.
- Gacic, M., V. Kovacevic, B. Manca, E. Papageorgiou, P.-M. Poulain, P. Sacarazzato and A. Vetrano, "Thermohaline properties and circulation in the Otranto Strait," *Bulletin De l'Institute oceanographique*, Monaco, CIESM Sciences Series 2, Special vol. 17, pp. 117-145, 1996.
- Gacic, M., G. Civitarese and L. Ursella, "Spatial and seasonal variability of water and biogeochemica; fluxes in the Adriatic Sea," *The Eastern Mediterranean as a Laboratory for Basin for the Assessment of Contracting Ecosystems*, Kluwer Acad. Publ., pp. 335-357, 1999.
- Grilli, F. and N. Pinardi, "The computation of Rossby radii of deformation for the Mediterranean Sea", *MTP News*, vol. 6, pp. 4-5, 1998.
- Hansen, D. V. and P. Poulain, "Processing of WOCE/TOGA drifter data," *J. Atmos. Oceanic Technol.*, vol. 13, pp. 900-909, 1996.

Larnicol, G., P. Traon, N. Ayoub, and P. De Mey, "Mean sea level and surface circulation variability of the Mediterranean Sea from 2 years of TOPEX/POSEIDON altimetry," *J. Geophys. Res.*, vol. 100, no. C12, pp. 25163-25177, 1995.

Malanotte-Rizzoli, P., B. Manca, M. D'Alcala, A. Theocharis, A. Bergamasco, D. Bregant, G. Budillon, G. Civitarese, D. Georgopoulos, A. Michelato, E. Sansone, P. Scarazzato, and E. Souvermezoglou, "A synthesis of the Ionian Sea hydrography, circulation and water mass pathways during POEM-Phase I," *Prog. Oceanog.*, vol. 39, pp. 153-204, 1997.

Matteoda, A. and S. Glenn, "Observations of recurrent mesoscale eddies in the eastern Mediterranean," *J. Geophys. Res.*, vol. 101, no. C9, pp. 29687-20709, 1996.

Mauri, E. and P. Poulain, "Northern Adriatic Sea surface circulation and temperature/pigment fields in September and October 1997," *J. Mar. Sys.*, submitted, 2000.

Mazelle, E., "Flachenposten in der Adria zur Bestimmung der Oberflachen," *Stromengen. Denkschr. Akad. Wiss. Naturwiss. Klasse*, 91, pp 1-46, 1914.

Millot, C., "Mesoscale and seasonal variabilities of the circulation in the western Mediterranean," *Dynamics of Atmospheres and Oceans*, vol. 15, pp. 179-214, 1991.

Millot, C., "Circulation in the Western Mediterranean Sea," *J. Mar. Sys.*, vol. 20, pp. 423-442, 1999.

Niiler, P., A. Sybrandy, K. Bi, P. -M. Poulain, and D. Bitterman, "Measurements of the water-following capability of holey-sock and TRISTAR drifters," *Deep-Sea Res. I*, vol. 42, no. 11/12, pp. 1951-1964, 1995.

Ovchinnikov, I. M., "Circulation in the surface and intermediate layers of the Mediterranean," *Oceanology*, vol. 6, pp. 48-59, 1966.

Pinardi, N. and A. Navarra, "Baroclinic Wind Adjustment Process in the Mediterranean Sea," *Deep Sea Res. II*, vol. 40, no. 6, pp. 1299-1326, 1993.

Pinardi, N., G. Korres, A. Lascaratos, V. Roussenov and E. Stanev, "Numerical simulation of the Mediterranean Sea upper ocean circulation," *Geophys. Res. Letters*, vol. 24, 4, pp. 425-428, 1997.

Poulain, P. -M. and P. Zanasca, "Drifter observations in the Adriatic Sea (1994-1996) – Data report," SACLANTCEN Memorandum, SM-340, SACLANT Undersea Research Centre, La Spezia, Italy, p. 46, 1998.

Poulain, P. -M., "Drifter observations of surface circulation in the Adriatic Sea between December 1994 and March 1996," J. Mar. Sys., vol. 20, pp. 231-253, 1999.

Poulain, P. -M., "Adriatic Sea Surface Circulation as Derived From Drifter Data Between 1990 and 1999", J. Mar. Sys., submitted, 2000.

Poulain, P. -M., E. Mauri, C. Fayos, L. Ursella and P. Zanasca, "Mediterranean Surface Drifter Database," website, [<http://www.oc.nps.navy.mil/~drifter/database>], 2000a.

Poulain, P. -M., E. Mauri, C. Fayos, L. Ursella and P. Zanasca, "Mediterranean surface drifter measurements between 1986 and 1999", CD-ROM, Naval Postgraduate School, Monterey, CA, 2000b.

Robinson, A. and M. Golnaraghi, "Circulation and dynamics of the Eastern Mediterranean Sea: quasi-synoptic data-driven simulations," Deep-Sea Res. II, vol. 40, no. 6, pp. 1207-1246, 1993.

Robinson, J., J. Sellschopp, A. Warn-Varnas, W. Leslie, C. Lozano, P. Haley Jr., L. Anderson, and P. Lermusiaux, "The Atlantic Ionian Stream," J. Mar. Sys., vol. 20, pp. 129-156, 1999.

Salas, J., E. Garcia-Ladona, and J. Font, "Statistical analysis of the surface circulation in the Algerian Current using Lagrangian buoys," J. Mar. Sys., submitted, 2000.

Sybrandy, A. and P. Niiler, *WOCA/TOGA Lagrangian Drifter Construction Manual*, WOCE Report, No. 63, p. 58, February, 1991.

INITIAL DISTRIBUTION LIST

1. Defense Technical Information Center.....2
8725 John J. Kingman Rd, STE 0944
Ft. Belvoir, Virginia 22060-6218

2. Dudley Knox Library.....2
Naval Postgraduate School
411 Dyer Rd
Monterey, California 93943-5101

3. Chairman, Code OC.....1
Department of Oceanography
Naval Postgraduate School
833 Dyer Rd. Room 328
Monterey, California 93943-5122

4. Professor Pierre-Marie Poulain (Code OC/PN).....4
Department of Oceanography
Naval Postgraduate School
833 Dryer Rd. Room 328
Monterey, California 93943-5122

5. Professor Robert L. Haney (Code MR/HY).....1
Department of Meteorology
Naval Postgraduate School
833 Dryer Rd. Room 328
Monterey, California 93943-5122

6. Professor Jeffrey D. Paduan (Code OC/PD).....1
Department of Oceanography
Naval Postgraduate School
833 Dryer Rd. Room 328
Monterey, California 93943-5122

7. Director.....1
SACLANT Undersea Research Centre
SACLANTCEN CMR 426
APO-AE 09613-5000

8. Dr. Elisabeth Horton..... 1
Integrated Drifting Buoy Program Manager
Naval Oceanographic Office
1002 Balch Blvd.
Stennis Space Center, Mississippi 39522-5001
9. LT Todd Mauerhan..... 4
2443 Rim Oak
San Antonio, Texas 78232